

A NUMERICAL STUDY OF VORTICES AND TURBULENCE IN
QUANTUM FLUIDS

GEORGE WILLIAM STAGG

Thesis submitted for the degree of
Doctor of Philosophy



*School of Mathematics & Statistics
Newcastle University
Newcastle upon Tyne
United Kingdom*

June 2016

Acknowledgements

I would like to thank everybody...

The work featured in this thesis was carried out in the period of 2012–2016. Some of the results over that time can also be found in the following publications:

- Critical velocity of a finite-temperature Bose gas
G. W. Stagg, R. W. Pattinson, C. F. Barenghi, N. G. Parker, Phys. Rev. A **93**, 023640 (2016)
- Classical-like wakes past elliptical obstacles in atomic Bose-Einstein condensates
G. W. Stagg, A. J. Allen, C. F. Barenghi, N. G. Parker, J. Phys.: Conf. Ser. **594** 012044 (2015)
- Generation and decay of two-dimensional quantum turbulence in a trapped Bose-Einstein condensate
G. W. Stagg, A. J. Allen, N. G. Parker and C. F. Barenghi, Phys. Rev. A **91**, 013612 (2015)
- Quantum analogues of classical wakes in Bose-Einstein condensates
G. W. Stagg, N. G. Parker and C. F. Barenghi, J Phys B: At. Mol. Opt. Phys. **47** 095304 (2014)

Abstract

Quantum fluids possess amazing properties of which two are particularly striking. Firstly they exhibit superfluid flow, with the total absence of viscosity. Secondly, there are no excitations when the fluid velocity (relative to some obstacle) is slower than a critical value; above this velocity the flow becomes dissipative and macroscopic excitations are created in the form of quantised vortices with fixed circulation proportional to Planck's constant. In this thesis we numerically study the dynamics of these phenomena, from the production of a single vortex pair to the complex and chaotic motion of turbulent vortex tangles, modelling both superfluid helium and atomic Bose-Einstein condensates (BEC) with obstacles of various shape and size. We give detailed descriptions of the numerical schemes and present extensive numerical simulation of the Gross-Pitaevskii equation (GPE) and its variants at zero temperature and beyond, in both two and three dimensions.

We study the wake that forms behind obstacles in the presence of a superfluid flow, modelling atomic BEC experiments with moving laser-induced potentials. We find that suitable obstacles produce classical-like wakes consisting of clusters of vortices of the same polarity. Remarkably, symmetric wakes resemble those observed in classical flow at low Reynolds number, despite the constrained vorticity. The structures are unstable, forming time-dependent asymmetric wakes similar to a Bénard–von Kármán vortex street.

Motivated by the recent work of Kwon *et al.* (Phys. Rev. A **90**, 063627 (2014)), we model an atomic BEC experiment in which a trapped, oblate condensate is translated past a stationary, laser-induced obstacle. The critical velocity is exceeded and so vortices nucleate, forming a state of two-dimensional quantum turbulence. We explore the system at both zero-temperature and with thermal dissipation, modelled through a phenomenological term in the GPE. Our simulations provide insight into early-stage evolution, not accessible experimentally, and into the decay of vortices by annihilation or passage out of the condensate.

We use classical field methods to simulate homogeneous Bose gases at finite temperature, from strongly non-equilibrium initial distributions to thermalised equilibrium states. We introduce a moving cylindrical potential and study how the thermal component of the gas affects vortex nucleation. We have found that the critical velocity decreases with increasing temperature and scales with the speed of sound. Above the critical velocity, vortices are nucleated as irregular vortex lines, rings, or vortex tangles.

Finally we model the surfaces of walls and moving objects (such as wires, grids, propellers or spheres) in the presence of superfluid liquid helium flow, using a real rough boundary obtained via atomic force microscopy. We find evidence pointing to the formation of a thin ‘superfluid boundary layer’ consisting of vortex loops and rings. As boundary layers usually arise from viscous forces, this is a surprising and intriguing result.

Contents

I Introduction and Theory	1
1 Introduction to Bose-Einstein Condensates	2
1.1 Superfluid Helium	2
1.2 Ultra-cold Bose Gases	2
1.3 Bose-Einstein Condensation	2
1.4 Macroscopic excitations: Vortices and Solitons	2
1.5 Quantum Turbulence	2
2 Theoretical Modelling of BEC	3
2.1 Mean-field description	3
2.2 The Gross-Pitaevskii Equation	3
2.3 Dimensionless Gross-Pitaevskii Equations	4
2.3.1 Homogeneous GPE	4
2.3.2 Trapped GPE	5
2.4 Quasi-Two-Dimensional Gross-Pitaevskii Equation	6
2.5 Time-independent Gross-Pitaevskii Equation	6
2.6 The imaginary time propagation method	7
2.7 The chemical potential	8
2.8 The Dissipative Gross-Pitaevskii Equation	9
2.9 Finite temperature homogeneous condensate using the classical field method	11
2.10 Transforming the reference frame	12
2.10.1 Linearly translating frame	12
2.10.2 Rotating frame	12
2.11 Hydrodynamic interpretation	13
2.12 Quantised Circulation	13
2.13 A selection of simple solutions	14
2.13.1 Density near a wall	14
2.13.2 Soliton solutions	15
2.13.3 Quantised Vortices	16

2.14	Initial Conditions	18
2.14.1	Homogeneous initial condition	18
2.14.2	Thomas-Fermi profile of a trapped condensate	18
2.14.3	Classical field initial condition	19
2.15	Creating obstacles with repulsive potentials	20
2.15.1	Three-dimensional elliptical Gaussian	20
2.15.2	Two and Three-dimensional cylindrical Gaussian	20
2.15.3	Three-dimensional ‘realistic’ rough-surface	21
3	Numerical Theory and Procedures	22
3.1	Numerical procedures for 2D and 3D solutions	22
3.1.1	Fourth order Runge-Kutta scheme	22
3.1.2	Numerical stability and convergence	23
3.2	Identifying vortices	24
3.2.1	Basic vortex detection method	25
3.2.2	Visualising vortex location with a vortex field	25
3.2.3	Further improving accuracy with a Gaussian blur	27
3.2.4	Avoiding ‘ghost vortices’	28
3.3	Quantifying vortex clustering in 2D	30
3.3.1	Vortex counting	30
3.3.2	Ripley’s K and L functions	30
3.3.3	Recursive Cluster Algorithm	32
3.4	Building vortex trajectories	33
3.5	Removing vortices with phase unwinding	34
3.6	Quasi-Condensate Visualisation	36
3.7	Evaluation of vortex line-length in 3D	37
II	Numerical Studies	38
4	Classical-like wakes behind elliptical obstacles in Bose-Einstein condensates	39
4.1	Introduction	39
4.2	Model	41
4.3	Two-Dimensional Wakes	41
4.3.1	Vortex emission from elliptical obstacles	41
4.3.2	Formation of the Bénard–von Kármán vortex street	43
4.3.3	Critical Velocity past an Elliptical Obstacle	44
4.3.4	Role of Obstacle Size and Ellipticity on the Wake	46
4.3.5	Vortex Clustering	46

4.4	Results: Three-Dimensional Wakes	47
4.4.1	Symmetric Wakes	47
4.4.2	Asymmetric Wakes	48
4.5	Conclusion	49
4.6	Model of 2D and 3D BEC with Gaussian Potentials	50
5	Decay of 2D quantum turbulence in a highly oblate Bose-Einstein condensate	51
5.1	Introduction	51
5.2	Set-Up	52
5.3	Results	53
5.3.1	Number of Vortices Generated	53
5.3.2	Stages of the Condensate Evolution	54
5.3.3	Crescent-Shaped Density Structures	58
5.3.4	Vortex Generation via an Elliptical Obstacle	59
5.4	Conclusion	59
6	Critical velocity at finite temperature	61
6.1	Introduction	61
6.2	Classical Field Method	63
6.3	Equilibration dynamics and decay of the vortex tangle	65
6.4	Moving obstacle at finite-temperature	67
6.4.1	Critical velocity for vortex nucleation	67
6.4.2	Vortex nucleation pattern	69
6.5	Conclusions	71
7	Simulating the surface of a “Floppy Wire”	73
7.1	Introduction	73
7.2	Method	74
7.3	Three-dimensional results	77
7.4	Two-dimensional results	78
7.4.1	Truncated surfaces	80
7.5	Conclusions	80
III	Appendix	82
A	Detailed Derivations	83
A.1	Derivation of the Runge-Kutta scheme	83
A.2	Derivation of the Gross-Pitaevskii Equation	86
A.3	Derivation of the Hydrodynamic Equations via the Madelung Transformation	90

B Important Quantities	93
B.1 Energy	93
B.2 Force	94
B.3 Healing Length	94
C Algorithms	96
C.1 Density/Phase Visualisation Technique	96
C.1.1 Plotting Algorithm	96
C.1.2 Colour space conversion - rgb to hsl	97
C.1.3 Colour space conversion - hsl to rgb	97
C.2 Other Numerical Algorithms	98
Bibliography	105

Part I

Introduction and Theory

Chapter 1

Introduction to Bose-Einstein Condensates

1.1 Superfluid Helium

1.2 Ultra-cold Bose Gases

1.3 Bose-Einstein Condensation

1.4 Macroscopic excitations: Vortices and Solitons

1.5 Quantum Turbulence

Chapter 2

Theoretical Modelling of BEC

2.1 Mean-field description

We aim to accurately model the dynamics of a closed system containing a dilute, weakly interacting Bose gas of N atoms, at extremely low temperatures. One could model the entire system by constructing a N -body quantum wavefunction, which would follow the Schrödinger equation, but the complexity of this method makes it extremely unwieldy to model the large number of particles used in Bose-Einstein condensate (BEC) experiments.

We instead model the system with a mean-field theory, described in Section 2.2, in which there are essentially two main approximations. First, justified by the dilute property of the gas, any binary interaction between particles is assumed to be a contact delta function of the form,

$$V(\mathbf{r} - \mathbf{r}') = g\delta(\mathbf{r} - \mathbf{r}').$$

Interactions involving a higher number of particles are ignored. Secondly, we assume all particles in the condensate are macroscopically described by a single wavefunction, $\psi(\mathbf{r}, t)$. As the particles all share the same phase and quantum state, $\psi(\mathbf{r}, t)$ is a classical field. This second approximation also assumes that there are no particles contributing to thermal or quantum fluctuations beyond the classical field, and so is only justified in general when the temperature, T , is exactly 0K. Nevertheless, we go further and describe some finite-temperature based effects in Sections 2.8 and 2.9.

2.2 The Gross-Pitaevskii Equation

The result of the mean-field methodology is the Gross-Pitaevskii equation (GPE),

$$i\hbar \frac{\partial \Psi(\mathbf{r}, t)}{\partial t} = \left(-\frac{\hbar^2}{2m} \nabla^2 + V(\mathbf{r}, t) + g|\Psi(\mathbf{r}, t)|^2 - \mu \right) \Psi(\mathbf{r}, t), \quad (2.1)$$

where $V(\mathbf{r}, t) = V_{\text{obj}}(\mathbf{r}, t) + V_{\text{trap}}(\mathbf{r}, t)$. In the homogeneous case $V_{\text{trap}}(\mathbf{r}, t) = 0$, otherwise a harmonic trapping potential is used. In the case of a 3D spherically symmetric condensate the harmonic trapping potential is defined as $V_{\text{trap}}(\mathbf{r}, t) = m\omega r/2$.

The first two terms on the right hand side of the GPE are the energy of a single particle in a potential field, and the third term describes the non-linear effects between the multiple particles in the system, with a strength usually parametrised by $g = 4\pi N \hbar^2 a / m$, where m is the mass of a single particle, a is the s-wave scattering length and N is the number of particles. Taking into account the fact that the GPE is only strictly valid at $T = 0$, it turns out the equation is surprisingly successful at quantitatively modelling ultra-cold gasses, even up to a temperature of $T = \frac{T_c}{2}$, where T_c is the critical temperature for Bose-Einstein condensation. The GPE is also successful at qualitatively modelling BEC based effects in higher temperature superfluids, such as liquid helium II[CITE] and even in neutron stars [CITE].

A detailed explanation of the mean-field formulation of the model and the full derivation of the GPE is shown in Section A.2.

2.3 Dimensionless Gross-Pitaevskii Equations

Bose-Einstein condensates can be formed with almost any size or scale. A trapped atomic cold gas BEC in particular can be experimentally realised with a wide range of topologies and atom interaction strength. A wide range of parameters can be fairly easily manipulated with magnetic or optical potentials and Feshbach resonances [CITE]. Superfluid helium can also form in various sizes, with vortex core radii of ~ 1 or ~ 100 angstroms, depending on the isotope of helium used. The cores of neutron stars are even theorised to be superfluid on a large scale. For this reason it is desirable to rescale the quantities used in the GPE so that any of the calculations performed can be easily reformulated into any length scale desired. We make this process easier by doing all calculations with dimensionless parameters. Another advantage of the dimensionless formulation is that the size of the values involved are all normalised on the scale of unity, reducing the chance of errors in numerical computation due to the floating point representation used by modern computer architectures. We present two methods of making the GPE dimensionless, the specific scaling used is chosen by the needs of the simulation and is usually apparent (such as by whether a trapping potential is involved).

2.3.1 Homogeneous GPE

Consider a homogeneous system with repulsive iterations and where $V_{\text{trap}} = 0$. In this case, Ψ does not depend on \mathbf{r} or t , and so we can set the time and spatial derivatives in

the GPE to zero,

$$0 = (g|\Psi(\mathbf{r}, t)|^2 - \mu)\Psi(\mathbf{r}, t). \quad (2.2)$$

By rearranging, we can easily find the natural homogeneous density of the system: $\rho = |\Psi|^2 = \mu/g$. We then choose to rescale the wavefunction using this value, so that $\psi = \Psi/\sqrt{\rho}$.

By dimensional arguments (see Appendix B.3 for details), the length scale of space is the healing length, $\xi = \hbar/\sqrt{mg\rho}$, and the length scale of time $\tau = \hbar/(g\rho)$. These units are often called the ‘natural units’. We define the rescaled dimensionless quantities as

$$\tilde{t} = \frac{t}{\tau}, \quad \tilde{r} = \frac{r}{\xi}, \quad \tilde{\varepsilon} = \frac{\varepsilon}{\mu}, \quad (2.3)$$

for time, length, and energy respectively, where a tilde denotes a dimensionless quantity. Substituting the dimensionless quantities into Equation 7.1 leads to the homogeneous GPE,

$$i\frac{\partial\psi(\tilde{\mathbf{r}}, \tilde{t})}{\partial\tilde{t}} = \left(-\frac{1}{2}\hat{\nabla}^2 + |\psi(\tilde{\mathbf{r}}, \tilde{t})|^2 + \tilde{V}_{\text{obj}}(\tilde{\mathbf{r}}, \tilde{t}) - 1\right)\psi(\tilde{\mathbf{r}}, \tilde{t}). \quad (2.4)$$

2.3.2 Trapped GPE

When considering a harmonically trapped condensate it is convenient to work with a wavefunction with density normalised to unity,

$$\int |\phi|^2 d^3\mathbf{r} = 1. \quad (2.5)$$

We make Equation 7.1 dimensionless using the harmonic oscillator length, $l = \sqrt{\hbar/(m\omega)}$, where ω is a trap frequency. This leads to the dimensionless rescalings,

$$\hat{t} = t\omega, \quad \hat{r} = \frac{r}{l}, \quad \hat{\varepsilon} = \frac{\varepsilon}{\hbar\omega}, \quad (2.6)$$

for time, length, and energy respectively, where a hat denotes a dimensionless quantity. We find then that

$$\int |\Psi|^2 d^3\mathbf{r} = N \Rightarrow \int |\Psi|^2 N^{-1} l^3 d^3\hat{\mathbf{r}} = 1, \quad (2.7)$$

and so we rescale the wavefunction to satisfy Equation 2.5,

$$|\phi|^2 = |\Psi|^2 N^{-1} l^3 \Rightarrow \phi = \Psi N^{-\frac{1}{2}} l^{\frac{3}{2}}. \quad (2.8)$$

Substituting the new rescaled quantities into Equation 7.1 leads us to the trapped GPE,

$$i\frac{\partial\phi(\hat{\mathbf{r}}, \hat{t})}{\partial\hat{t}} = \left(-\frac{1}{2}\hat{\nabla}^2 + \hat{g}|\phi(\hat{\mathbf{r}}, \hat{t})|^2 + \hat{V}(\hat{\mathbf{r}}, \hat{t}) - \hat{\mu}\right)\phi(\hat{\mathbf{r}}, \hat{t}). \quad (2.9)$$

where

$$\hat{g} = \frac{gN}{\hbar\omega l^3}. \quad (2.10)$$

2.4 Quasi-Two-Dimensional Gross-Pitaevskii Equation

For some condensate geometries it is useful to be able simulate the condensate via a lower dimensional GPE. An example of this is a highly oblate condensate, in which the trapping potential is defined as

$$V_{\text{trap}}(x, y, z) = m\omega_{\perp}^2 \frac{x^2 + y^2}{2} + m\omega_z^2 \frac{z^2}{2}, \quad (2.11)$$

with trapping frequencies $\omega_z \gg \omega_{\perp}$ and under the condition $\hbar\omega_z \gg \mu$, where μ is the 3D chemical potential. Tight z confinement causes the dynamics to become essentially two dimensional (experimentally achieved in [1]) as the wavefunction along z becomes fixed into the independent harmonic oscillator ground state, so that

$$\Psi(\mathbf{r}, t) = \Psi_{\perp}(x, y, t)\Psi_z(z). \quad (2.12)$$

An expression for Ψ_z is found by assuming a Gaussian ground state under the condition that $\int |\Psi_z(z)|^2 dz = 1$.

$$\Psi_z(z) = \pi^{-1/4} l_z^{-1/2} \exp(-z^2/2l_z^2), \quad (2.13)$$

where $l_z = \sqrt{\hbar/m\omega_z}$. This is known as the quasi-2D regime and when this form of Ψ is substituted into Equation 7.1 it forms a 2D-GPE that can be used to model the system with reduced dimensionality, with the modified interaction term $g_{2D} = g/(\sqrt{2\pi}l_z)$ [2]. The 3D chemical potential μ is also modified as an extra term is absorbed, $\mu_{2D} = \mu - \hbar\omega_z/2$, and all other three-dimensional properties become two-dimensional.

A similar process can be performed with ‘cigar’ quasi-1D geometries so that a 1D-GPE can be used with a modified g_{1D} interaction term, and μ_{1D} chemical potential. As before all 3D properties become 1D, however as we will not consider quasi-1D regimes in detail, the specifics are omitted from this thesis.

2.5 Time-independent Gross-Pitaevskii Equation

We find a stationary version of the GPE by first fixing the potential, $V(\mathbf{r})$, so that it is constant in time, and then writing the wavefunction in the form $\Psi(\mathbf{r}, t) = \Psi_0(\mathbf{r}) \exp(i\mu t/\hbar)$, where $\Psi_0(\mathbf{r})$ is the ground state. Equation 7.1 then becomes

$$\mu\Psi_0(\mathbf{r}) = \left(-\frac{\hbar^2}{2m}\nabla^2 + V(\mathbf{r}) + g|\Psi_0(\mathbf{r})|^2 \right) \Psi_0(\mathbf{r}), \quad (2.14)$$

the time-independent GPE. In the absence of interactions, $g = 0$, this reduces to the standard Schrödinger equation. This version of the GPE can be used to find stationary solutions of the system for a certain value of μ , characterising the energy of the ground state.

2.6 The imaginary time propagation method

Many numerical explorations of quantum systems, particularly those associated with magnetic or optical trapping, involve calculating the ground-state as either the final result or as a stepping stone for further calculations. While often there exists analytic solutions for a condensate ground state, this problem is often solved numerically using so called eigensolvers. Numerically finding the ground state becomes practically necessary if a simulation requires complicated potential fields.

There are several methods available for implementing a numerical eigensolver: inverse iteration and Lanczos methods [3], systematic variational techniques [4], boundary eigenvalue methods [5], conjugate gradient techniques [6] and imaginary time propagation [7]. We choose to use the last of these methods due to its relative simplicity at the expense of computational time.

The imaginary time method revolves around moving from real to imaginary time using a Wick rotation $\tau = it$. The substitution transforms the GPE into a form similar to a diffusion equation. As a result, a local equilibrium can be found by propagating τ . This can be understood by considering a trial solution (as similar to the true ground-state as possible) as a collection of eigenfunctions Ψ_n corresponding to eigenvalues E_n ,

$$\Psi(\mathbf{r}, \tau) = \sum_n \Psi_n(\mathbf{r}) \exp\left(-\frac{E_n \tau}{\hbar}\right).$$

The eigenfunctions decay exponentially under propagation of the GPE in imaginary time. In particular, the decay rate is directly related to the size of the eigenvalues E_n , so that eigenfunctions relating to higher eigenvalues decay the fastest. The final ingredient is to inhibit the overall decay of the wavefunction by renormalising during propagation. After a sufficient transient time the contributions from the higher eigenvalues become negligible, forcing the wavefunction to tend towards the lowest energy eigenfunction,

$$\Psi(\mathbf{r}, \tau) \rightarrow \Psi_0(\mathbf{r}) \exp\left(-\frac{E_0 \tau}{\hbar}\right).$$

The imaginary time propagation method converges on the ground state solution very slowly and so we must perform many numerical steps to prepare an initial state. A silver lining of this drawback is that the method can be used to prepare almost any viable initial

state. For example, an initial condition consisting of a Thomas-Fermi profile with many vortices can be made more accurate with this method by imposing the phase during imaginary time propagation. The result is a less violent start to condensate dynamics; minimal sound is produced due to the difference between the approximate initial condition and a true solution of the GPE.

The energy can be used as a way to gauge the solution convergence. An example ground state solution is found using the imaginary time method and is shown with the energy in Figure 2.1. For $-t\omega/i > 0.6$ the computed ground state energy does not significantly change, a good indicator that the ground state has been found to sufficient accuracy.

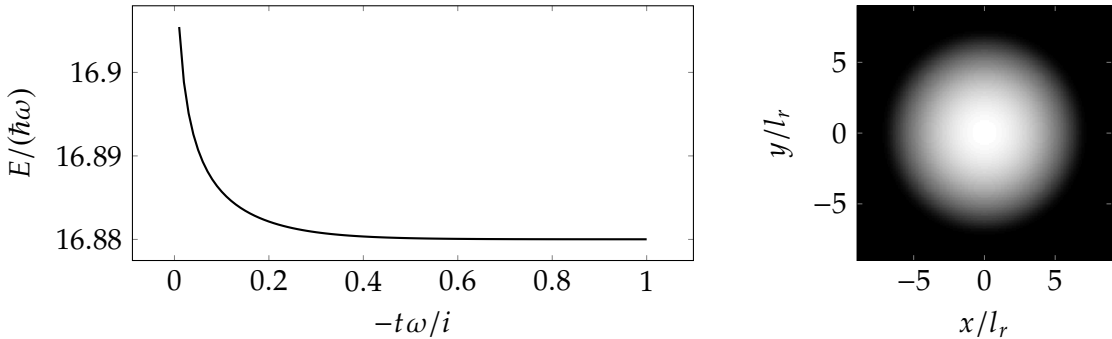


Figure 2.1: An example of the use of the imaginary time propagation method for finding the condensate ground state for a condensate with interaction energy $\hat{g} = 2000$ and $\hat{\mu} = 25.27$, with the Thomas-Fermi solution as the initial state. The density of the final ground state solution is shown (right) along with the energy of the solution as the method propagates through imaginary time (left).

2.7 The chemical potential

The chemical potential of the system, μ , can be thought of as the energy required to remove a particle from a system with large N , or alternatively as a measure of the energy of a particle. The value of μ will vary for the specific species of bosons considered and provides a useful scale of energy.

The chemical potential can be found in terms of energies of the system by direct integration of Equation 2.14,

$$\mu = (E_{\text{kin}} + E_{\text{pot}} + 2E_{\text{int}})/N, \quad (2.15)$$

Where the quantities E_{kin} , E_{pot} and E_{int} are defined in Appendix B.1.

2.8 The Dissipative Gross-Pitaevskii Equation

Equation 7.1 does not include any form of damping or dissipation. In fact, up to numerical accuracy, the GPE conserves both the particle number and the total energy of the system. This is in direct opposition of physical reality, where due to the effects of finite-temperature all excitations in experiments are damped over time. The Dissipative Gross-Pitaevskii Equation (DGPE) attempts to introduce a simple-minded way of modelling finite-temperature damping by introducing a phenomenological dissipation into the GPE. The procedure was introduced by Pitaevskii [8] and refined by others [9, 10, 11]. The derivation of the DGPE presented here closely follows the arguments shown previously by these authors.

We would like to extend the GPE such that a damping process is introduced, so that dynamics approach an equilibrium state over time. Such an equilibrium state can be described by Equation 2.14. The equation of motion for our wavefunction Ψ is then written

$$i\hbar \frac{\partial \Psi}{\partial t} = \hat{L}\Psi, \quad (2.16)$$

where \hat{L} is a non-Hermitian operator (so that we have a relaxation process). At equilibrium the anti-Hermitian part of $\hat{L}\Psi$ must be zero, we force this by writing the anti-Hermitian part of $\hat{L}\Psi$ in the form,

$$i\Gamma \left(-\frac{\hbar^2}{2m} \nabla^2 + V(\mathbf{r}) + g|\Psi(\mathbf{r})|^2 - \mu \right) \Psi(\mathbf{r}),$$

which value will forced to zero at equilibrium by satisfaction of Equation 2.14. Here gamma is a dimensionless value parametrising the relaxation time.

Another property we require is that when $\Gamma = 0$ the $T = 0$ behaviour of the GPE is recovered. This forces us to write $\hat{L}\Psi$ as

$$\hat{L}\Psi = (1 + i\Gamma) \left(-\frac{\hbar^2}{2m} \nabla^2 + V(\mathbf{r}) + g|\Psi(\mathbf{r})|^2 - \mu \right) \Psi(\mathbf{r}),$$

and the equation of motion becomes the DGPE,

$$i\hbar \frac{\partial \Psi(\mathbf{r})}{\partial t} = (1 + i\Gamma) \left(-\frac{\hbar^2}{2m} \nabla^2 + V(\mathbf{r}) + g|\Psi(\mathbf{r})|^2 - \mu \right) \Psi(\mathbf{r}), \quad (2.17)$$

where $\Gamma < 0$ for damping.

Equation 2.17 describes the evolution of the condensate Ψ towards equilibrium, an example of this is shown in Figure 2.2. The process can be understood by considering Ψ

to be made up of a ground state Ψ_0 and a coherent excitation δ ,

$$\Psi = e^{-i\mu t}(\Psi_0 + \delta).$$

The value of δ will approach zero as the wavefunction is evolved via 2.17. The parameter Γ will control the speed of the relaxation and the exact value will change depending on the system. For instance the thermal component of the fluid will largely affect the damping time-scales and so Γ will depend largely on temperature. A microscopic justification for the model is found in [12, 13]; by studying the growth of a condensate in the presence of a rotating thermal cloud an expression for Γ was found.

$$\Gamma = \frac{4m g_c a^2 k T}{\pi \hbar^2}, \quad (2.18)$$

where k is Boltzmann's constant and $g_c = 3$ is a factor used for correction.

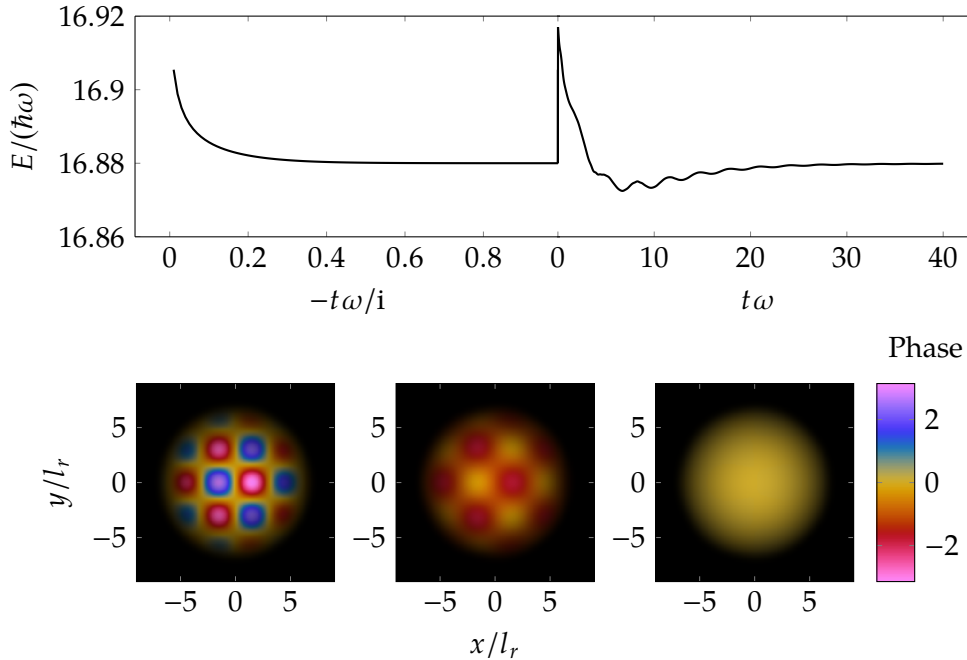


Figure 2.2: Simulated DGPE for a condensate with interaction energy $\hat{g} = 2000$, $\hat{\mu} = 25.27$ and $\gamma = 0.01$. The total energy (upper) is shown during both imaginary and real time. At $\hat{t} = -i$ an excitation is added to the condensate ($\phi \rightarrow \phi + \sin(\hat{x}) \cos(\hat{y})$). The ground state is then re-approached through dissipation. Density and phase are shown (below) at time $\hat{t} = 0$ (left), $\hat{t} = 1$ (center), and $\hat{t} = 40$ (right).

For an arbitrary wavefunction Ψ (that is preferably close to a true solution of the GPE), evolution will indeed approach an equilibrium state. However it is important to note that since now the equation of motion is non-Hermitian, the evolution does not conserve total energy or total atom number. For a fixed chemical potential μ and interaction strength

g , the final equilibrium state may no longer satisfy $\int |\Psi|^2 d\mathbf{r} = N$ and be different from the ground state as found by imaginary time propagation or other eigensolvers. It is therefore necessary to force consistency by either renormalising the wavefunction every time step so that the particle number is constant, or by carefully choosing the value of the chemical potential so that the equilibrium state approached using the DGPE matches the true ground state with correct atom number. The latter of these two methods is perhaps preferred as it is less artificial in nature, and so a numerical technique for finding the ‘correct’ μ for a given value of g is presented in Section [TO BE ADDED]. The evolution shown in Figure 2.2 demonstrates the method of carefully choosing a value of μ .

Some authors [10, 11] write the DGPE in a similar but different way,

$$(i - \gamma)\hbar \frac{\partial \Psi}{\partial t} = \left(-\frac{\hbar^2}{2m} \nabla^2 + V(\mathbf{r}) + g|\Psi|^2(\mathbf{r}) - \mu \right) \Psi(\mathbf{r}), \quad (2.19)$$

where $\gamma > 0$ for damping. Following these authors, this is the form of the DGPE used in numerical simulations in this thesis. Simple algebra shows that while not exactly equal to Equation 2.17, the difference is only in a factor of γ^2 . When $\gamma \ll 1$, which is in most cases, this difference is negligible and makes no difference to qualitative behaviours.

2.9 Finite temperature homogeneous condensate using the classical field method

A common method of simulating finite temperature systems is the classical field methods, also referred to as c-field methods. The classical-field method used in this thesis is investigated and laid out in [14]. The advantage of the classical-field method is that the numerics are no more complicated than simulations of the zero-temperature GPE, instead the meaning of the field Ψ is reinterpreted.

An analysis of the kinetics of a weakly interacting bosonic field was undertaken in [15] and it was demonstrated that under the assumption that the occupation numbers are large, the system evolves as an ensemble of classical fields with corresponding classical-action. In the case of a highly disordered and weakly interacting Bose gas, the state can be viewed as a mixture of coherent modes, each of which evolves (to leading order) along the classical trajectory described by Equation 7.1. The initial condition for numerical simulations of this system must reflect the highly occupied and non-equilibration nature of the Bose gas, and is described in Section 2.14.3.

We emphasise that the requirements of large occupation numbers and weak interactions are essential. Without these requirements quantum modes exist that are coupled to the rest of the system and with occupation number of order unity, and the classical field description breaks down. All Bose gases discussed in this thesis will be of the dilute and

weakly interacting form, so this caveat poses no future trouble. Further discussion and analysis of a highly non-equilibrium Bose gas and the classical-field method can be found in [14].

2.10 Transforming the reference frame

2.10.1 Linearly translating frame

The GPE is transformed into the translating reference frame via the linear momentum operator. In quantum mechanics the momentum operator is defined in position space as $\hat{P} = -i\hbar\nabla$. In our case we wish to translate along a single axis (in most cases the x axis) and so the operator is rewritten so that the momentum is along x only,

$$\hat{Q} = -i\hbar \frac{\partial}{\partial x}.$$

This term can be added to the right hand side of the GPE to modify it such that it is in the reference frame moving along x . For example, the GPE in the frame translating along the x direction with velocity v is written,

$$i\hbar \frac{\partial \Psi(\mathbf{r}, t)}{\partial t} = \left(-\frac{\hbar^2}{2m} \nabla^2 + V(\mathbf{r}, t) + g|\Psi(\mathbf{r}, t)|^2 - \mu - vi\hbar \frac{\partial}{\partial x} \right) \Psi(\mathbf{r}, t), \quad (2.20)$$

2.10.2 Rotating frame

The GPE is transformed into the rotating reference frame via the angular momentum operator. Recall that in classical mechanics that the angular momentum is defined as a vector product of the position \mathbf{r} and the momentum \mathbf{p} ,

$$\mathbf{L} = \mathbf{r} \times \mathbf{p} = \begin{vmatrix} i & j & k \\ x & y & z \\ p_x & p_y & p_z \end{vmatrix}.$$

In quantum mechanics the corresponding position and momentum *operators* are defined as $\hat{R} = \mathbf{r}$ and $\hat{P} = -i\hbar\nabla$, and so we can define a similar angular momentum *operator*,

$$\hat{L} = \hat{R} \times \hat{P}. \quad (2.21)$$

Components of equation 2.21 can also be written as differential operators,

$$\hat{L}_x = -i\hbar \left(y \frac{\partial}{\partial z} - z \frac{\partial}{\partial y} \right), \quad \hat{L}_y = -i\hbar \left(z \frac{\partial}{\partial x} - x \frac{\partial}{\partial z} \right), \quad \hat{L}_z = -i\hbar \left(x \frac{\partial}{\partial y} - y \frac{\partial}{\partial x} \right), \quad (2.22)$$

which can then be added to the right hand side of the GPE to modify it such that it is in the rotating reference frame. For example, the GPE in the frame rotating about the z axis with angular momentum Ω is written,

$$i\hbar \frac{\partial \Psi(\mathbf{r}, t)}{\partial t} = \left(-\frac{\hbar^2}{2m} \nabla^2 + V(\mathbf{r}, t) + g|\Psi(\mathbf{r}, t)|^2 - \mu - i\hbar\Omega \left[x \frac{\partial}{\partial y} - y \frac{\partial}{\partial x} \right] \right) \Psi(\mathbf{r}, t), \quad (2.23)$$

2.11 Hydrodynamic interpretation

Often it can be helpful to write the GPE, via the so called Madelung transformation, as a set of hydrodynamic equations. The transformation reinterprets the wavefunction Ψ as a magnitude directly related to the fluid density and a phase which is directly related to the fluid velocity. We write the wavefunction in the form

$$\Psi(\mathbf{r}, t) = R(\mathbf{r}, t) \exp(i\theta(\mathbf{r}, t)), \quad (2.24)$$

and identify the fluid density as $\rho = mR^2$ and the velocity as $\mathbf{v} = \frac{\hbar}{m} \nabla \theta$. In vector form we obtain a continuity equation

$$\frac{\partial \rho}{\partial t} + \nabla(\rho \mathbf{v}) = 0, \quad (2.25)$$

and an equation similar to the Euler equation for an inviscid fluid,

$$\rho \left(\frac{\partial \mathbf{v}}{\partial t} + (\mathbf{v} \cdot \nabla) \mathbf{v} \right) = -\nabla p - \nabla \mathbf{P} - \rho \nabla \left(\frac{V}{m} \right). \quad (2.26)$$

where $P_{jk} = -\frac{\hbar^2}{4m^2} \rho \frac{\partial^2 \ln \rho}{\partial x_j \partial x_k}$. A detailed derivation of this result can be found in Appendix A.3.

2.12 Quantised Circulation

An interesting feature of the GPE is that the fluid circulation must be quantised. We can see this by first writing the integrated change of phase along any closed curve C ,

$$\Delta\theta = \oint_C \nabla \theta \cdot d\mathbf{l}, \quad (2.27)$$

where $d\mathbf{l}$ is the line element. The wavefunction at the start and the end of the integration must be single valued, and so

$$\exp(i\theta_0) = \exp(i\theta_0) \exp(i\Delta\theta), \quad (2.28)$$

for some θ_0 . This is only satisfied when $\Delta\theta = 2\pi q$, with $q \in \mathbb{Z}$. Our local velocity is $\mathbf{v} = \frac{\hbar}{m}\nabla\theta$ and so we can write

$$\Gamma = \oint_C \mathbf{v} d\mathbf{l} = \frac{2\pi\hbar}{m}q. \quad (2.29)$$

Notice that we are now taking the line integral of the velocity; we have a formula for the circulation. We find the circulation must be quantised in units of $\kappa = 2\pi\hbar/m$, the so called ‘quantum of circulation’. This is in stark contrast to classical fluids where the circulation can take any real value.

2.13 A selection of simple solutions

Due to the nonlinearity of the GPE fully analytical solutions are rare. However, there are a selection of solutions available for simple cases that allow us to gain insight into the behaviour of a fluid governed by the GPE in more complicated scenarios.

2.13.1 Density near a wall

Consider a stationary ($\partial\Psi/\partial t = 0$) solution of the 1D-GPE with no trapping potential ($V(x, t) = 0$) and boundary conditions $\Psi(0) = 0$ (representing a hard wall boundary at $x = 0$) and $\Psi(x) = \sqrt{\mu/g}$ as $x \rightarrow \infty$. The 1D-GPE becomes

$$-\frac{\hbar^2}{2m} \frac{\partial^2}{\partial x^2} \Psi + g\Psi|\Psi|^2 - \mu\Psi = 0, \quad (2.30)$$

which is solved by,

$$\Psi(x) = \sqrt{\frac{\mu}{g}} \tanh\left(\frac{x}{\xi}\right). \quad (2.31)$$

This solution is shown in Figure 2.3. We gain insight through this analytical solution

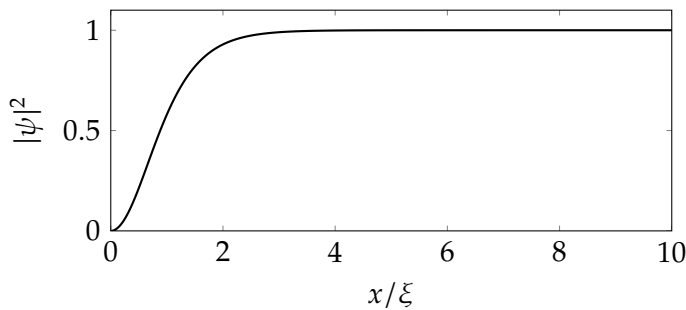


Figure 2.3: A fluid governed by the homogenous GPE healing at a hard wall at $x = 0$.

for how a fluid governed by the GPE ‘heals’ near areas of low density. There is clearly a natural minimum distance, related to ξ , over which the wavefunction can change from

a density of zero to its homogeneous value. This behaviour appears many times in the context of superfluids, from solitons and solitary waves in low dimensional systems, to the fluid behaviour near impurities and vortex lines and tubes in fully 3D systems.

2.13.2 Soliton solutions

Due to its nonlinear nature, solutions of the GPE can support localised non-dispersive waves packets known as solitons. Two flavours of solitons can form in 1D, so called bright or dark solitons. Bright solitons form when interactions between particles are attractive ($g < 0$), however, as no physically relevant simulations in this thesis occur in this range we do not focus on these solitons. Dark solitons form when the interaction term is repulsive ($g > 0$) and physically consist of a dip in the density along with a phase slip of up to a value of π . When the density dips to zero, the phase slip is equal to π and the velocity of the soliton is $v = 0$. Dark solitons with $v > 0$ have a density dip that does not quite reach zero and a smaller valued, smooth phase slip. The 1D dark soliton solutions, derived in the 70s [16, 17], take the general form,

$$\Psi(x, t) = \sqrt{\rho} \exp\left(-\frac{i\mu}{\hbar}t\right) \left\{ \sqrt{1 - \frac{v^2}{c^2}} \tanh \left[\sqrt{1 - \frac{v^2}{c^2}} \frac{(x - vt)}{\xi} \right] + \frac{iv}{c} \right\}, \quad (2.32)$$

where v is the velocity of the soliton and c is the speed of sound. Examples of dark solitons are seen in Figures 2.4 and 2.5.

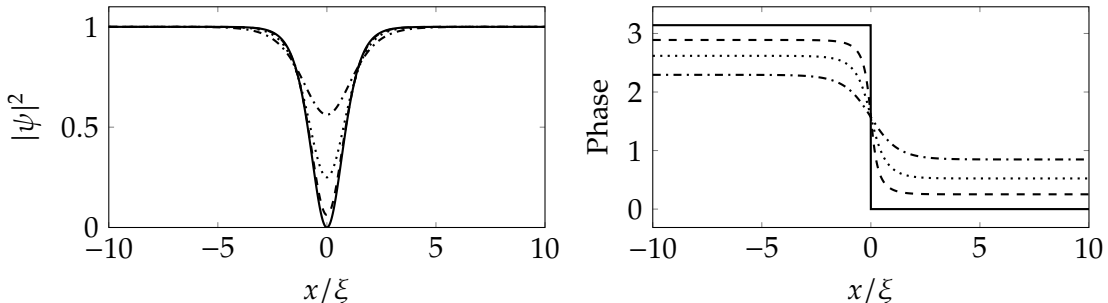


Figure 2.4: Density (left) and phase (right) of solitons in a 1D homogeneous system moving at speed $v = 0$ c (solid), $v = 0.25$ c (dashed), $v = 0.5$ c (dotted) and $v = 0.75$ c (dash-dotted).

Solitonic waves can exist in higher dimensional systems, but these are not solitons in the strict mathematical sense; the structures are unstable, and decay due to the snake instability [18, 19]. Nevertheless, long living stable solitary waves can exist, particularly in quasi-1D geometries [20].

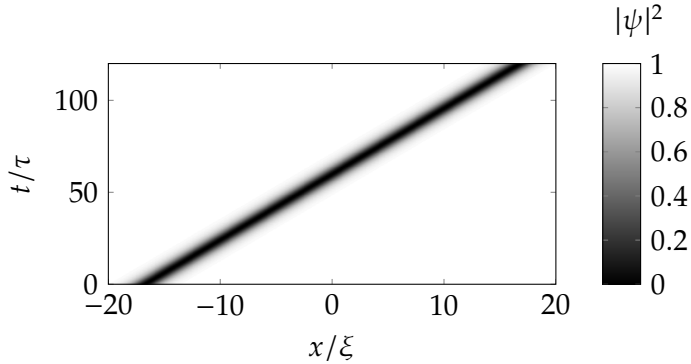


Figure 2.5: Density over time of a 1D fluid containing a soliton with speed $v = 0.25c$, confirming the non-dispersal nature of the wavepacket.

2.13.3 Quantised Vortices

We have already seen in section 2.12 that rotation in a fluid governed by the GPE must be quantised. Both two and three-dimensional solutions of the GPE can support vortices and vortex lines as a carrier of quantised vorticity. They are defined by a singularity in the phase, along with a corresponding dip in density. This density dip masks the phase singularity, which is related to the fluid velocity, and so avoids solutions with infinite energy density.

The 2D quantised vortex core solution (or equivalently the solution in the plane perpendicular to a straight line 3D vortex) is circularly symmetric and can be written in polar coordinates as

$$\psi(\mathbf{r}, \varphi) = f_v(r) \exp(ni\varphi), \quad (2.33)$$

where $n \in \mathbb{Z}$ is the charge or winding number of the vortex. Vortex solutions can be found numerically using the imaginary time propagation method outlined in Section 2.6 and an example 2D solution with $n = 1$ is shown in Figure 2.6.

No analytic form exists for the shape of the vortex core, $f_v(r)$, and it must be approximated or calculated numerically. A useful approximation for the shape of the core when $n = 1$ is the Padé approximation outlined in [21],

$$f_v(r) = \sqrt{\frac{0.6874(r/\xi)^2 + 0.1144(r/\xi)^4}{1 + 0.6666(r/\xi)^2 + 0.1144(r/\xi)^4}}, \quad (2.34)$$

which captures the correct vortex core asymptotic behaviour for $r \rightarrow 0$ and $r \rightarrow \infty$ and is close to the true vortex solution everywhere. A comparison of the Padé approximation and the true ($n = 1$) vortex solution is shown in Figure 2.7 (a). Note that the density dip heals over a radius on the order of 5ξ . While the density heals over a short area around the vortex, the presence of a vortex changes the phase in the entirety of the fluid; vortices are

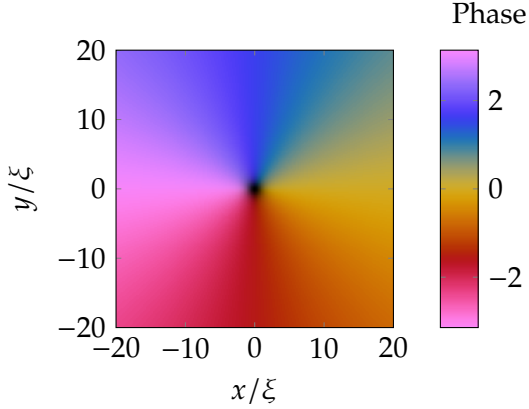


Figure 2.6: Density and phase of a vortex at $(x, y) = (0, 0)$ with $n = 1$, found numerically with the GPE in imaginary time. Note how the density dip at the vortex centre masks the phase singularity from the fluid.

a truly a non-local phenomenon and multiple vortices can interact even when separated much further than the size of their density cores.

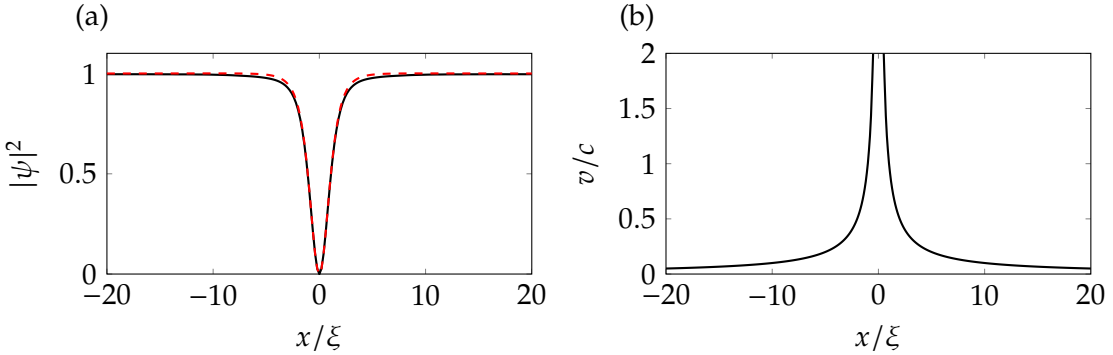


Figure 2.7: (a) A comparison of the true vortex solution (black solid line) at $x = 0$, found by numerically propagating the GPE in imaginary time, and the Padé approximation (red dashed line) for a vortex core with a charge of $n = 1$. (b) Fluid velocity in the vicinity of a vortex at $x = 0$ with charge $n = 1$.

As seen in Section 2.11, the velocity of the fluid can be written $\mathbf{v} = \frac{\hbar}{m} \nabla \theta$, where θ is the phase. We can use this with Equation 2.33 to find the velocity of the fluid around a vortex,

$$\mathbf{v}(\mathbf{r}, \varphi) = \frac{n\hbar}{mr} \hat{\boldsymbol{\varphi}}. \quad (2.35)$$

Note the $v \propto 1/r$ dependence in the speed of the fluid around the vortex, demonstrated in Figure 2.7 (b).

2.14 Initial Conditions

When numerically solving the GPE, an initial condition must be chosen. Correct choice of initial condition is important for accurate simulation of dynamics. If an unstable initial condition is chosen far from the ground state solution, noise and other excitations such as solitary waves and vortices may be generated that interfere with any measurements and studies undertaken at later times in the numerical computation. A selection of appropriate non-violent initial conditions are outlined in this section.

2.14.1 Homogeneous initial condition

When the potential term $V = 0$, the condensate ground state becomes homogeneous with density $\rho = \mu/g$. In this case, a stationary solution of the GPE is as simple as setting the ground state density everywhere,

$$\Psi = \sqrt{\frac{\mu}{g}}. \quad (2.36)$$

2.14.2 Thomas-Fermi profile of a trapped condensate

Consider an initial condition that is stationary in time, but has a non-zero potential and so varies in space. Such a condition will necessarily satisfy 2.14, the time-independent GPE. Let us assume that we have a strongly repulsive interaction term ($g \gg 0$). In this case, as an approximation we can neglect the kinetic energy term in the solution as it will be negligible compared to the strength of the repulsive atom-atom interactions. We write

$$\mu\Psi(\mathbf{r}) = (V(\mathbf{r}) + g|\Psi(\mathbf{r})|^2)\Psi(\mathbf{r}), \quad (2.37)$$

which can be simplified as,

$$|\Psi(\mathbf{r})|^2 = \frac{\mu - V(\mathbf{r})}{g}. \quad (2.38)$$

From this result, we then construct an approximate solution,

$$\Psi(\mathbf{r}) = \begin{cases} \sqrt{\frac{\mu - V(\mathbf{r})}{g}} & \text{if } \mu \geq V(\mathbf{r}), \\ 0 & \text{otherwise.} \end{cases} \quad (2.39)$$

This is known as the Thomas-Fermi (TF) profile and is extremely useful as an approximate initial condition for modelling a trapped atomic condensate. The approximation is accurate near the centre of the condensate, but fails near the condensate edge, where the tails of the true density distribution are not captured. Nevertheless Figure 2.8 demonstrates the high accuracy of the approximation. Due to the discrepancy at the tails of the condensate density, it is often the case that the TF profile is used as an initial guess for numerical

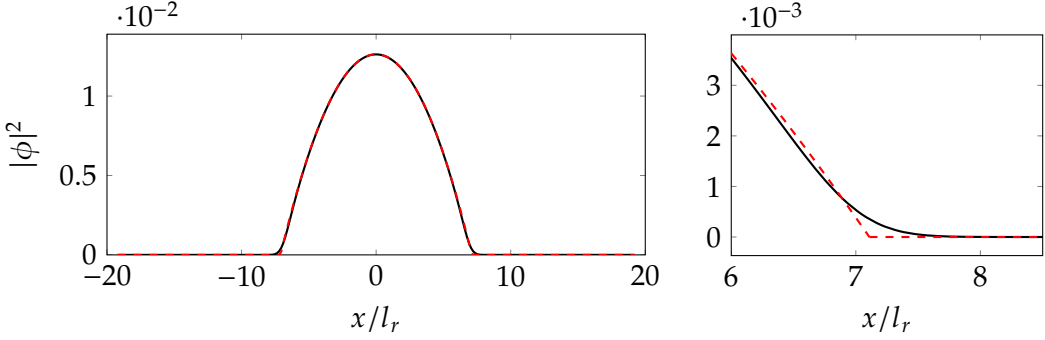


Figure 2.8: Comparison of the TF profile (red dashed line) and the true trapped harmonic oscillator ground state (black solid line) as found by numerical solution of the GPE in imaginary time. The TF profile fits extremely well over most of the condensate density (left), however fails at capturing the smooth tails of the density distribution (right). Here the TF radius is approximately $R_{\text{TF}} = 7.1 l_r$, and can be identified as a kink in the TF profile.

eigensolvers, which then find a time-independent numerical solution to be used as the true initial condition.

The TF solution provides a useful analytic approximation for the size of a condensate. The perimeter of the fluid occurs approximately when $\mu = V(\mathbf{r})$, and so the approximate Thomas-Fermi radius of the condensate is,

$$R_{\text{TF}} = \sqrt{\frac{2\mu}{m\omega_r^2}}. \quad (2.40)$$

The TF radius is an useful indicator of length scales when working with analytical descriptions of condensate behaviours in a trapped system.

2.14.3 Classical field initial condition

In numerical simulation of a finite temperature Bose gas, we begin with a highly non-equilibrium state, so that the low-lying coherent modes of the system are all highly occupied.

$$\psi_{\text{neq}}(\mathbf{r}) = \sum_{\mathbf{k}}^{k < k_{\max}} a_{\mathbf{k}} \exp(i\mathbf{k} \cdot \mathbf{r}), \quad (2.41)$$

where the complex Fourier amplitudes $a_{\mathbf{k}}$ are related to the occupation numbers $n_{\mathbf{k}}$ through $\langle a_{\mathbf{k}} a_{\mathbf{k}'}^* \rangle = n_{\mathbf{k}} \delta_{\mathbf{k}\mathbf{k}'}$. The phase of the complex amplitudes $a_{\mathbf{k}}$ are distributed uniformly on $[0, 2\pi]$ while $|a_{\mathbf{k}}|$ is distributed randomly with fixed mean equal to unity; it has been found that different distributions of $|a_{\mathbf{k}}|$ make no qualitative difference to the turbulent evolution [14]. A momentum cutoff, $k < k_{\max}$, is introduced to limit the momentum of the low lying modes, and in harmonic systems can be imposed as an energy-cutoff during evolution using the Projected-GPE [22]. However, in the case of homogeneous finite temperature

simulations the momentum cut-off arises naturally as a consequence of the discretisation of the system; for a 3D finite temperature simulation in a periodic box with uniform grid spacing Δ , $k_{\max} = \sqrt{3}\pi/\Delta$.

The numerical initial condition $\psi(\mathbf{r}, t_0)$ is then determined by renormalisation of $\psi_{\text{neq}}(\mathbf{r})$ to fix the number density, N/V and kinetic energy density, E_{kin}/V . The choice of N/V and E_{kin}/V uniquely determines the condensate fraction, and therefore the temperature for the equilibrium state of the Bose gas.

2.15 Creating obstacles with repulsive potentials

In ultra-cold atomic gas experiments, perturbations to the gas can be achieved using laser beams. A red-detuned laser beam can create areas of attraction, and conversely, blue-detuned laser beams can create areas of repulsion. Should the blue-detuned laser beam be bright enough, a localised ‘hole’ in the condensate can be formed where there are no atoms. Similarly, in superfluid helium experiments, there are examples where the fluid can feel the presence of a wall, wire, spheres or ion bubbles[CITE]. These effects are replicated in the GPE model through the use of two and three-dimensional Gaussian or hard wall potentials.

2.15.1 Three-dimensional elliptical Gaussian

In our 3D simulations the localized obstacle is modelled via a repulsive Gaussian potential,

$$V_{\text{obj}}(\mathbf{r}) = V_0 \exp\left(-\frac{\varepsilon^2(x - x_0)^2}{d^2} - \frac{(y - y_0)^2}{d^2} - \frac{(z - z_0)^2}{d^2}\right), \quad (2.42)$$

where V_0 is its amplitude, d its width in the y and z directions, and (x_0, y_0, z_0) its coordinates. ε parametrises the ellipticity of the obstacle, a value of $\varepsilon = 1$ corresponds to a spherical obstacle, a higher value of ε ‘squashes’ the obstacle along x , forming a pancake shape.

2.15.2 Two and Three-dimensional cylindrical Gaussian

In addition to spheres, we model cylindrical potentials as a Gaussian,

$$V_{\text{obj}}(\mathbf{r}) = V_0 \exp\left(-\frac{\varepsilon^2(x - x_0)^2}{d^2} - \frac{(y - y_0)^2}{d^2}\right), \quad (2.43)$$

where V_0 is its amplitude, d its width in the y direction, and (x_0, y_0, z_0) its coordinates. ε parametrises the ellipticity of the Gaussian (experimentally feasible with laser beam focusing or masking), so that a value of $\varepsilon = 1$ corresponds to a circular shaped hole. In 3D

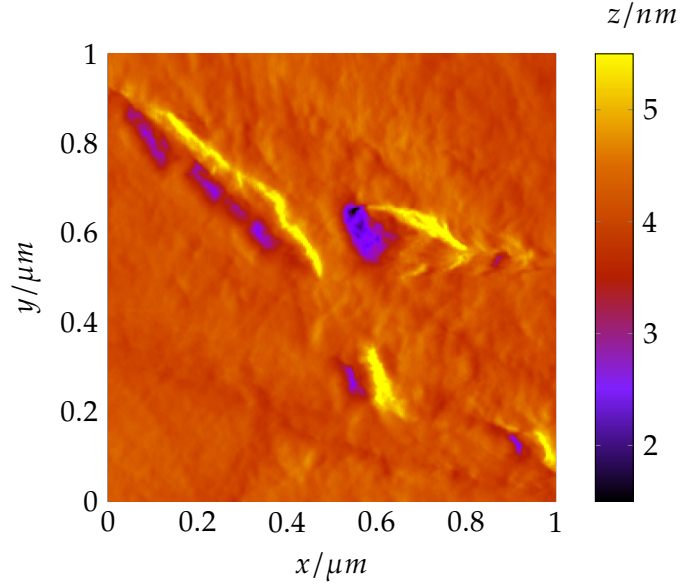


Figure 2.9: An atomic force microscope (AFM) image showing the microscopic detail on the surface of a single–core NbTi ‘floppy’ wire used for generating superfluid turbulence. This data was kindly provided by C. R. Lawson [23].

the Gaussian hole is extended across the entire z dimension forming a cylindrical shaped barrier.

2.15.3 Three-dimensional ‘realistic’ rough-surface

In many superfluid helium experiments [24], turbulence is generated by moving grids [25], wires [26, 27, 28, 29, 30], forks [31, 32] or spheres [33]. Although macroscopically polished, the surface of these objects is rough on the length scale of the superfluid vortex core, which is of the order of 10^{-10} m in ^4He and 10^{-8} m in ^3He . As an example, Fig. 2.9(a) is an atomic force microscope (AFM) image showing the microscopic detail on the surface of a single–core NbTi ‘floppy’ wire used for generating superfluid turbulence [28]. Note the appearance of an elongated scratch, typical of such wires.

We can simulate the microscopic detail through the use of a potential derived from sample AFM height-map data. We define the external potential to be,

$$V_{\text{obj}}(\mathbf{r}) = \begin{cases} V_0 & \text{if } z < (h(\alpha x, \alpha y) - z_0) \\ 0 & \text{if } z > (h(\alpha x, \alpha y) - z_0), \end{cases} \quad (2.44)$$

where V_0 is its amplitude, z_0 is a shift in height and α is a scaling factor. Scaling $h(x, y)$ acts as a crude way of varying the roughness of simulated boundaries. Finally, a Gaussian blur is applied so that $V(x, y, z)$ is smooth in z .

Chapter 3

Numerical Theory and Procedures

3.1 Numerical procedures for 2D and 3D solutions

3.1.1 Fourth order Runge-Kutta scheme

The classical fourth-order Runge-Kutta formula (RK4) is described equivalently in many texts. We follow the description in [6]. Let an initial value problem be specified as

$$\frac{\partial \psi}{\partial t} = f(\psi, t), \quad \psi(t_0) = \psi_0.$$

A step-size, $h > 0$, is chosen as the parameter controlling how the solution is advanced over t . The scheme for estimating $\psi(t_n) = \psi_n$ is then written

$$\begin{aligned} k_1 &= h f(t_n, \psi_n), \\ k_2 &= h f\left(t_n + \frac{h}{2}, \psi_n + \frac{k_1}{2}\right), \\ k_3 &= h f\left(t_n + \frac{h}{2}, \psi_n + \frac{k_2}{2}\right), \\ k_4 &= h f(t_n + h, \psi_n + k_3), \\ \psi_{n+1} &= \psi_n + \frac{k_1}{6} + \frac{k_2}{3} + \frac{k_3}{3} + \frac{k_4}{6} + O(h^5), \\ t_{n+1} &= t_n + h. \end{aligned} \tag{3.1}$$

An outline derivation of the Runge-Kutta scheme, which includes a proof of accuracy are shown in Appendix A.1. In all of our relevant calculations the value of f is set as the right hand side of the homogeneous or trapped GPE. The main loop formulating the RK4 method may be repeated indefinitely to reach any $t > t_0$. The step size for a given set of parameters should be chosen small enough that smaller choices make no quantitative

changes to the resulting solution. The following section outlines the methods we have implemented to ensure numerical solutions are converged.

3.1.2 Numerical stability and convergence

We now investigate numerical parameters which affect the stability of simulated superfluid systems. Our direct aim is to find a suitable discretisation of space and time so that while simulations are timely, our numerical quantities are converged (so that they are not sensitive to small changes in computational parameters) and that quantities conserved by the equations of motion are indeed conserved in the computed numerical solutions.

We begin by estimating Δ_x , the required spatial grid spacing, by considering the width of the vortex core in a homogeneous system, a feature we would like well and accurately visualised in our numerical solutions. Through observation of a singly quantised vortex core (as in Figure 2.7) we observe a core radius of approximately 5ξ when the background density is $\rho = 1$. To ensure the vortex core structure is well resolved we decide to dedicate 10 grid points for a vortex core radius, suggesting a value of $\Delta_x = \xi/2$.

In the trapped case we can use the same idea. It is shown in Section B.3 that $\xi = \hbar/\sqrt{mg}$ for $\rho = 1$. We can then easily rearrange to find an expression for ξ in the harmonic oscillator units of trapped condensates. We find that our approximate grid spacing to adequately resolve the vortex core is $\Delta_x = 0.5\xi = 0.5\omega\sqrt{\hbar/(\mu\omega)}l_r$. As an example, for a trapped condensate with interaction energy $\hat{g} = 2000$, chemical potential $\hat{\mu} = 25.27$ and trap frequency $\omega = 8.75$ Hz we find that a value of $\Delta_x = 0.1l_r$ should be adequate.

Similar arguments (concerned with time rather than space), can be used to approximate a suitable time step h . We define a time period that we would like to be well resolved by considering by the smallest possible element moving at the fastest reasonable speed. If we define this period as $\Delta_x/5c$ and allocate to it 10 time steps, we find that $h = 0.5\xi/50c = 0.01\tau$.

In addition to this process, for each set of simulation parameters it is recommended to confirm the suitability of the chosen Δ_x and h by testing the convergence and conservation in the numerical methods. The total condensate energy and particle number are good measures for this as they should both be well conserved by the GPE with a dissipation of $\gamma = 0$. An example of this process (confirming the suitability of a chosen Δ_x) is shown in Figure 3.1: For a large $\Delta_x = 0.4l_r$, both the condensate energy and norm fluctuate wildly. For $\Delta_x = 0.1l_r$, the norm is extremely well conserved to within $2.10^{-5}\%$ and the energy is conserved within $5.10^{-3}\%$. The smallest tested value of $\Delta_x = 0.05l_r$ finally confirms that the energy has converged. We conclude that for the chosen system parameters that $\Delta_x = 0.1l_r$ (the value suggested by the above analysis) is numerically sufficient and there is little reason to use $\Delta_x < 0.1l_r$.

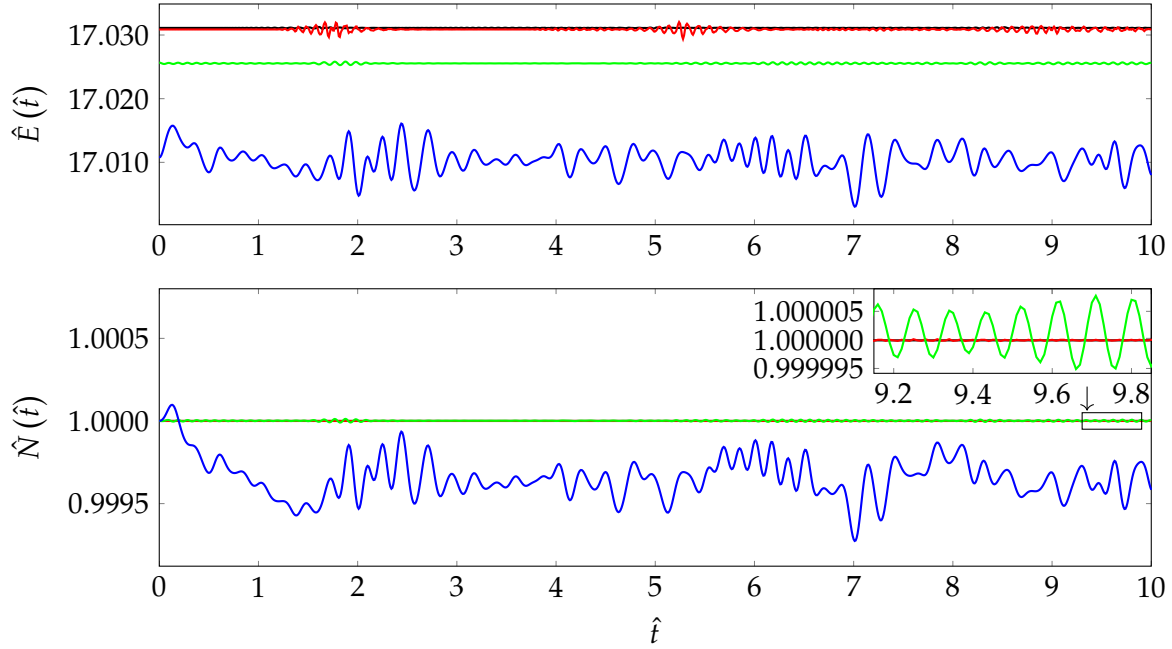


Figure 3.1: Dimensionless energy, \hat{E} , and particle number, \hat{N} , throughout numerical propagation of a trapped condensate containing a singly quantised vortex in its center, with interaction energy $\hat{g} = 2000$ and chemical potential $\hat{\mu} = 25.27$. The numerical grid width varies with each line; $\Delta_x = 0.05$ (black), $\Delta_x = 0.1$ (red), $\Delta_x = 0.2$ (green) and $\Delta_x = 0.4$ (blue). (Inset) Zoomed view of the \hat{N} .

3.2 Identifying vortices

Large portions of this thesis are dedicated to the study of 2D vortex dynamics. As such, accurate detection of the location and charge of densely packed quantised 2D vortices is required, and so we have developed robust numerical methods for vortex identification. The basic idea is fairly simple, with arguments similar to those used to demonstrate the quantised nature of the circulation.

As shown in Section 2.12, the integrated change of phase along any closed curve C is,

$$\Delta\theta(C) = \oint_C \nabla\theta \cdot d\mathbf{l} = 2\pi q, \quad (3.2)$$

where $d\mathbf{l}$ is the line element and $q \in \mathbb{Z}$. Further, the fundamental theorem of calculus for line integrals[CITE] implies that $\Delta\theta(C) = 0$, providing that C is continuous and does not encompass a phase singularity. This result is crucial; it allows us to directly state that a vortex lies within C if and only if $|\Delta\theta(C)| > 0$.

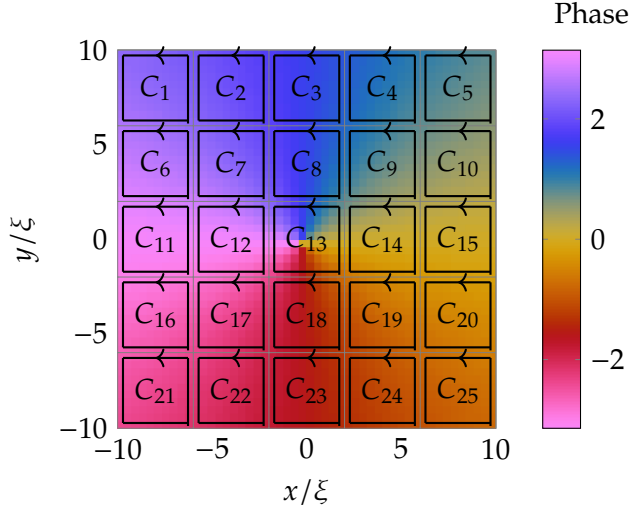


Figure 3.2: The phase for a homogeneous system with a vortex located at $(0,0)$. Also shown is an example set of curves C_k for vortex identification. All $\Delta\theta(C_{k \neq 13}) \approx 0$, and $\Delta\theta(C_{13}) > 0$. The conclusion is that a positive vortex lies in the region defined by C_{13} .

3.2.1 Basic vortex detection method

First define a set of curves C_k with each curve lying on points of our numerical grid, so that a single C_k encompasses only a small region of the fluid (ideally, C_k should encompass a region at most the diameter of a vortex core). $\Delta\theta(C_k)$ is then approximated for each k using numerical differentiation (2nd order finite differences) and numerical line integration (trapezium or Simpson rule). If $\Delta\theta(C_k) = 0$ to within numerical accuracy then we determine that the region inside C_k contains no vortices. Otherwise the sign of $\Delta\theta(C_k)$ tells us the polarity of the encompassed vortex.

In principle the result also allows us to calculate the exact charge of a vortex in terms of the quantum of circulation. However, for accurate determination of vortex location the curves C_k must encompass a very small area, contain few grid points, and so accuracy is low. We use only the sign of the $\Delta\theta(C_k)$ so that the integration error makes minimal difference and results in an accurate detection of vortex polarity and location. As multiply charged ($|q| > 1$) vortices are unstable (rapidly decaying into several singly charged vortices) there is no significant loss of information in practise.

3.2.2 Visualising vortex location with a vortex field

The basic vortex identification method set out in Section 3.2.2 is quick to implement and useful when there are few well separated vortices, but one can easily imagine a situation where the system fails. One such case would be two vortices both lying within a single C_k curve; in the case of two similarly charged vortices only a single vortex would be detected

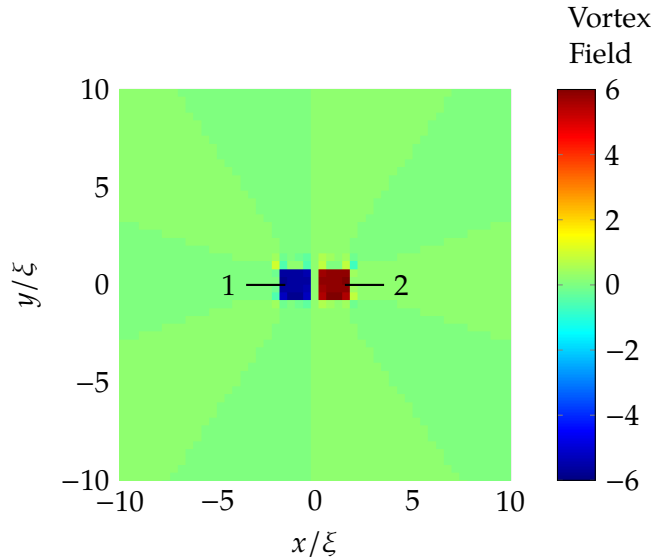


Figure 3.3: Vortex field for two oppositely charged vortices located at $(-\xi, 0)$ and $(\xi, 0)$ in a homogeneous system. The positive (negative) vortex leads to a positive (negative) quantity in the vortex field. In addition, the output of the bwlabel algorithm is labelled.

or in the case of two oppositely charged vortices potentially none at all!

The solution is not always as simple as reducing the size of C_k , vortices can be densely packed and there are often too little grid points to make this reasonable. Instead, curves with a width around the diameter of a vortex core are again used, but for every grid point (taking into account boundary conditions) the curve $C_{[i,j]}$ is defined surrounding and centred on the grid point $[i, j]$. A vortex field can then be visualised by visualizing the 2D plot of $\Delta\theta(C_{[i,j]})$. Algorithm 2 describes the process in detail. As before, areas where $|\Delta\theta(C_{[i,j]})| > 0$ (to within numerical accuracy) signify the presence of a vortex. Figure 3.3 demonstrates a vortex field obtained from a homogeneous system with a negative vortex located at $(-\xi, 0)$ and a positive vortex located at $(\xi, 0)$. It can be easily seen where the two vortices are located in the wavefunction by direct observation of the 2D vortex field.

For every vortex detected by this algorithm, the corresponding area in the vortex field is composed of several adjoined points in the numerical grid. For correct vortex counting, these multiple points must be classified as a single vortex. The bwlabel algorithm described in Algorithm 5 is used to obtain this required classification. The algorithm takes the vortex field as input and assigns each connected component a label. An example output of bwlabel is shown in Figure 3.3. To find the vortex location for a given label, we simply take the mean of all the x and y locations of points with the same label.

The algorithm described in this section leads to more accurate vortex counts when vortices are densely packed. As a bonus the accuracy of detected vortex location is improved; the final output is a combination of information from several curves $C_{[i,j]}$, and so in good

conditions the result is often sub-pixel accurate (that is, the algorithm output is accurate even if the phase singularity corresponding to a vortex lies between grid points).

3.2.3 Further improving accuracy with a Gaussian blur

When using Algorithm 2 in ‘messy’ wavefunctions (containing many vortices and waves), artefacts of the incorrect sign can be introduced by the numerical discretisation, differentiation and integration errors. Faint examples of these artefacts can be seen in Figure 3.3 surrounding the two labelled regions. These artefacts are spatially small (on the scale of Δ_x) and so can be corrected by removing all high frequency spatial waves from the vortex field using low-pass filtering. A common low-pass filter is the Gaussian blur [CITE], applied using a convolution. The Gaussian blur algorithm is described in Algorithm 4 and the result of applying the algorithm to the vortex field is shown in Figure 3.4. Note how the incorrectly signed artefacts surrounding the detected vortex regions are now removed.

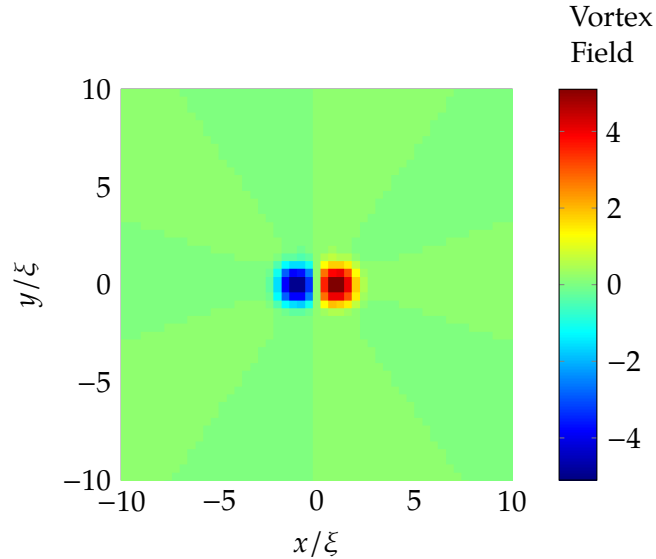


Figure 3.4: Smoothed vortex field for two oppositely charged vortices located at $(-\xi, 0)$ and $(\xi, 0)$ in a homogeneous system. The high frequency noisy artefacts in the vortex field are removed by the low-pass filtering.

A by-product of applying a low-pass filter to the vortex field is that sharp edges in structures are blurred and spread out. To identify vortex locations a threshold function is therefore used before performing the `bwlabeled` algorithm, i.e vortices are identified when $|\Delta\theta(C_{[i,j]})| > \Delta_{th}$, where $\Delta_{th} > 0$ is some threshold. Δ_{th} can be tweaked to make the vortex detection more or less sensitive (for either detecting vortices more easily in messy systems, or to ignore weak spurious signals in the vortex field) and in general will vary for each system.

3.2.4 Avoiding ‘ghost vortices’

A common problem when detecting vortices is the prevalence of invalid or uninteresting phase defects inside obstacles or when considering trapped condensates. In areas where the density is exactly zero the system phase becomes undefined. Depending on how the simulation is implemented these areas may fill with small numerical noise and cause many singularities to be detected. A similar phenomenon occurs in areas of near-zero density; well-defined singularities in the phase form but with an ill-defined vortex core in the density [10]. Examples of these vortices are shown in the low density regions of Figure 3.5. As these singularities carry negligible angular momentum and energy they are of no interest and are termed ‘ghost vortices’.

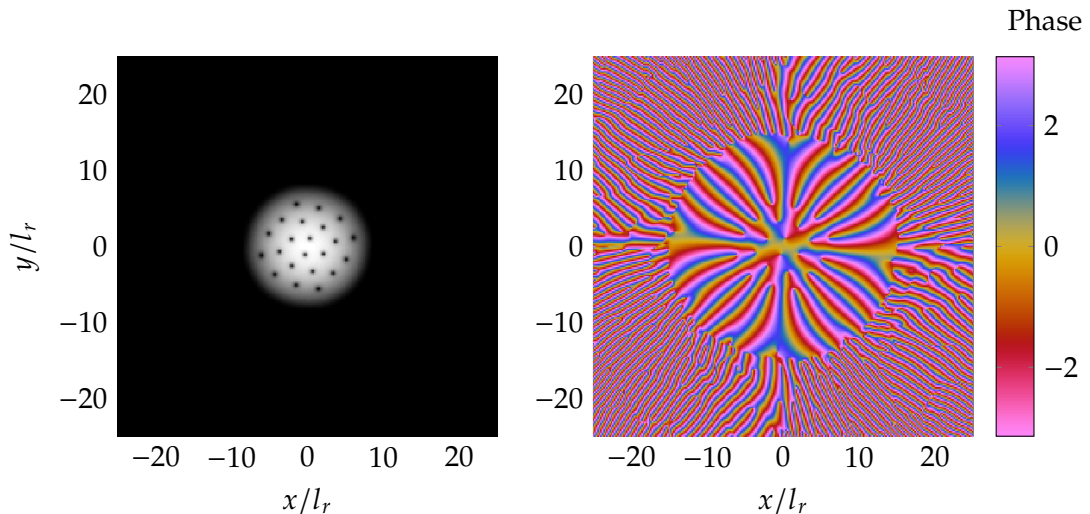


Figure 3.5: A trapped rotating condensate with $\Omega = 0.7$, $\hat{g} = 2000$ and $\hat{\mu} = 25.27$. Ghost vortices can be seen in the phase as singularities where the corresponding density is near-zero.

A simple way to remove ghost vortices is to use a mask to hide vortices found in low-density regions in trapped systems and inside obstacles. While on the one hand it is easy to define a mask using the TF radius or considering where $V_{\text{trap}} + V_{\text{obj}} > 1$, masks are quite arbitrary in nature and an overzealous mask may hide details. Additionally, any condensate with certain excitations such a breathing mode or centre of mass oscillation will periodically extend beyond a hard coded mask.

An alternative method to avoid identifying ghost vortices presents itself when implementing Algorithm 2. The vortex field can be multiplied by the wavefunction density at every point *before* performing the Gaussian convolution step. The result is that in low-density areas the vortex field becomes completely zero and singularities in this region are no longer identified as vortices. At the centre of vortex cores the vortex field also goes to zero. However, enough vortex information remains in the vortex field in the vicinity of

the vortex cores that vortices in high-density regions are still identified accurately after the Gaussian convolution. As before, the threshold value Δ_{th} controls the sensitivity of this algorithm, in particular for detecting vortices in the low density regions of the condensate. Algorithm 3 describes this method in further detail and Figure 3.6 shows the vortex field with and without the added step of multiplying by the density, demonstrating that the ghost vortices detected when using Algorithm 2 are indeed removed when using Algorithm 3.

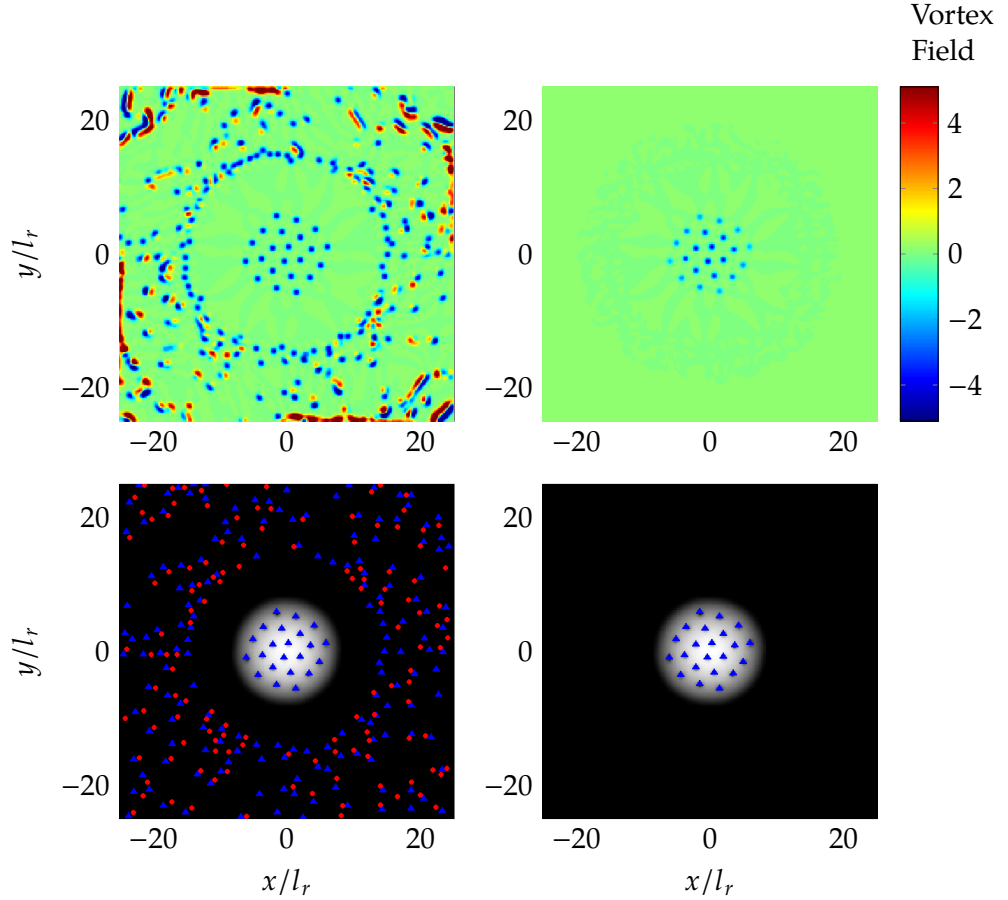


Figure 3.6: Identifying vortices within a trapped rotating condensate with $\Omega = 0.7$, $\hat{g} = 2000$ and $\hat{\mu} = 25.27$. (a) The smoothed vortex field using Algorithm 2, (b) the smoothed vortex field using Algorithm 3, (c) the system density with vortices identified using Algorithm 2, and (d) the system density with vortices identified using Algorithm 3. The ghost vortices seen in (a,c) are removed in (b,d).

3.3 Quantifying vortex clustering in 2D

With the ability to detect vortex polarity and locations in 2D, we can begin to better understand vortex distribution and statistics in simulations. In this section we describe the various methods of quantifying vortex distribution, both simple and complex.

3.3.1 Vortex counting

The simplest method of ascertaining vortex statistics is to simply count the number of vortices, N_v , in the entire system. A further obvious decomposition of this quantity is to count the number of positive and negative vortices separately, designated N_+ and N_- respectively. With this information we can define an interesting property of a system's vortex distribution,

$$P_v = \frac{N_+ - N_-}{N_v}, \quad (3.3)$$

where P_v is known as the polarity of the system. This quantity takes values in the range $[-1, 1]$; when there are only positively (negatively) charged vortices in the system $P_v = 1$ ($P_v = -1$), and when there are equal quantities of positive and negatively charged vortices $P_v = 0$.

3.3.2 Ripley's K and L functions

While counting vortices as in Section 3.3.1 is a great way to gain statistics of the distribution of vortices in terms of vortex charge, the quantities tell us nothing about how vortices are located in space. The problem of spatial descriptive statistics is an old one and measures of spatial dispersion or homogeneity have in the past been applied to several datasets consisting of point locations, very similar to the results of our vortex detection algorithms. Some of these applications include spatial distribution of trees [34, 35, 36], plants [37], bird nests [38] and the spread of disease [39].

One such measure of homogeneity is Ripley's K Function [40], defined theoretically in the following way,

$$K(s) = \lambda^{-1} E[\# \text{ of points within distance } s \text{ of a randomly chosen point}], \quad (3.4)$$

where λ is the density (number per unit area) of points. $K(s)$ can be analytically evaluated when it is known that points are distributed according to a homogeneous Poisson process, i.e. randomly placed in space. In this case each point is independent from all the other points and the resulting equation for $K(s)$ is known as complete spatial randomness (CSR),

$$K(s) = \pi s^2. \quad (3.5)$$

The simplest use of Ripley's K function is to approximate $K(s)$ from an observed set of points and test the result of CSR. Should the result be inconsistent with CSR, $K(s)$ can also tell us at what length scales the points deviate from spatial homogeneity.

For most of our simulations, $K(s)$ can be easily estimated by using observed vortex locations.

$$\hat{K}(s) = \frac{A}{N_v^2} \sum_i \sum_{j \neq i} I(d_{ij} < s), \quad (3.6)$$

where d_{ij} is the distance between the i th and j th vortex, A is the area of the region of interest, N_v is the number of vortices, and I is the indicator function (1 if its argument is true, 0 otherwise). In homogeneous simulations A could be as simple as the numerical box area, while with a trapped condensate calculating A could involve measuring the bulk part of the condensate or calculating an area using the TF radius.

Equation 3.6 ignores so called *edge effects*. These effects arise when the search radius s becomes large enough that the lack of points outside the region of interest begins to bias the estimator $\hat{K}(s)$. Ripley provides an edge-corrected estimator [41] which takes the form,

$$\hat{K}(s) = \frac{A}{N_v^2} \sum_i \sum_{j \neq i} w(\mathbf{r}_i, \mathbf{r}_j)^{-1} I(d_{ij} < s), \quad (3.7)$$

where the weight function, $w(\mathbf{r}_i, \mathbf{r}_j)$, provides edge correction. If the circle centred on the point \mathbf{r}_i and passing through the point \mathbf{r}_j completely lies within the region of interest, then $w(\mathbf{r}_i, \mathbf{r}_j) = 1$, otherwise $w(\mathbf{r}_i, \mathbf{r}_j)$ is equal to the proportion of the circumference of the circle that is inside the region of interest. The edge-corrected estimator provided by Equation 3.7 should be used when we are interested in large spatial scale homogeneity, i.e. when s is large, as it is on this scale edge-effects can dominate.

Visualising $\hat{K}(s)$ can be made easier by considering Ripley's L function, with estimator,

$$\hat{L}(s) = \sqrt{\frac{\hat{K}(s)}{\pi}}. \quad (3.8)$$

$L(s)$ has the useful properties that under CSR the variance is approximately constant [42], which can be used as a secondary check, and $L(s) - s$ should be approximately zero for all s . Deviations from zero allows us to immediately identify in what way, as well as at what scale, spatial homogeneity is broken in the dataset.

The power of Ripley's curves is demonstrated in Figure 3.7, wherein $K(s)$ and $L(s)$ were estimated (taking edge-effects into account) from inhomogeneous sample points. Inhomogeneity was enforced by randomly placing 100 sample points within the region $x, y \in (-5, 5)$, with two further randomly placed 'clusters' of 100 points in the regions $x, y \in (-5, -4)$ and $x, y \in (4, 5)$. The curve $\hat{L}(s) - s$ clearly shows a positive region (suggesting clustering) on the scale of the cluster size, and a negative region (suggesting dis-

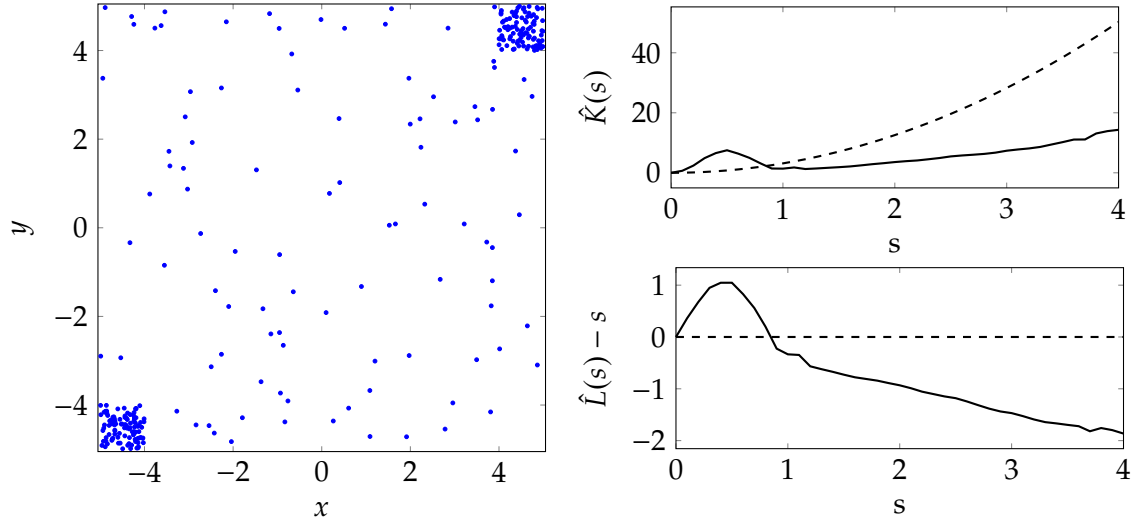


Figure 3.7: Sample points (left) used for estimating Ripley’s K and L functions. Shown (right) are the estimated curves $\hat{K}(s)$ and $\hat{L}(s) - s$ (black solid lines) and the theoretical curves (dashed black lines) for points under complete spatial randomness. Here Equation 3.7 was used to calculate $\hat{K}(s)$. $\hat{L}(s) - s > 0$ for small values of s and $\hat{L}(s) - s < 0$ for larger values of s , demonstrating that the sample points are clustered at small scales and sparse at larger scales.

persion) on the scale of the box size, detecting from the point data alone exactly the spatial pattern used to generate the points.

3.3.3 Recursive Cluster Algorithm

The limit of Ripley’s curves is quickly reached when we want to describe statistics of both the charge and spatial features of a collection of vortices. The K and L curves operate solely on location and are not easily modified to capture the charge of a vortex and so for detailed analysis of charged vortex clusters another algorithm must be used.

The algorithm we use is the Recursive Cluster Algorithm (RCA) developed by Reeves *et. al.* [43, 44]. The algorithm allows for detailed spatial-temporal statistics regarding like-signed vortex clustering. The algorithm works in a recursive manner, by removing dipole-like structures first, and then decomposing the remaining vortices into positive or negatively signed clusters. To perform the algorithm the following two rules are applied to a collection of vortices:

- *Opposite sign vortices that are mutual nearest-neighbors are removed from the algorithm’s consideration.*
- *Same-sign vortices that are closer to each other than either is to an opposite-sign vortex are placed in the same cluster.*

The rules are applied repeatedly in order until no more vortices can be added to the dipole

or cluster groups. Any remaining vortices are labelled as “free vortices”. An implementation of the algorithm, compatible with the output of the vortex detection algorithms in Section 3.2, is described in detail in Algorithm 7. A sample RCA decomposition of 200 randomly placed points with random polarity is demonstrated in Figure 3.8. It can be seen that the algorithm correctly picks out the chance clusters of like-signed points.

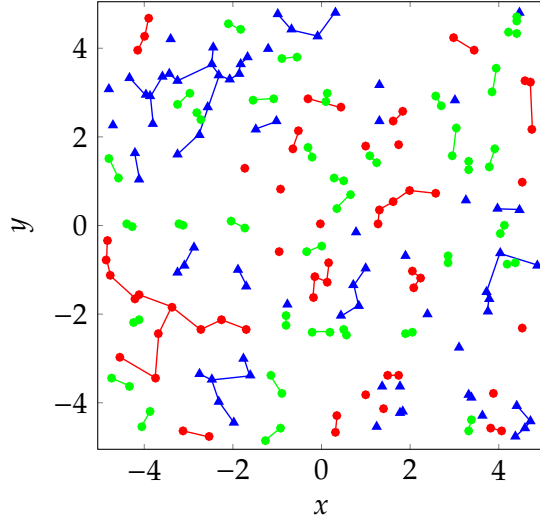


Figure 3.8: A sample RCA decomposition into clusters, free vortices and dipoles. Positive (negative) clusters and vortices are shown as blue triangles (red circles), dipoles are shown as green circles.

With the decomposed points, one can begin to obtain the statistical properties of the clusters. The physical location of the cluster can be estimated using its ‘center of mass’,

$$\mathbf{R}_C = \frac{1}{N_C} \sum_{i \in C} \mathbf{r}_i, \quad (3.9)$$

where C is the a set of vortices in a particular cluster, N_C is the number of vortices in the set C , and \mathbf{r}_i is the vortex location. Additionally, the size of a particular cluster can be quantified using an expression for the approximate cluster radius,

$$R_C = \frac{1}{N_C} \sum_{i \in C} |\mathbf{r}_i - \mathbf{R}_C|. \quad (3.10)$$

3.4 Building vortex trajectories

It is of interest to be able to track vortices over time, eventually leading to the building of vortex trajectories. The process of building trajectories from the location of many different points over time is known as particle linking. Note that in particle linking although the location of particles is known, their identity is unknown (that is, the particles are not la-

belled) and so it is not immediately obvious what particle at one point in time corresponds to another at different times and so methods for particle linking are therefore often built through minimisation algorithms.

The first step in the particle linking method described here is to perform frame-to-frame particle linking. Links are built by moving from one time point to the next and pairing vortices that are close together (taking into account both euclidean distance and vortex charge), as these are likely to be the same vortex. This step is performed efficiently using the Hungarian algorithm [45], an algorithm that is able to pairs together many particles at two different time points while minimising the sum of all the pair distances.

As the simulation develops, the number of vortices will change and so trajectories will necessary end early or begin at later times. A threshold value, Δ_v used in conjunction with the Hungarian algorithm controls if a track ends. If the euclidean distance between a pair of vortices exceeds Δ_v , it is assumed they cannot possibly be the same vortex, and they are not linked. The algorithm continues in fashion, linking pairs of vortices frame-to-frame until the end of the simulation is reached.

Sometimes, due to numerical error or simulation dynamics, a vortex will not be detected for one or more time points before reappearing. The particle linking algorithm must take this into account, aiming to assign each vortex only a single trajectory. The second step in the method is to iterate once more through the data and investigate the ends of the trajectories. If a trajectory beginning is found close (once again taking into account euclidean distance and vortex charge) to the end of a previous trajectory within a certain number of time points, a link is made joining the two trajectories. Once again a threshold value compared to the distance between points in space and time. Should the trajectory ends be too far apart, it is assumed they are not the same vortex and remain unlinked. Figure 3.9 demonstrates the building of vortex trajectories in a trapped condensate.

3.5 Removing vortices with phase unwinding

A problem with long-time numerical simulations is the effects of the finite boundaries on the results. In some cases large boxes or periodic boundary conditions are an adequate way of avoiding spurious results introduced by boundary effects. However, in some cases, vortices “wrapping around” the numerical domain is unfavourable as they may interfere with regions of interest and increasing the numerical grid can be infeasible due to computational constraints.

A particularly problematic example of this kind of situation is encountered often in the latter sections of this thesis: a simulation working in the moving frame with vortices nucleated via a potential obstacle. This system is of particular note because vortices that have fallen downstream wrap around the domain and re-approach the potential obstacle,

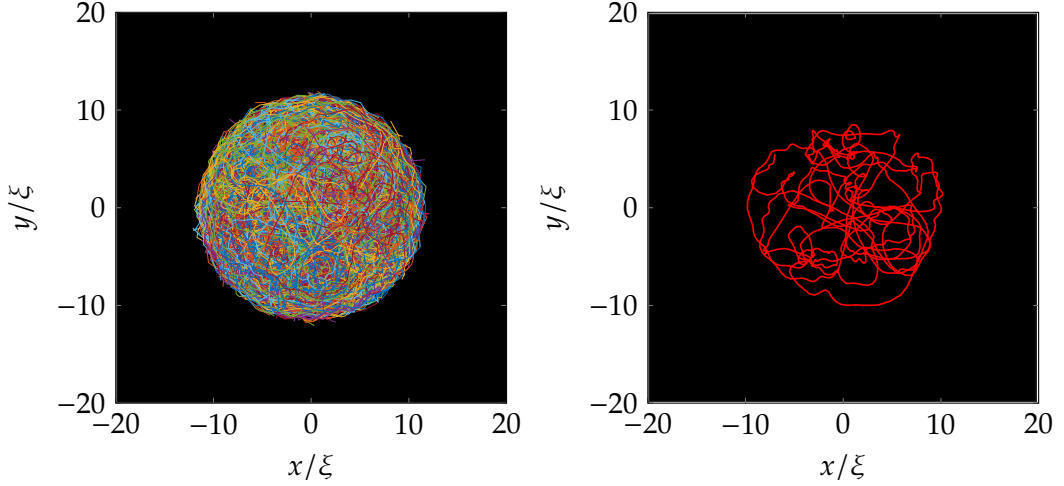


Figure 3.9: An example of building vortex trajectories for a trapped condensate with interaction energy $\hat{g} = 2000$ and $\hat{\mu} = 25.27$ filled with vortices of both polarity. (Left) 353 vortex trajectories clearly showing the movement of vortices within the boundary of the condensate. (Right) The single longest vortex trajectory, over the time period $648.5 \omega^{-1}$.

modifying the nucleation dynamics and the drag force felt by the obstacle.

The ideal solution would be to implement so called *absorbing* boundary conditions. These boundaries allow waves and vortices to pass by, without any reflections, as if they had travelled through the boundary to infinity. An approximation for absorbing boundary conditions in a homogeneous GPE has been used to study flows patterns behind an obstacle [46]. Thin fringe areas are added near the outer edges of the numerical domain. A small dissipation $\gamma \approx 0.1$ is applied in this region, ramping up smoothly from $\gamma = 0$ in the bulk to its maximal value in the fringe area. Inside the fringe region, waves and vortex pairs lose energy; the amplitude of waves decay and opposite-signed vortices move towards one-another so as to annihilate.

To facilitate the process and allow the fringe region to remain as small as possible, vortices in the region are “unwound” using Algorithm 8. In practice this is performed by simply imprinting a vortex of opposite charge directly at a vortex’s location (and so accurate vortex detection methods as described in Section 3.2 are required). A demonstration of the vortex unwinding process is shown in Figure 3.10. The vortex located at $(-5\xi, -5\xi)$ is unwound and so its phase singularity is removed. Note that around the outer side of the domain the phase winds by 8π before the process, and only by 6π after, indicating a vortex has indeed been removed.

Also demonstrated in Figure 3.10 is the result of an additional routine. At the same time as unwinding the phase, the density profile of the vortex core is replaced with the value of the density at infinity. This reduces a vortex core (which then must decay as the

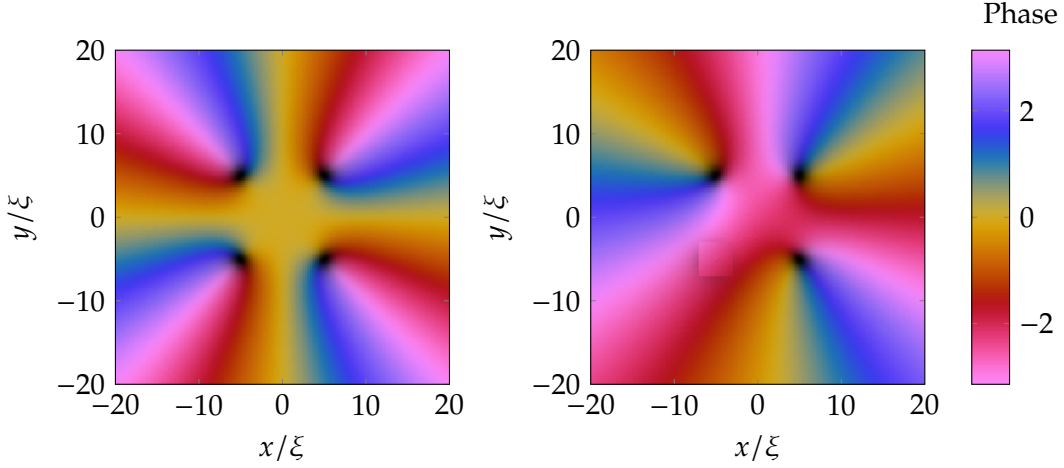


Figure 3.10: An example of the unwinding of a vortex. (Left) A homogeneous condensate containing 4 positively charged vortices located at $(\pm 5\xi, \pm 5\xi)$. (Right) The vortex at $(-5\xi, -5\xi)$ has been removed using Algorithm 8.

singularity is removed) into a collection of smaller waves, which decay much quicker.

The final result of these routines is that fluid wrapping around the numerical domain is clean (free of any vortices and waves), and the resulting in-flowing fluid does not affect any part of the simulation. This allows for simulations to be run for much longer in time, allowing for better measurement of quantities such as drag force or nucleation frequency.

3.6 Quasi-Condensate Visualisation

When simulating a finite temperature Bose gas, the raw numerical wavefunction is too noisy to allow direct visualization of vortical structures. This can be overcome by defining a quasi-condensate wavefunction $\hat{\psi}$, as established in [14]. This wavefunction is constructed by filtering out high-frequency spatial modes from the classical field wavefunction, by transforming the complex amplitudes via $\hat{a}_k = a_k \times \max\{1 - k^2/k_c^2, 0\}$. $\hat{\psi}$ then represents the long-wavelength component of the classical field.

The choice of k_c is facilitated by the bimodal distribution of occupation numbers in the wavefunction, a distribution which develops naturally through propagation of the GPE. The high- k part of the distribution is associated with the thermal excitations and low mode occupations. The low- k part of the field is the quasi-condensate, characterised by macroscopic mode populations and superfluid ordering. k_c is chosen as the boundary in k -space between the quasi-condensate and the thermal gas. Figure 3.11 demonstrates the filtering technique in action.

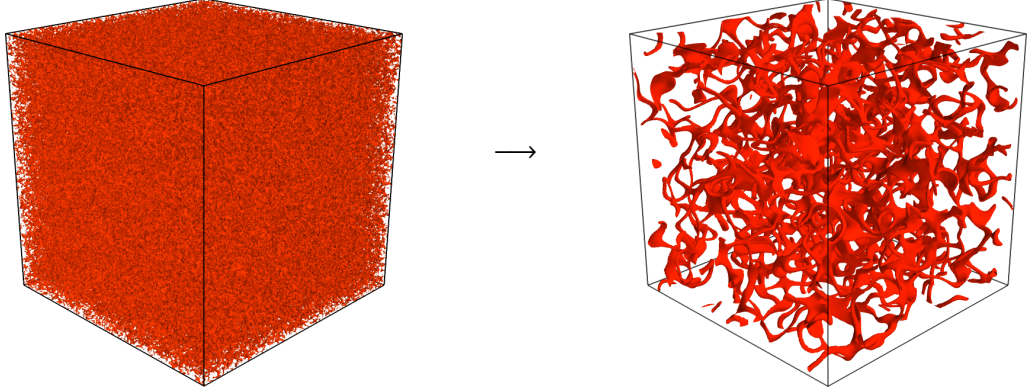


Figure 3.11: (Left) Unfiltered wavefunction density, $|\psi|^2$, from a classical-field simulation with condensate fraction $\rho_0/\rho = 0.22$ during equilibration. A vortex tangle is present but not visible by direct density visualisation. (Right) Filtered wavefunction density, $|\hat{\psi}|^2$, clearly showing the vortical structures in the gas.

3.7 Evaluation of vortex line-length in 3D

For a given 3D wavefunction, Ψ , featuring a vortex distribution, the vortex volume V_t (the total volume associated with the vortex cores) is evaluated by numerical integration of the inside of the vortex isosurface tubes obtained from the filtered density $|\hat{\Psi}|^2$, with an integration region of the whole numerical box. Note that the isosurface level should be low enough to pick out vortex cores only (and not, e.g. fluctuations and waves), while large enough to contain sufficient grid points to allow a reasonable numerical evaluation of volume. In this work we use the isosurface level $0.04\langle|\hat{\Psi}|^2\rangle$ (chosen so as to produce filtered vortex cores that are similar in radius to the true vortex core). The volume calculation can be written $V_t = \int \Theta(0.04\langle|\hat{\Psi}|^2\rangle - |\hat{\Psi}(\mathbf{r})|^2) dV$, where Θ is the Heaviside step function. In practice the calculation of the vortex core volume can be efficiently performed by assigning a value of unity/zero to grid points located within/outside the isosurface tubes and directly integrating the result using the trapezium or Simpson's rule.

The total line length is then deduced by dividing V_t by the cross-sectional area of a vortex core, A_t (in effect, the average cross-sectional area of the isosurface tubes). The measured values of V_t and A_t will depend on the chosen isosurface level but, providing the vortex tubes are well-separated, their ratio (and hence the evaluated line length) will remain constant. For closely-positioned vortex tubes, the isosurface level can affect whether the tubes appear as two separate tubes, or start to merge, and so will lead to deviations in this ratio.

Part II

Numerical Studies

Chapter 4

Classical-like wakes behind elliptical obstacles in Bose-Einstein condensates

4.1 Introduction

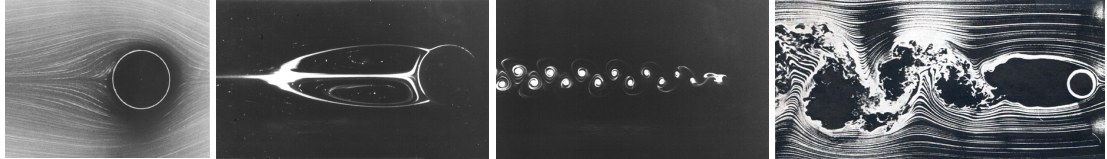


Figure 4.1: Classical viscous flow past a cylinder. From left to right: laminar flow ($Re = 3.64$) [47]; steady symmetric wake behind the cylinder ($Re = 41$) [47]; time-dependent Bénard–von Kármán vortex street ($Re = 112$) [48]; and chaotic downstream wake ($Re > 10^5$) [49].

Recent experimental [50, 51], numerical [52, 53, 54] and theoretical studies [55] have highlighted similarities between turbulence in quantum fluids and turbulence in ordinary (classical) fluids [56]. In particular, it is found that, in the idealized case of homogeneous isotropic conditions away from boundaries, the distribution of kinetic energy over the length scales obeys the celebrated Kolmogorov scaling of classical turbulence [57]. This similarity is remarkable, because a superfluid has zero viscosity and vorticity is not a continuous field but is concentrated in discrete vortex filaments of fixed circulation κ proportional to Planck's constant. In the more realistic presence of boundaries (such as an obstacle or confining channel walls), superfluid hydrodynamics is less understood, despite the large number of experiments in such scenarios.

In a classical viscous fluid [56], the prototype problem with a boundary is the flow around a cylinder or a sphere (or, changing the frame of reference, the motion of a cylinder

or a sphere in a fluid at rest). The nature of such flow is determined by the Reynolds number $Re = vd/\nu$, where v is the (assumed uniform) flow's velocity away from the obstacle, d is the obstacle's size, and ν is the fluid's kinematic viscosity. If $Re \lesssim 50$, a steady symmetric wake forms behind the obstacle; if $10^2 \lesssim Re \lesssim 10^5$ the wake becomes asymmetric and time dependent, forming the famous Bénard–von Kármán vortex street structure. These cases are depicted in Figure 4.1. At even higher Re , the flow becomes turbulent.

What happens in a superfluid is not clear. Firstly, the superfluid has zero viscosity ($\nu = 0$) and hence Re cannot be defined. Secondly, experiments performed in superfluid helium confirm that the flow is affected by the boundaries [58, 59]; unfortunately what is observed is not the flow pattern itself, but rather the trajectories of tracer particles, whose relation with the flow is still the subject of investigations [60]. Numerical simulations of three-dimensional (3D) superfluid flow around an oscillating sphere performed using the vortex filament model were not conclusive - quantum vortices did not appear to organise themselves into a visible classical-like wake near the obstacle [61, 62, 30].

The two-dimensional (2D) scenario of an obstacle moving through a superfluid offers a simplified platform to consolidate analogues and disparities between classical and quantum fluids. In their pioneering simulations of the 2D nonlinear Schrödinger equation, Frisch and Pomeau [63] observed the formation of vortex pairs in the flow past a circular obstacle. A more complete picture has been recently revealed by Sasaki *et al.* [64]. Below a critical velocity (which depends on the strength [65] and shape of the external potential), the fluid undergoes laminar flow around the obstacle. Above this critical velocity vortices become nucleated and peel off from the moving obstacle. Two patterns are possible, depending on the size of the obstacle: vortex-antivortex pairs in either a symmetric [63] or asymmetric configuration (with the preference for the latter); or alternating pairs of like-signed vortices, forming a trail analogous to the Bernárd-von Kármán vortex street. At higher velocities, vortex nucleation becomes highly irregular. Recent studies of this 2D system have considered vortex emission and drag [66, 67, 68, 69], the critical velocity [70, 71, 72, 73, 74], the effect of inhomogeneous potentials [68, 75, 76], the role on the obstacle parameters [69, 77], and supersonic effects such as oblique dark solitons [78] and Cerenkov radiation [79].

In this chapter we present the first clear evidence of a classical-like wake in superfluid flow past an obstacle. Using the 2D Gross-Pitaevskii equation (GPE) for a zero-temperature Bose-Einstein condensate and an elliptical obstacle, we show that the interaction of discrete vortex singularities downstream of the obstacle yields a flow pattern which mimics classical vortex flow.

4.2 Model

We consider an atomic Bose-Einstein condensate (BEC) moving relative to a laser-induced obstacle (imposed through an external potential), as realized experimentally in 3D [80, 81, 82, 83] and quasi-2D condensates [83]. This scenario closely resembles that of the classical wake-problem [47, 48]. On a much larger scale, a similar 3D configuration has been experimentally realized in liquid helium [58, 59].

The BEC, assumed to be weakly-interacting and at ultracold temperature, is modelled through the GPE described in Section 2.3.1 transformed into the moving frame as shown in Section 2.10.1. The external potential acting on the system $V(\mathbf{r}, t)$ is taken to be zero everywhere, apart from a localized repulsive potential which represents the obstacle with a Gaussian shape described in Section 2.15.2. A key feature of this work is that the obstacle is taken to be elliptical, of ellipticity ϵ , with the short axis being parallel to the flow, x . Such a potential can be generated via the repulsive optical dipole force from an incident blue-detuned laser beam which is moved relative to the condensate either by deflection of the beam [80, 81, 82] or motion of the condensate itself when offset in a harmonic trap [83]. While laser-induced obstacles generated to date have had a circular profile, elliptical modification of the Gaussian potential can be achieved via cylindrical focussing of the laser beam.

4.3 Two-Dimensional Wakes

4.3.1 Vortex emission from elliptical obstacles

For illustrative purposes we first consider an elliptical obstacle (size $d = 5\xi$, ellipticity $\epsilon = 3$) moving at speed $v = 0.365c$. This speed exceeds the critical velocity for the obstacle such that quantum vortices become nucleated and trail behind to form a wake [Figure 4.2(a)]. Sound waves, also generated by the obstacle, have little effect on the vortex dynamics. At early times [Figure 4.2(a)(i)], the vortex shedding occurs through the symmetric generation of vortex-antivortex pairs, leading to a collimated and symmetric wake behind the obstacle. This is in qualitative agreement with observations for circular obstacles [63, 66, 68, 69], although, for the same obstacle velocity and size, the elliptical obstacle induces a higher frequency of vortex emission and thus a denser wake. We examine the role of ellipticity in more detail in Sections 4.3.3 and 4.3.4.

At later times [Figure 4.2(a)(ii)], the flow becomes asymmetric due to the known instability of symmetric wakes [66]. A striking pattern emerges whereby distinct clusters of co-rotating vortices (of the order of 5 vortices in each cluster) develop downstream of the obstacle. Each cluster contains vortices of the same sign and adjacent clusters have alternating sign. These clusters form a Bénard–von Kármán vortex street downstream

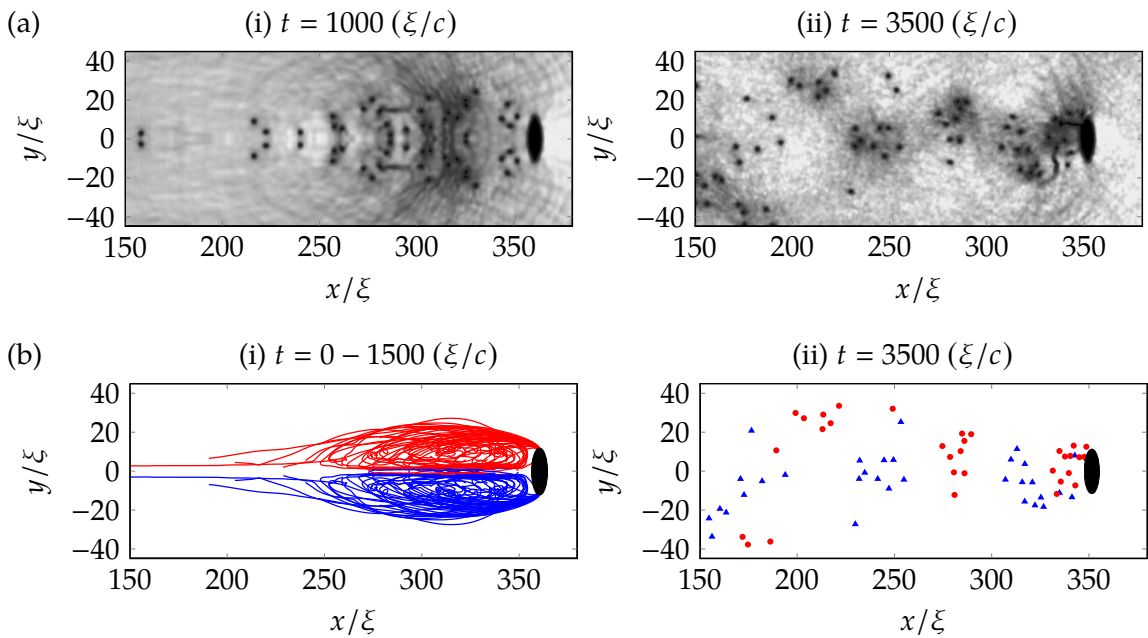


Figure 4.2: Snapshots showing the (a) density profile and (b) vortex trajectories during vortex shedding from an elliptical object ($\varepsilon = 3$) at (i) early times and (ii) later times. The obstacle has speed $v = 0.52c$ and size $d = 5\xi$. Red and blue lines represent vortices of oppositely quantized circulation. At early t , a symmetric wake similar to a classical fluid with low Re forms. Symmetry breaks at $t \approx 1500 (\xi/c)$ at which point vortex motion becomes disordered. In this case the initial condition is noise-free.

from the obstacle, confirming the intuition that a sufficiently large number of quanta of circulation reproduce classical physics. Here, the ellipticity of the obstacle facilitates the formation of this street; the relatively high rate of vortex emission leads to a greater interaction between vortices in the wake which in turn promotes clustering. In contrast, for a circular obstacle the symmetric wake evolves into a V-shaped wake of vortex-antivortex pairs [64]; this because the vortex emission rate and hence their subsequent interaction is insufficient to induce significant clustering.

The vortex trajectories provide visualisation of the time-integrated nature of the wake [Figure 4.2(b)]. At early times (i), we see that the vortex trajectories are symmetric, forming a flow pattern in striking analog to the classical wake at low Re . The generic development of vortex trajectories is as follows. Pairs of singly-quantized vortices of opposite sign peel off from the poles of the obstacle and interact with each other as vortex-antivortex pairs. Each pair propagates in the positive x direction with approximate velocity $\hbar/(md_p)$ [64], where d_p is the pair separation [84]; the pair's velocity is less than the obstacle's velocity and it drifts behind the obstacle. As the pair moves further away from the obstacle, its separation decreases and its velocity increases, such that it begins to catch the obstacle up. Once the pair is sufficiently close to the obstacle, it again separates and slows down, then the cycle repeats. As more vortices are nucleated, two distinct clusters of like-circulation form. Nucleated pairs then travel around the outside of the existing cluster before contracting, speeding up and travelling through the middle of the clusters towards the obstacle. The clusters grow until they reach a maximum size depending on the obstacle's size and speed. Hereafter, nucleated vortex pairs travel around the outside of the two clusters and continue travelling downstream, becoming lost from the main wake.

4.3.2 Formation of the Bénard–von Kármán vortex street

Once the symmetry of the wake is broken, vortices no longer separate into two distinct clusters of like-circulation. Existing vortices and newly-nucleated vortices mix together behind the obstacle. However it is apparent in Figure 4.2(b)(ii) that, on average, positive vortices drift to $y > 0$ while negative vortices prefer to drift to $y < 0$.

To accelerate the formation of the asymmetric wake, we subsequently seed the initial condition with noise. Figure 4.3 shows the vortex locations at various stages of the evolution. The initial symmetry of the wake [Figure 4.3(a)] breaks at $t \approx 450(\xi/c)$, with the wake splitting into several clusters. The velocity field around the obstacle is affected: it depends on time and the distance of the nearest cluster of vortices. The obstacle no longer simultaneously produces vortex-antivortex pairs, but now generates a series of like-signed vortices. Since like-signed vortices are known to co-rotate, these vortices group into clusters which slowly rotate. This cluster effects the velocity field once more, causing a cluster of opposite signed vortices to be produced. This process then repeats such that clusters

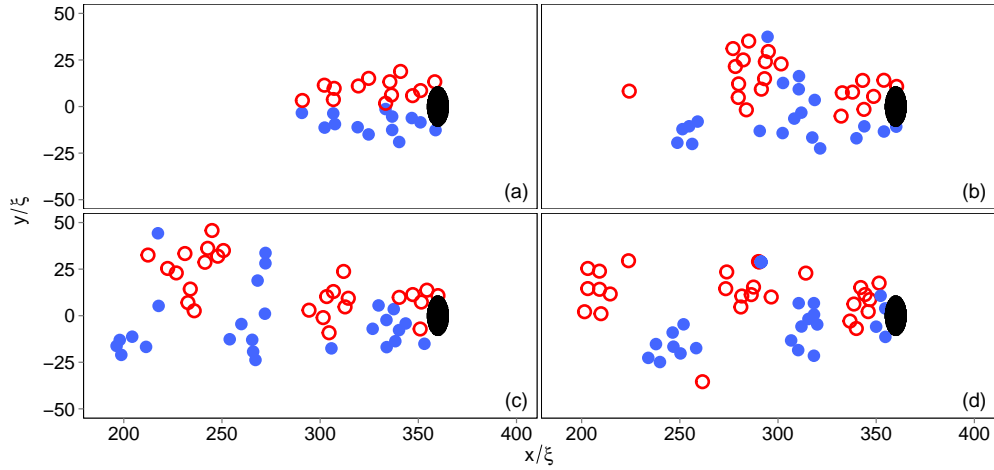


Figure 4.3: Snapshots of vortex locations during the motion of an elliptical object ($d = 5\xi$ and $\varepsilon = 3$) at speed $v = 0.52c$ in the presence of small-amplitude noise at $t = 0$. The snapshots are at times (a) $t = 450$, (b) 900 , (c) 1000 and (d) 1100 (ξ/c). Red/blue circles represent vortices with quanta of circulation $+1/-1$. The wake forms into clusters of like-circulation that continue to be produced, in analogy to the classical Bénard–von Kármán vortex street from a cylinder.

of like signed vortices are then produced behind the obstacle, much like vorticity in the classical vortex street behind a cylinder. While some positive clusters contain negative vortices and vice versa, the overall pattern is still a time-dependent Bénard–von Kármán vortex street.

For clusters consisting of pairs of vortices, it has been shown that they can survive downstream for a very long time [64]. However, for regimes with larger numbers of vortices in each cluster, the chaotic nature of vortex motion can cause originally tightly packed and circular clusters to easily stretch over large areas, form strange shapes, or even split into smaller clusters. Examples of this will be shown later in Figure 4.5.

4.3.3 Critical Velocity past an Elliptical Obstacle

Elliptical obstacles facilitate the formation of semi-classical wakes because they reduce the critical velocity and enhance the vortex shedding frequency. Figure 4.4(a) shows the critical velocity for flow past the obstacle as a function of its ellipticity, taking the obstacle to have fixed width in the y -direction of $d = 10\xi$. We determine the critical velocity numerically by performing simulations with flow velocities increasing in steps of 0.01 until vortices nucleate. For a circular object, we find that the critical velocity is $v_c = 0.355(\pm 0.005)c$, consistent with predictions in the Eulerian ($d \gg \xi$) limit [72, 73, 74]. As the ellipticity is increased (i.e. the obstacle becomes narrower in x), the critical velocity decreases. The modification of the critical velocity is significant: if $\varepsilon = 3$, v_c is more than 40% smaller than that for a circular obstacle.

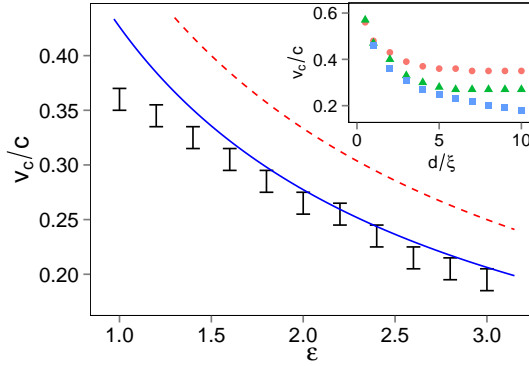


Figure 4.4: Critical velocity against obstacle ellipticity ε , for $d = 10\xi$. Shown are the results from the numerical simulations (black bars), Equation (4.1) (dashed red line) and Equation (4.2) (solid blue line). Inset: Critical velocity (obtained numerically) versus the obstacle width d , for ellipticities $\varepsilon = 1$ (red circles), $\varepsilon = 2$ (green triangles) and $\varepsilon = 3$ (blue squares).

The rough dependence of v_c on ε can be derived as follows. According to Landau's criterion [85], superfluidity breaks down when the fluid velocity exceeds the critical velocity $v_{\text{Lan}} = \min[E(p)/p]$, where p is the momentum of elementary excitations and $E(p)$ their energy. The weakly-interacting Bose gas has the dispersion relation $E(p) = [n g p^2/m + p^4/(4m^2)]^{1/2}$, hence $v_{\text{Lan}} = c$. If an obstacle moves through the fluid with speed v , the local fluid velocity at the poles exceeds v . Approximating the BEC as an inviscid Euler fluid undergoing potential flow about the object, then the maximum local velocity is $v_{\max} = (1 + \varepsilon)v$ and the Landau critical velocity is (dashed red line in Figure 4.4(a)),

$$\frac{v_{c1}}{c} = \frac{1}{1 + \varepsilon}. \quad (4.1)$$

While this result assumes constant density, a first order correction can be made by using Bernoulli's theorem to model the reduction in local density near the obstacle (due to the enhanced local fluid velocity) which in turn reduces the local speed of sound $c(x, y) = \sqrt{n(x, y)g/m}$ [86]. This then leads to the modified result,

$$\frac{v_{c2}}{c} = \left[\frac{3}{2}(1 + \varepsilon)^2 - \frac{1}{2} \right]^{-\frac{1}{2}}. \quad (4.2)$$

This relation (solid blue line in Figure 4.4) gives good agreement with the computed values of v_c . The deviation for $\varepsilon \sim 1$ has been noted elsewhere [73], and can be remedied using higher order corrections.

From studies on circular objects, it is known that v_c depends on the obstacle's shape at small diameters, where boundary layer effects are significant; v_c approaches the "Eulerian" value only for large diameters $d \gg \xi$ [69, 73]. The variation of v_c with the obstacle width d is shown in Figure 4.4 (inset). For $d = 10\xi$, the critical velocity effectively reaches its

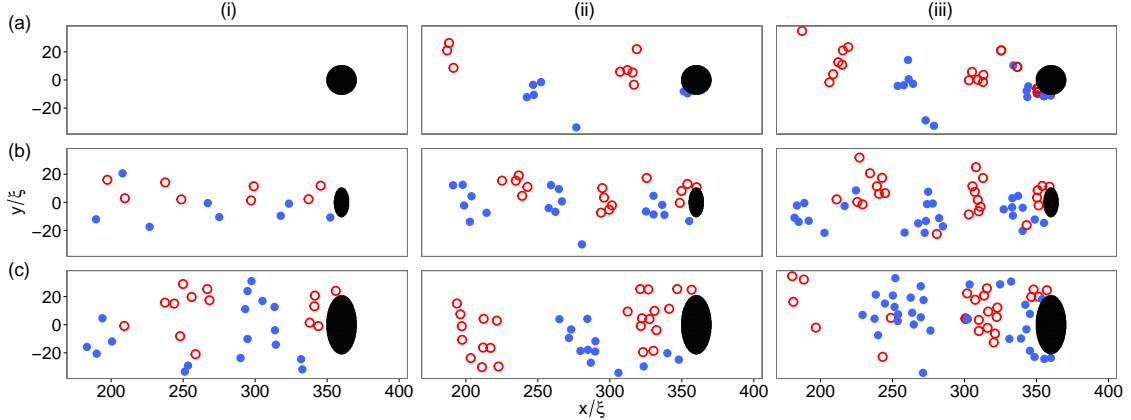


Figure 4.5: Snapshots of the vortex positions for various obstacle parameters, at $t = 2000$ (ξ/c). Shown are obstacles corresponding to (a) $\varepsilon = 1$ and $d = 5\xi$, (b) $\varepsilon = 2$ and $d = 5\xi$, and (c) $\varepsilon = 2$ and $d = 10\xi$, at the velocities (i) $v = 0.32c$, (ii) $v = 0.40c$, and (iii) $v = 0.48c$. Red/blue circles represent vortices with quanta of circulation $+1/-1$.

asymptotic value, while at smaller widths, it is much larger.

4.3.4 Role of Obstacle Size and Ellipticity on the Wake

During the initial symmetric phase of vortex nucleation, the wakes generated by the obstacle have the same qualitative structure shown in Figure 4.2(b) (i). However, once the wake becomes asymmetric, the nature of the clusters that form are highly dependent on the velocity and shape of the obstacle. Figure 4.5 shows wakes generated for various obstacle parameters, all captured at the same time $t = 2000$ (ξ/c). We find that any increase of size, ellipticity or velocity of the obstacle increases the number of vortices in the wake's clusters.

The shedding frequency of vortices increases with the velocity of the flow [67]. For an elliptical obstacle, the combination of a reduced critical velocity and increased local velocity around the obstacle has the effect of increasing the shedding frequency with ε and d . The overall result is that, when increasing any of v , ε or d , more vortices are nucleated in a given time period, causing the cluster size to increase. This increase in cluster size is investigated in the next section.

4.3.5 Vortex Clustering

We have shown that the Bénard–von Kármán vortex street forms through the clustering of like-signed vortices. Methods of quantifying the clustering of vortices in quantum fluids have been explored in the literature [87, 43, 88]. Here we utilize the algorithm of Reeves *et. al.* [43] to identify clusters.

Firstly we record the number of clusters N_c and the number of vortices in each cluster N_i , where i is the cluster index. Then we determine the average number of vortices in

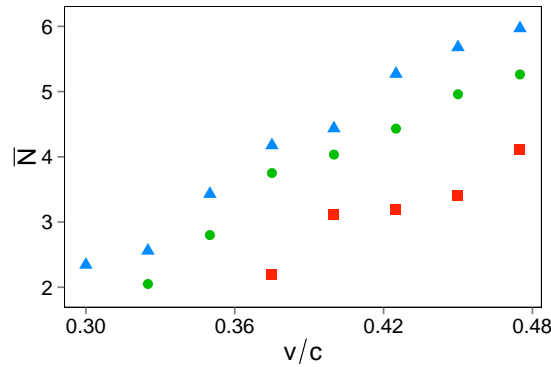


Figure 4.6: Average number of vortices in the clusters as a function of the obstacle velocity v . Shown are cases with $\varepsilon = 1$ (red squares), $\varepsilon = 2$ (green circles) and $\varepsilon = 3$ (blue triangles). All cases feature $d = 5\xi$.

the clusters, $\bar{N} = (1/N_c) \sum_{i=1}^{i=N_c} N_i$ as a function of obstacle velocity v for three ellipticities $\varepsilon = 1, 2$ and 3 , at times $t = 500(\xi/c), 510(\xi/c), \dots, 2500(\xi/c)$. The results, plotted in Figure 4.6, show that increasing v (above the critical velocity) causes \bar{N} to increase and that, at fixed v , \bar{N} increases with ε . We attribute this to an object with a larger ε having a lower critical velocity and producing more vortices at the same v . This result explains why an elliptical obstacle efficiently generates a semi-classical wake composed of large vortex clusters. We also find that for all values of ε , a large obstacle velocity ($v \gtrsim 0.6$) causes vortices to nucleate non-periodically, inducing an irregular flow without a visible Bénard-von Kármán vortex street configuration, in agreement with previous simulations with circular obstacles of smaller diameter [64].

4.4 Results: Three-Dimensional Wakes

We now generalize our results to 3D by considering quantum wakes in three-dimensional flow past a localized obstacle, as simulated via the 3D GPE with the 3D obstacle potential of Equation (2.42). Our results will confirm that the features observed in 2D wakes also arise in the 3D setting. A comprehensive study of the parameter space is, however, not tractable in 3D due to the computational intensity of the 3D simulations.

4.4.1 Symmetric Wakes

For a spherical ($\varepsilon = 1$) object with $d = 5\xi$, we find that the critical velocity is $v_c = 0.455 \pm 0.05c$, consistent with $v_c = 0.55c$ reported in the Eulerian limit ($d \gg \xi$) [86, 89]. Making the obstacle ellipsoidal, with the short direction parallel to the flow, reduces the critical velocity, in parallel with our 2D observations. For example, for $\varepsilon = 5$, the critical velocity is reduced to $v_c = 0.315 \pm 0.05c$. Figure 4.7(a) shows the 3D wake generated past this

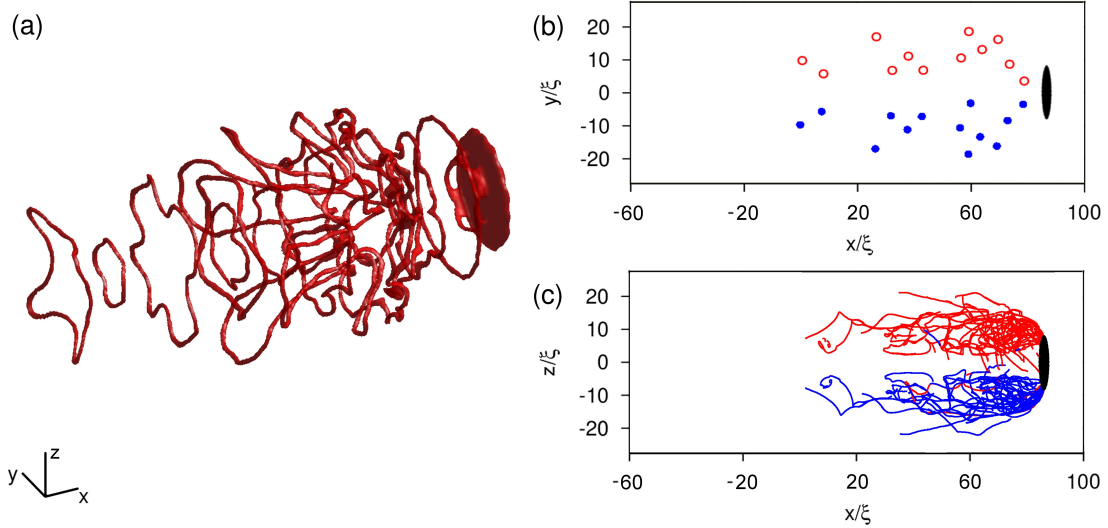


Figure 4.7: Symmetric wake in 3D at $t = 450 (\xi/c)$ for an elliptical obstacle ($d = 5\xi$ and $\epsilon = 5$) moving at $v = 0.6c$. (a) Isosurface plot of low density, over a range $[0, 100]$ in x and $[-25, 25]$ in y and z . (b) Vortex locations in the xy plane. (c) Vortex trajectories in the xz plane. Here (b) and (c) show opposing circulation in red and blue.

ellipsoidal obstacle ($d = 5\xi$ and $\epsilon = 5$) when moving at super-critical speed $v = 0.6c$. Vortex rings, the 3D analog of vortex-antivortex pairs, are ejected at high frequency (due to the obstacles high ellipticity) in the direction of the flow. At early times ($t = 450 (\xi/c)$ in this case) the vortex configuration maintains cylindrical symmetry about the obstacle's axis, as is clearly visible in the xy and xz planes in Figure 4.7(b) and (c). As the vortex rings move downstream they shrink and speed up, returning to the object, sometimes passing through other vortex rings. A similar behaviour is observed [90] in the evolution of toroidal bundles of many coaxial vortex rings which leapfrog around each other. Occasionally a ring will escape this cycle and fall downstream. These behaviors conspire to form an organized symmetric wake behind the obstacle, the 3D analog of our 2D observations.

4.4.2 Asymmetric Wakes

We break the cylindrical symmetry of the system by tilting the obstacle by a small angle in the xz plane. The vortex rings, illustrated in Figure 4.8, now become ejected and evolve asymmetrically; Kelvin waves and reconnections occur, forming an apparently disordered tangle of vortices behind the obstacle. Due to the manner in which symmetry is broken, the wake remains approximately symmetric in the xy plane, as evident in Figure 4.8 (b). However, unlike in Figure 4.8, the vortices do not self organise into two clusters of alternate circulation. This is due to the vortex rings interacting, reconnecting and shifting out of the plane (which manifests in 2D as two alternate-sign vortices approaching one another).

However, in the xz plane (Figure 4.8 (c)), symmetry is broken. Due to the relatively

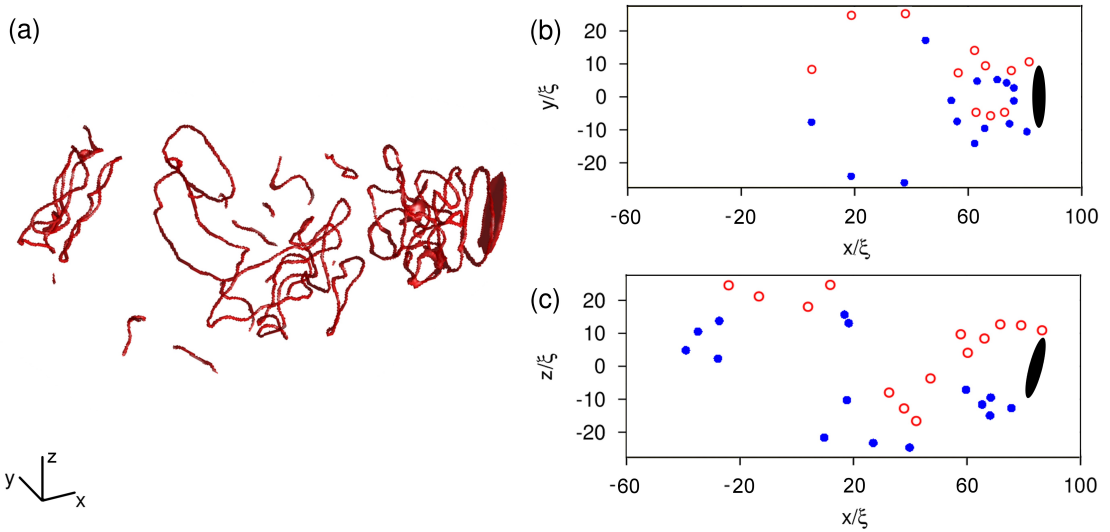


Figure 4.8: Asymmetric wake in 3D at $t = 340$ (ξ/c) for an elliptical obstacle ($d = 5\xi$ and $\epsilon = 5$) moving at $v = 0.6c$. (a) Isosurface plot of low density, over a range $[-60, 100]$ in x and $[-25, 25]$ in y and z . (b) Vortex locations in the xy plane. (c) Vortex locations in the xz plane. Here (b) and (c) show opposing circulation in red and blue.

high frequency of vortex nucleation and relatively low flow speed, like signed vortices cluster together as they are ejected by the obstacle, much like the 2D solutions seen in earlier sections. Downstream the tangle may shift both across or out of the plane. In 2D, although this manifests as a shift in location of the vortex clusters, the clusters largely remain rather than forming dipoles.

4.5 Conclusion

We have shown that the motion of an obstacle in a Bose-Einstein condensate produces classical-like wakes consisting of quantum vortices of the same polarity. This is consistently observed in both two- and three-dimensional scenarios. The key ingredient to produce classical-like wakes - that vortices are generated at a sufficiently high rate that they undergo strong interactions with their neighbours (rather than being swept away) - is that the obstacle is elliptical, which reduces the critical velocity for vortex nucleation. Symmetric wakes resemble those observed in classical flow at low Re . These are unstable, forming time-dependent asymmetric structures similar to the Bénard–von Kármán vortex street of classical fluid dynamics. Vortex singularities in the inviscid superfluid thus mimic classical vortex patterns typical of viscous flows. The effects which we describe (dependence of the critical velocity and cluster size on the obstacle's size, velocity and ellipticity) can be experimentally studied in atomic Bose-Einstein condensates using moving laser-induced potentials. They are also relevant to the motion of objects (such as vibrating wires, grids

and forks) in superfluid helium, as the obstacle's ellipticity plays a role which is analogous to rough boundaries [91, 27].

4.6 Model of 2D and 3D BEC with Gaussian Potentials

The 3D (2D) system is simulated using the 4th-order Runge-Kutta method under periodic boundary conditions on a $400 \times 150 \times 150$ (2048×512) grid with uniform spacing $\Delta = 0.4\xi$. The obstacle is positioned upstream in the box to enable a long simulation time before vortices recycle through the periodic box. We have verified that our simulations are well-converged, that is, increasing the grid resolution has negligible effect on the results. The computational box is sufficiently large that the boundary conditions do not play a role in vortex shedding. The initial condition is the stationary state of the GPE (including obstacle potential) with $v = 0$ (as determined by the imaginary time convergence method). Setting $V_0 = 100 \mu$ throughout, the external potential closely approximates an impenetrable obstacle. Unless stated otherwise, a small amount of noise is added to the initial condition to break symmetry: a random number between -0.0005 and 0.0005 is added to both the real and imaginary parts of the initial wavefunction.

To minimize initial generation of waves, v is ramped up in time along a hyperbolic tangent curve, from $v = 0$ at $t = 0$ to its terminal value at around $t \approx 100$ (ξ/c). During the evolution, the vortices are located (and their circulation evaluated) using an algorithm based on those of references [92] and [87].

Chapter 5

Decay of 2D quantum turbulence in a highly oblate Bose-Einstein condensate

5.1 Introduction

Ultracold gaseous Bose-Einstein condensates (BECs) provide a unique testbed with which to investigate the phenomenon of quantum turbulence and the more rudimentary realm of superfluid vortex dynamics [93, 94]. These systems provide an impressive degree of parameter manipulation unavailable in superfluid helium, the traditional context for studying quantum turbulence [95], with scope to control the particle interactions and potential landscape in both time and space. The typical size of these systems is only one or two orders of magnitude larger than the inter-vortex spacing, which in turn is another order of magnitude larger than the vortex core size. These compact length scales mean that the collective behaviour of vortices and their interaction with the background condensate is significant. The emergence of turbulent-like behaviour in the form of a vortex tangle was observed by Henn *et al.* in 2009 by oscillating a three-dimensional condensate [96]. What's more, the experimentalist's handle over the confining potential enables crossover to two-dimensional quantum turbulence [97]: by tightly confining the trap geometry along one axis, such that the vortices closely embody point vortices [98], states of two-dimensional quantum turbulence have been recently reported [99, 100].

In the recent experiment of Kwon *et al.* [100], a trapped, oblate BEC was translated past a stationary, laser-induced obstacle. As is characteristic of superfluids, vortices and anti-vortices were nucleated into the condensate once the relative speed exceeded a critical value [63]. A state of two-dimensional quantum turbulence emerged, characterized by a disordered distribution of vortices. The authors monitored the number of vortices, reveal-

ing the dependence on the relative speed and the thermal relaxation of the vortices. They directly observed vortex collision events, characterized by a crescent-shaped depletion in the condensate density. Furthermore, some vortex cores were seen to coalesce, evidence of vortex pair annihilation.

In this article we elucidate these experimental findings through mean-field simulations of the two-dimensional (2D) Gross-Pitaevskii equation (GPE), both at zero-temperature and in the presence of thermal dissipation, modelled through a phenomenological dissipation term in the GPE. Notably, our simulations provide insight into the sign of the circulation of the vortices and the early-stage evolution, not accessible experimentally. We establish the key stages of the dynamics, from the initial nucleation of vortices and formation of a quasi-classical wake, through the rapid symmetry breaking and disorganization of the vortices, to the decay of the vortices by annihilation or passage out of the condensate. Our approach gives excellent agreement with the experimental observations.

5.2 Set-Up

In the experiment, a ^{23}Na condensate with $N = 1.8 \times 10^6$ atoms was confined within a highly-oblate cylindrically symmetric harmonic trap $V_{\text{trap}}(x, y, z) = \frac{1}{2}m[\omega_r^2(x^2+y^2)+\omega_z^2z^2]$, with axial frequency $\omega_z = 2\pi \times 350$ Hz and radial frequency $\omega_r = 2\pi \times 15$ Hz (corresponding to an aspect ratio parameter $\omega_z/\omega_r \approx 23$) and where m denotes the atomic mass. A 2D mean-field description is strictly valid when the condition $Nal_z^3/l_r^3 \ll 1$ is satisfied, where $l_z = \sqrt{\hbar/m\omega_z}$ and $l_r = \sqrt{\hbar/m\omega_r}$ are the axial and radial harmonic oscillator lengths and a is the s -wave scattering length [101, 102]. For this experiment, $Nal_z^3/l_r^3 = 8.3$, i.e. the system remains 3D in nature. Nonetheless, the dynamics of the vortices is essentially 2D because of the suppression of Kelvin waves in the z -direction [103]. Therefore, we will adopt a 2D description throughout this work and show that it is sufficient to capture the experimental observations. It is worth noting that in the xy plane the condensate closely approximates a Thomas-Fermi (inverted parabola) density profile with radius $R_{\text{TF}} \approx 70\mu\text{m}$.

We parameterize the condensate by a 2D wavefunction $\phi(x, y, t)$; the condensate density distribution follows as $n(x, y, t) = |\phi(x, y, t)|^2$. The wavefunction satisfies the 2D GPE:

$$i\hbar \frac{\partial \phi}{\partial t} = \left(-\frac{\hbar^2}{2m} \nabla^2 + V(x, y, t) + g|\phi|^2 - \mu \right) \phi \quad (5.1)$$

where μ denotes the chemical potential of the condensate and $g = 2\hbar a(2\pi\omega_z\hbar/m)^{1/2}$ characterizes the effective 2D nonlinear interactions arising from s -wave atomic collisions. We solve the GPE on a 1024×1024 grid using a fourth-order Runge-Kutta method. The vortex core size is characterized by the healing length $\xi = \hbar/\sqrt{mng}$; at the condensate centre this has the value $\xi \approx 0.6\mu\text{m}$. The grid spacing is $0.27\mu\text{m}$ in both x and y , and we have verified

that reducing the grid spacing has no effect on our results.

Following the experiment, the total potential acting on the condensate $V(x, y, t)$ is the above harmonic trap plus a static Gaussian-shaped obstacle potential $V_{\text{obs}}(x, y) = V_0 \exp[-2(x^2 + y^2)/d^2]$, located at the origin, with $V_0 = 15\mu\text{m}$ and $d = 15\mu\text{m}$. The initial ground-state BEC is obtained by solving the GPE in imaginary time with enforced norm $N = 1.8 \times 10^6$. At $t = 0$ the harmonic trap is centered at $x = 18.5\mu\text{m}$. The trap is translated towards the left, at speed v , over a distance of $37\mu\text{m}$; to smooth this speed curve we additionally include a linear acceleration/deceleration over 3.75ms at the start/end, which is included as part of the $37\mu\text{m}$ translation. Once the trap is at rest, the obstacle amplitude V_0 is ramped down to zero over 0.4s.

5.3 Results

5.3.1 Number of Vortices Generated

Following removal of the obstacle, we determine the number of vortices in the system N_v (performed by identifying locations where the condensate possesses a 2π singularity in the phase). We limit our search to 75 percent of the Thomas-Fermi radius (centred on the centre-of-mass to account for sloshing motion); by avoiding the low density periphery we avoid artifacts from ghost vortices and match closely what is performed experimentally (since vortices close to the edge are not detected due to low signal-to-noise [104]). In Fig. 5.1 we plot N_v versus the translation speed v . We see the same *qualitative* form between our simulations (red circles) and the experiment (black crosses): above a critical speed $v_c \approx 0.45\text{mm/s}$ vortices enter the system, nucleated by the relative motion between the obstacle and the superfluid, and for $v > v_c$ the growth in N_v is initially rapid but tails off for $v \gg v_c$. Quantitatively, however, the GPE overestimates N_v . One can expect that thermal dissipation, not accounted for in the GPE, will act to reduce the number of vortices in the system. We introduce the effects of such dissipation via the addition of phenomenological dissipation, γ [9, 10], which enters the GPE (5.1) by replacing i on the left hand side by $(i - \gamma)$. This term induces the decay of excitations; for single vortices this manifests in them spiraling out of the trapped condensate [11, 103, 105, 106]. We choose a small value $\gamma = 0.0003$ so as to model the experiment in its very coldest realization of $\sim 130\text{nK}$ and enforce the norm throughout the dissipative simulations so as to emulate the experiment (for which no significant loss of atom number was observed).

With this dissipation the data for N_v becomes reduced, bringing it closely in line with the experimental data. Experimental limitations in resolving and counting vortices may also contribute to the over-estimate of N_v from the GPE.

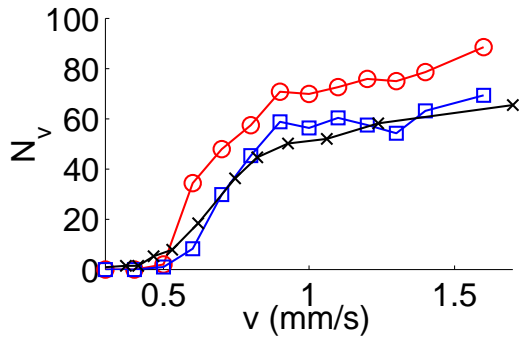


Figure 5.1: (Color online) Number of vortices N_v in the condensate after removal of the obstacle. Shown are simulations of the GPE without dissipation (red circles), with dissipation $\gamma = 0.0003$ (blue squares) and experimental results extracted from Fig. 1 of [100] (black crosses). Each point is averaged over 20 ms once the obstacle amplitude reaches $V_0 = 0$. For comparison, the speed of sound in the center of the BEC is $v_c \approx 4.6$ mm/s.

5.3.2 Stages of the Condensate Evolution

We now examine in detail the evolution of the condensate, charting its dynamics from the initial stage (when the harmonic trap translation begins) to the intermediate and final stages (randomization and decay of the vortices). We see the same qualitative evolution with and without dissipation, and for all velocities exceeding v_c . For the purposes of illustration, we focus on an example with dissipation and a translation speed $v = 1.4$ mm/s.

Figure 5.2 shows the condensate density at various times. At the start of the simulation ($t = 0$) the condensate has a smooth circular density profile, with a density depression due to the obstacle. Later vortices appear as small dots of low density; superimposed red/blue markers tag vortices of positive/negative circulation.

Vortex Nucleation and Wake Formation

To initiate the dynamics, the harmonic trap is translated to the left. This is performed sufficiently rapidly that the condensate does not adiabatically follow the trap minimum, but rather begins a sloshing motion in the trap; the centre-of-mass of the BEC oscillates at the trap frequency and the BEC undergoes a quadrupolar shape oscillation. As the BEC sloshes first to the left, its speed increases. When the local fluid velocity exceeds the speed of sound [63], vortices nucleate at the poles of the obstacle (where the local fluid velocity is the greatest) and are washed downstream (to the left). The pattern of vortices nucleated by a moving obstacle in a superfluid depends, in general, on the speed, shape and size of the obstacle [65, 64, 107]. During the initial evolution vortices of negative and positive circulation are created near each pole in an irregular manner, sometimes with alternating circulation; other times several vortices of the same circulation appear. In our case, the rate of vortex nucleation is sufficiently high that the vortices interact strongly with each other, collectively forming macroscopic clusters of negative and positive vortices downstream of the object ($t = 43$ ms). This is reminiscent of the wakes in classical viscous fluids past cylindrical obstacles [107]. During this early stage, vortices of opposite circulation may become very close and annihilate (i.e. undergo a 2D reconnection), leaving behind density

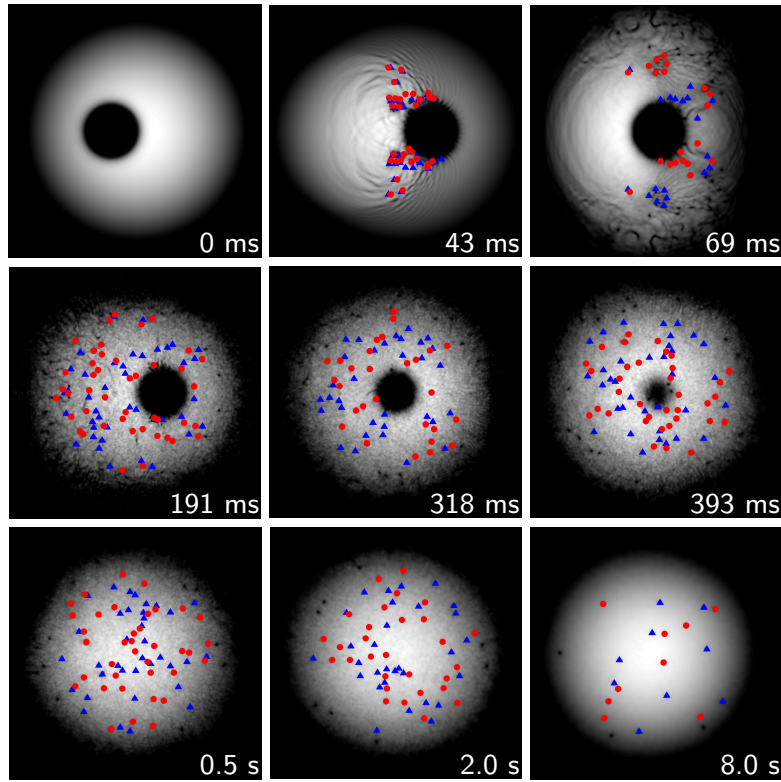
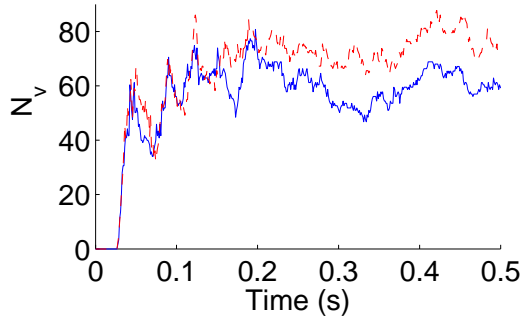


Figure 5.2: (Color online) Snapshots of the condensate density, for a translational speed $v = 1.4\text{mm/s}$ and in the presence of dissipation ($\gamma = 0.0003$). The obstacle is completely removed at 0.43s. The field of view in each subfigure is of size $[170\mu\text{m}]^2$ and shifted along the x -axis so as to best display the condensate. Vortices with positive (negative) circulation are highlighted by red circles (blue triangles).

(sound) waves. The condensate then sloshes to the right; this motion not only carries the existing vortices to the opposite (right) side of the obstacle but nucleates further vortices. As the condensate's sloshing mode is damped by the dissipation, the relative speed of the obstacle decreases and the vortex nucleation pattern changes: like-signed vortices are generated near each pole, forming symmetric classical-like wakes [107]. This effect leads to further clustering of like-signed vortices ($t = 69\text{ms}$). As the condensate continues to slosh, more vortices nucleate into the system. It must be stressed that, up to these early times ($t = 191\text{ms}$), the vortex distribution remains symmetric about the x axis. Without the dissipation term in the GPE, the sloshing mode initially decays while the obstacle is present but then persists with constant amplitude once the obstacle is removed. If dissipation is included then the sloshing mode continues to decay.

Figure 5.3: Growth of vortex number (in a single realization) at early times for a translational speed of $v = 1.4\text{mm/s}$. Shown are the results with no dissipation (red dashed line) and with dissipation $\gamma = 0.0003$ (blue solid line).



Vortex Randomization

In the presence of the obstacle and the sloshing mode, vortices continually nucleate and their spatial distribution remains approximately symmetric about the x axis. At later times ($t > 318\text{ms}$) this symmetry breaks and the vortices evolve into a completely disorganized, apparently random configuration with no significant clustering of like-signed vortices. This random distribution of vortices is consistent with the experimental observations [100]; following this we also classify the system as one of quantum turbulence. Besides vortices, the condensate contains also collective modes and an energetic, disordered sound field, with this spatial range of excitations further indicative of two-dimensional quantum turbulence [97, 99]. (Note that the typical characteristic diagnostics of steady-state 2D quantum turbulence, e.g. power-law energy spectra and the inverse energy cascade, are not appropriate here since the system is not continuously driven and does not reach steady state.)

The vortex randomization is driven by the growth of numerical noise. We have repeated our results in the presence of imposed noise (amplitude 5%, as described elsewhere [107]) and find the qualitative dynamics to be unchanged (although, as one would expect, the vortex randomization occurs at a slightly earlier time). This noise serves to model the natural fluctuations that arises in a realistic experimental scenario, e.g. due to thermal and quantum atomic fluctuations, electromagnetic noise, vibrations, etc.

It is interesting to note the obstacle is still in the system at this point, nucleating vortices in a symmetrical manner. The disorganized vortices already in the system create a velocity field which quickly mixes newly created vortices nucleated at the poles of the obstacle. Visual inspection, confirmed by a clustering-detection algorithm [87, 43], shows no significant clusters beyond this stage of the evolution. By the time the obstacle is removed the vortex configuration is essentially random, but the number of positive and negative vortices stays approximately equal. It is important to remark that, without detecting the sign of the vortex circulation, we could not reach these conclusions.

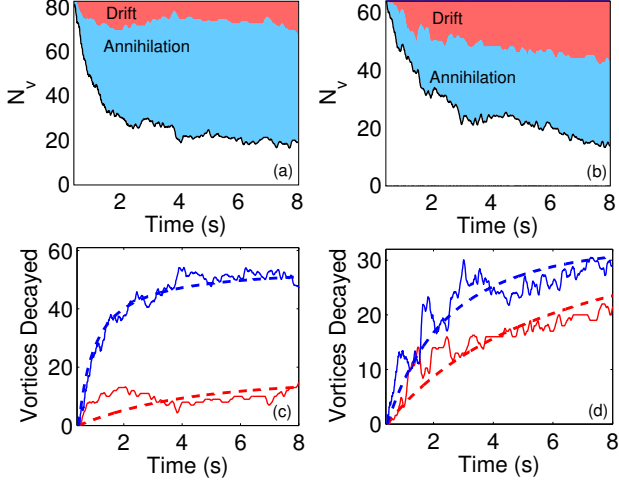


Figure 5.4: Vortex decay in the absence of dissipation (a, c) and with dissipation $\gamma = 0.0003$ (b, d) for a translational speed of $v = 1.4\text{mm/s}$. The upper figures show the decay of the total vortex number $N_v(t)$, with the contribution of drifting and annihilation depicted by the shaded regions. The lower figures show the drift number $N_d(t)$ and annihilation number $N_a(t)$, plus their respective fits.

Vortex Decay

It is clear from Fig. 5.2 that, following the removal of the obstacle, the number of vortices (N_v) depletes. Indeed, one expects that the condensate will decay towards its vortex-free, time-independent ground state. To quantify the vortex generation and decay, Fig. 5.3 plots N_v versus time. The onset of vortex nucleation is at around $t = 0.02\text{ms}$; this is the time taken for accelerating condensate to exceed the speed of sound at the poles of the object. At first N_v grows steeply, as vortices (around 40-60) are rapidly driven into the system. Subsequently, N_v grows more slowly; vortices continue to be nucleated from the obstacle but vortices undergo annihilation or move into low density regions where they are not detected. The fluctuations in N_v are amplified, particularly at early times, by the shape oscillations of the condensate, which carry vortices in and out of the detection radius. As the obstacle is removed at $t \approx 0.4\text{s}$, the surrounding condensate fills the low density area. Vortices (including some outside of the detection radius) move inwards with the flow, causing N_v to peak.

Following removal of the obstacle, the vortex number N_v decays with time. This is shown in Fig. 5.4(a) and (b) for the absence and presence of dissipation, respectively. Kwon *et al.* [100] argued that there are two mechanisms by which vortices decay: (i) thermal dissipation (resulting in drifting of vortices to the edge of the condensate), and (ii) vortex-antivortex annihilation events, and proposed that the vortex decay takes the form:

$$\frac{dN_v}{dt} = -\Gamma_1 N_v - \Gamma_2 N_v^2. \quad (5.2)$$

Here the linear and nonlinear terms, parameterized by the positive coefficients Γ_1 and Γ_2 , respectively, model these two decay processes. From our simulations we are able to independently count the number of vortices which drift out and the number which annihilate. We decompose the number of vortices according to $N_v(t) = N_{v0} - N_d(t) - N_a(t)$,

where N_{v0} is the initial number of vortices (when the obstacle is removed), $N_d(t)$ is the cumulative number of vortices which have drifted out of the condensate and $N_a(t)$ is the cumulative number which have undergone pair annihilation. The contribution of both vortex drifting and annihilation to the overall decay of N_v is depicted by the coloured regions in Fig. 5.4(a) and (b). In the absence of dissipation the vortex decay is dominated by annihilation. Indeed, apart from at early times (where internal condensate dynamics carry vortices out to high radii), no vortices drift out. In contrast, in the presence of dissipation, vortices continue to drift out over time, consistent with dissipative dynamics of single vortices [105].

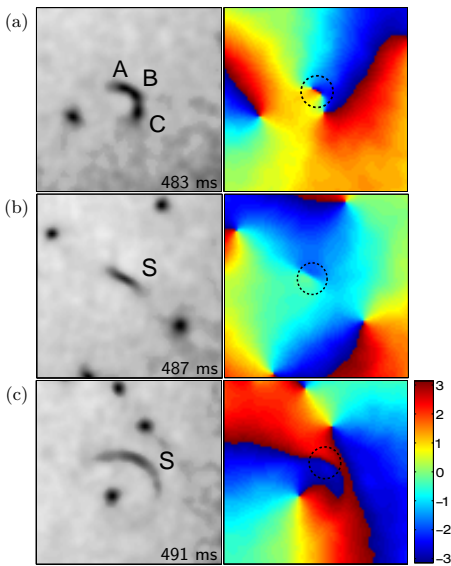


Figure 5.5: Density (left) and phase (right) just before (a), immediately following (b) and a later time after (c) a vortex-antivortex annihilation event. The field of view is $[23.5\mu\text{m}]^2$, centered on the vortex pair/sound pulse (highlighted by a circle in the phase).

Our decomposition of N_v enables us to independently fit the drift and annihilation decay processes (as two coupled ODEs for N_d and N_a , equivalent to Eq. (5.2)), with the results shown in Fig. 5.4(c) and (d). In the absence of dissipation, we find $\Gamma_2 = 0.0040$ (It is not appropriate to discuss Γ_1 since $N_d(t)$ is not of a decaying form). While the experimental observations [100] suggest Γ_2 is proportional to T^2 and thus approaches 0 as $T \rightarrow 0$, our results demonstrate a finite Γ_2 in this limit. In the presence of dissipation we obtain $\Gamma_1 = 0.093$ and $\Gamma_2 = 0.0041$, which are comparable to the coldest experiments of Kwon *et al.*

5.3.3 Crescent-Shaped Density Structures

In the experiment, Kwon *et al.* observed the occasional appearance of crescent-shaped waves of depleted density. Lacking direct access to the vortex signs, they suggested that these structures result from annihilation events of vortices of opposite circulation [108, 109, 110]: a vortex reconnection is predicted to induce an intense, localised, rarefaction sound pulse [111, 112]. Figure 5.5 shows snapshots of the condensate density and phase during a reconnection event. Vortices show up as localized dips in the density (left column) and 2π -defects in the phase (right column). Figure 5.5 (a) shows a vortex (A) and antivortex (B) close to each other, and a third vortex (C) in the vicinity. Note that the individual vortices are not spatially resolvable through their density alone (the vortex cores merge into a deep, elongated crescent-shaped depression), but they are clearly identified by the phase plot.

A short time later (b), vortices A and B annihilate, as confirmed by the disappearance of their phase singularities, leaving behind a shallow rarefaction pulse (S) with a linear phase step. This pulse rapidly evolves into a shallow, crescent-shaped sound wave [Fig. 5.5 (c)]. In other words, our simulations yield crescent-shaped density features as seen in the experiment, but these features are not uniquely formed by annihilation events - they may also result from two (or more) vortices in close proximity. Information about the condensate phase is thus crucial to distinguish the nature of these observed structures. In this direction, an approach has recently been proposed for the experimental detection of quantized vortices and their circulation in a 2D BEC [113].

5.3.4 Vortex Generation via an Elliptical Obstacle

It is evident from the snapshots in Figure 2 that the initial translation of the condensate past the obstacle generates not just vortices but also shape excitations, sound waves (low-amplitude density waves), and high-amplitude density waves. These additional excitations will heat the condensate and modify the subsequent turbulent dynamics in a highly nonlinear and complicated manner. While reducing the translational speed reduces this disruption, this also reduces the number of vortices. A less disruptive and more efficient (higher rate of vortex nucleation) means to generate vortices may be provided by employing a laser-induced obstacle with *elliptical*, rather than circular, cross-section (attainable through cylindrical beam focusing). Repeating our simulations with such an elliptical obstacle $V_{\text{obs}}(x, y) = V_0 \exp[-2(\epsilon^2 x^2 + y^2)/d^2]$ with arbitrary ellipticity $\epsilon = 3$ (the short/long axis being parallel/perpendicular to the flow) confirms the same qualitative behaviour as for homogeneous systems [107]: the ellipticity acts to reduce the critical superfluid velocity and, for a given flow speed, increase the rate of vortex nucleation. To illustrate the merits of the elliptical obstacle, in Fig. 6 we depict snapshots of the condensate dynamics for ellipticity $\epsilon = 3$ and a translational speed of $v = 0.8\text{mm/s}$. Despite a lower translational speed, the number of vortices generated by the time the obstacle is removed is almost identical to the circular example of Fig. 3. As a consequence of the reduced translational speed, the condensate disruption is visibly reduced. It is also worth noting that the elliptical obstacle promotes the formation of clusters of like-signed vortices (see intermediate time), and thus may facilitate future exploration of coherent vortex structures.

5.4 Conclusion

In conclusion, we have shown that the recent experimental creation and decay of vortices within a BEC [100] is well described by simulations of the 2D GPE with phenomenological dissipation (despite the 3D nature of the system). Theoretical access to the condensate phase, and thus the circulation of the vortices, promotes our understanding of the dy-

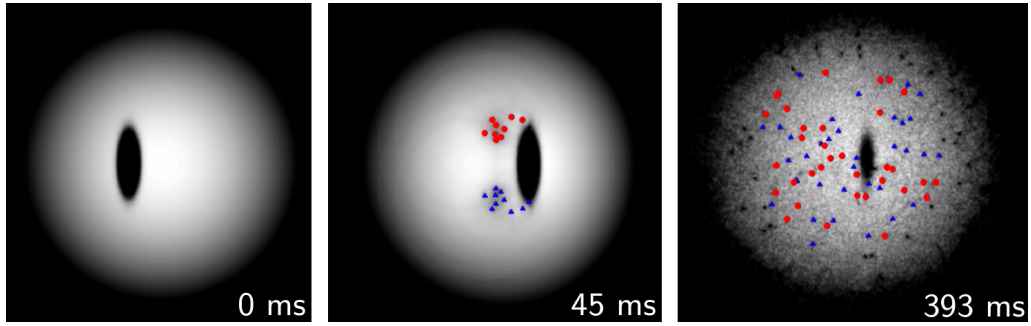


Figure 5.6: (Color online) Snapshots of the condensate density for a translational of speed $v = 0.8\text{mm/s}$ past an elliptical obstacle (ellipticity $\epsilon = 3$). The field of view in each subfigure is of size $[170\mu\text{m}]^2$ and shifted along the x -axis so as to best display the condensate. Compared to the corresponding snapshots in Figure 2, the elliptical obstacle generates as many final vortices but at a lower translational speed and with reduced condensate disruption.

namics. In the early stages of translation of the obstacle, a quasi-classical wake of vortices forms behind it, before symmetry breaking causes disorganisation of the vortices. After the obstacle is removed, the vortices decay in a manner which is both qualitatively and quantitatively consistent with the two mechanisms proposed by Kwon *et al.*, i.e. loss of vortices at the condensate edge due to thermal dissipation and vortex-antivortex annihilation events within the condensate. We confirm the occasional appearance of crescent-shaped density features, resulting either from the proximity of vortex cores or from a sound pulse which follows a vortex-antivortex reconnection. Finally, we propose that a moving *elliptical* obstacle may provide a cleaner and more efficient means to generate two-dimensional quantum turbulence.

Chapter 6

Critical velocity at finite temperature

6.1 Introduction

A defining feature of superfluids is the absence of excitations when the flow (relative to some obstacle or boundary) is slower than a critical velocity; above this velocity, the flow becomes dissipative. This can be understood in terms of the Landau criterion, which predicts excitations when the local fluid velocity exceeds $v_L = \min[E(p)/p]$, where p is the momentum of elementary excitations and $E(p)$ their energy [85]. In weakly-interacting atomic Bose-Einstein condensates, and for infinitesimally small perturbations, one obtains $v_L = c$, the speed of sound. The breakdown of superfluidity has been experimentally probed by introducing a localized repulsive obstacle, engineered via the repulsive force generated by focussed blue-detuned laser beam, and moving the condensate relative to the obstacle [83, 100, 114, 115, 80, 81, 82, 116]. This has enabled measurement of the critical velocity and the direct observation of the ensuing excitations, that is, pairs of quantized vortex lines with opposite polarity. In flattened condensates, this scenario currently provides a route to engineer states of two-dimensional quantum turbulence [83, 100]; it also gives insight into the deep link between quantum fluids and their classical counterparts, where it has been predicted that the wake of quantized vortices produced downstream of the obstacle can collectively mimick the classical wakes, including the Bérnard-von Kármán vortex street [64, 107, 46].

The motion of an obstacle in the zero-temperature Bose gas, described by the Gross-Pitaevskii equation, is a well-studied problem, particularly for circular obstacles in 2D geometries. The pioneering simulations by Frisch *et al.* [63] of an impenetrable circular obstacle moving within the 2D nonlinear Schrödinger equation (NLSE), demonstrated the existence of a critical velocity of value $v_c \sim 0.4c$ above which vortex-antivortex pairs are nucleated. For small obstacles, boundary effects tend to suppress vortex nucleation, and, as the obstacle's size increases, the critical velocity reduces towards an asymptotic

value [72, 73, 74]. The critical velocity also depends on the shape of the obstacle, for example, obstacles with elliptical cross-section lead to reduced/heightened v_c , depending on the orientation relative to the flow [107, 117]. Similar behaviour holds for spherical obstacles, albeit with the emission of vortex rings and increased critical speeds of circa $0.7c$ [118, 86, 107]. In current condensate experiments [83, 100, 80, 81, 82, 116, 114, 115], the obstacles are penetrable, corresponding to a Gaussian potential of finite amplitude, produced via an incident blue-detuned laser beam. The same qualitative behaviour emerges for impenetrable obstacles, although the critical velocity and vortex nucleation patterns become modified [64].

Very recently, Kwon *et al.* have undertaken a systematic experimental analysis of the critical velocity for vortex shedding, exploring the dependence of the nucleation on height and width of the penetrable obstacle and the crossover from penetrable to impenetrable obstacles [114]. Their results, obtained in a condensate with temperature much lower than the critical temperature for condensation, are in agreement with previous zero-temperature predictions based on the Gross-Pitaevskii equation. Their work has made a significant step in consolidating our theoretical and experimental understanding of the critical velocity in a condensate in the zero-temperature limit. At the same time, it has highlighted the need to extend the study of the critical velocity to finite temperatures. While the role of finite temperature has been explored considerably for another vortex nucleation scenario, namely within deformed, rotating traps [119, 120, 121, 12, 122, 123] (for which unstable surface modes underpin the vortex nucleation), there is a paucity of literature relating to the finite temperature behaviour of vortex nucleation by a translating obstacle. Indeed, to our knowledge, the only finite-temperature analysis of a moving obstacle in a three-dimensional condensate is that of Leadbeater *et al.* [124], who found that the critical velocity of a hard sphere decreases with temperature.

In this work we study the motion of a cylindrical Gaussian-shaped obstacle through a three-dimensional homogeneous Bose gas at finite temperature via classical field simulations. We find that the critical velocity decreases with temperature and increases with condensate fraction (ratio of condensate to total density). Indeed, the critical velocity is found to be closely proportional to the speed of sound of the condensate, which scales as the square root of the condensate fraction. Above the critical velocity, vortex nucleation occurs either through pairs of vortex lines, collections of vortex rings, or direct formation of a vortex tangle, and we indicate the occurrence of these structures in the parameter space of condensate fraction and flow speed.

6.2 Classical Field Method

We consider a weakly-interacting Bose gas with N atoms in a periodic box of volume ℓ^3 . The atoms have mass m and their interactions are approximated by a contact pseudo-potential $V_{\text{int}}(\mathbf{r} - \mathbf{r}') = g\delta(\mathbf{r} - \mathbf{r}')$, where g is a coefficient which characterises the atomic interactions and δ is the Dirac delta function [125].

In order to theoretically model thermal excitations of the weakly-interacting Bose gas, one must progress beyond the standard mean-field approximation to include both the condensate and the thermal fraction atoms in the gas. Various methods have been proposed for this purpose, as reviewed elsewhere [126, 127, 128, 129, 130, 131]. Among these methods, a popular one is the classical field method [132, 133, 134, 14, 135, 136, 126]. This method is based on the observation that, providing the modes of the gas are highly occupied (an *a priori* assumption in our work), then the gas can be approximated by a classical field $\psi(\mathbf{r}, t)$ whose equation of motion is the Gross-Pitaevskii equation (GPE). However, whereas the GPE conventionally describes the condensate only, $\psi(\mathbf{r}, t)$ now describes the entire multi-mode ‘classical’ gas [127, 130]. The classical field method has been used to model phenomena beyond-mean-field effects, including thermal equilibration dynamics [14, 136, 137, 138], condensate fractions [133], critical temperatures [139], correlation functions [140], spontaneous production of vortex-antivortex pairs in quasi-2D gases [141], thermal dissipation of vortices [142], and related effects in binary condensates [143, 144, 137].

We parameterize the gas by the classical field $\psi(\mathbf{r}, t)$. The density distribution of atoms is then $|\psi(\mathbf{r}, t)|^2$. The evolution of ψ is governed by the GPE

$$i\hbar \frac{\partial \psi}{\partial t} = \left(-\frac{\hbar^2}{2m} \nabla^2 + V_{\text{obj}}(\mathbf{r}, t) + g |\psi|^2 \right) \psi, \quad (6.1)$$

where $V_{\text{obj}}(\mathbf{r}, t)$ is the externally applied potential. The GPE conserves the total number of particles, $N = \int |\psi|^2 dV$, and the total energy,

$$H = \int \left(\frac{\hbar^2}{2m} |\nabla \psi|^2 + V_{\text{obj}} |\psi|^2 + \frac{g}{2} |\psi|^4 \right) dV.$$

In what follows we express all quantities in terms of the natural units of the homogeneous Bose gas: density in terms of a uniform value ρ , length in terms of the healing length $\xi = \hbar/\sqrt{mg\rho}$, speed in terms of the speed of sound $c = \sqrt{\rho g/m}$, energy in terms of the chemical potential of the homogeneous condensate $\mu = \rho g$, and time in terms of $\tau = \hbar/g\rho$.

We label the modes of the system through the wavevector \mathbf{k} . To allow for occupation

across all classical modes of the system, the initial condition is highly non-equilibrium,

$$\psi(\mathbf{r}, 0) = \sum_{\mathbf{k}} a_{\mathbf{k}} \exp(i\mathbf{k} \cdot \mathbf{r}) \quad (6.2)$$

where the coefficients $a_{\mathbf{k}}$ are uniform and the phases are distributed randomly [14]. The occupation of mode \mathbf{k} is $n_{\mathbf{k}} = |a_{\mathbf{k}}|^2$. The final temperature/condensate fraction of our simulations is varied through a rescaling of ψ , so as to fix the quantities N and H .

The GPE is evolved numerically, in the absence of any potential V_{obj} , using a fourth-order Runge-Kutta method on a 192^3 periodic grid with time step $\Delta t = 0.01\tau$ and isotropic grid spacing $\Delta = 0.75\xi$. The spatial discretization of our numerical grid implies that high momenta are not described in our simulations. In effect, an ultraviolet cutoff is introduced, $n_{\mathbf{k}}(t) = 0$ for $k > k_{\max}$, where $k = |\mathbf{k}|$ and the maximum described wave vector amplitude is $k_{\max} = \sqrt{3}\pi/\Delta$.

The ensuing evolution from the strongly nonequilibrium initial conditions has been outlined previously [14, 137]. Initially the mode occupation numbers n_k are uniformly distributed over wavenumber k , up to the cutoff. Self-ordering leads to the rapid growth in the occupation of low- k modes, which initially evolves in a state of weak turbulence. Then the distribution evolves to a bimodal form. The high- k part of the distribution is associated with the thermal excitations and low mode occupations. The low- k part of the field is the quasi-condensate, characterised by macroscopic mode populations and superfluid ordering.

From the bimodal distribution, a wavenumber k_c can be chosen as the boundary in k -space between the quasi-condensate and the thermal gas, as performed in [14]. Here we take $k_c \approx 13(2\pi N^{-1}\xi^{-1})$, although our qualitative results are insensitive to the precise definition of k_c . The condensate density, ρ_0 , is then calculated as the density within the quasi-condensate, i.e. a coarse-grained averaging over the quasi-condensate modes. This is then used to define the condensate fraction, ρ_0/ρ , where ρ is the total density of the gas.

While the raw wavefunction is too noisy to allow direct visualization of vortical structures, this can be overcome by defining a quasi-condensate wavefunction $\hat{\psi}$, as established in [14]. This wavefunction is constructed by filtering out high-frequency spatial modes from the classical field wavefunction, by transforming the complex amplitudes via $\hat{a}_{\mathbf{k}} = a_{\mathbf{k}} \times \max\{1 - k^2/k_c^2, 0\}$. $\hat{\psi}$ represents the long-wavelength component of the classical field.

The quasi-condensate features a tangle of quantized vortices which relaxes over very long times, and the final equilibrium state is free of vortices. Its physical properties, e.g. temperature and condensate fraction, are uniquely determined by the number of particles N and the kinetic energy $E = \int (\hbar^2/2m)|\nabla\psi|^2 dV$ of the system [136]. The equilibrium state of the non-condensed particles follows the Rayleigh-Jeans distribution, modified by

	Initial conditions					
$N/\ell^3 (\xi^{-3})$	0.50	0.50	0.50	0.50	0.50	0.50
$\langle H \rangle / \ell^3 (\mu \xi^{-3})$	2.57	2.13	1.75	1.33	0.53	0.23
Equilibrium state						
ρ_0/ρ	0.02	0.22	0.36	0.48	0.77	0.91
T/T_λ	0.98	0.81	0.68	0.56	0.26	0.10

Table 6.1: Condensate fraction and temperature of the equilibrium classical field state for our chosen initial conditions.

the nonlinear interaction with the condensed particles [136]. It is interesting to note that the equilibrium condensate fraction is insensitive to the number of modes, providing that the number of modes is, or exceeds, 16^3 modes. This suggests that this number of modes is sufficient to model the thermodynamic limit of the system. For comparison, we employ 192^3 modes.

Here we parametrise the system in terms of its particle density $\rho = N/\ell^3$ and average energy density $\langle H \rangle / \ell^3$. Note that the total energy $H = E + E_0$, where E is the kinetic energy of the system and E_0 is the energy of the condensate [136]. The temperature is evaluated from the condensate fraction using the following empirical relationship established in Ref. [142]:

$$\frac{T}{T_\lambda} = 1 - (1 - \alpha\sqrt{\rho})\frac{\rho_0}{\rho} - \alpha\sqrt{\rho} \left(\frac{\rho_0}{\rho}\right)^2, \quad (6.3)$$

where T_λ is the critical temperature for condensation and $\alpha = 0.2275$ is a fitting parameter. Table 6.1 lists the parameters chosen in our simulations and the resulting condensate fractions and temperatures of the ensuing equilibrated classical field states.

6.3 Equilibration dynamics and decay of the vortex tangle

The ensuing evolution from the strongly nonequilibrium initial conditions has been outlined previously [14, 137]. Initially the mode occupation numbers n_k are uniformly distributed over wavenumber k , up to the cutoff. Self-ordering leads to the rapid growth in the occupation of low- k modes, which initially evolves in a state of weak turbulence. The distribution evolves to a bimodal form. The high- k part of the distribution is associated with the thermal excitations and low mode occupations. The low- k part of the field is the quasi-condensate, characterised by macroscopic mode populations and superfluid ordering. The quasi-condensate is formed featuring a tangle of quantized vortices. Over very long times, this tangle relaxes. The final equilibrium state, including its final condensate fraction and temperature, is free of superfluid vortices and uniquely determined by the number of particles N and the kinetic energy $E = \int (\hbar^2/2m)|\nabla\psi|^2 dV$ of the system [136].

Figure 6.1 shows the typical evolution of the quasi-condensate during the equilibration

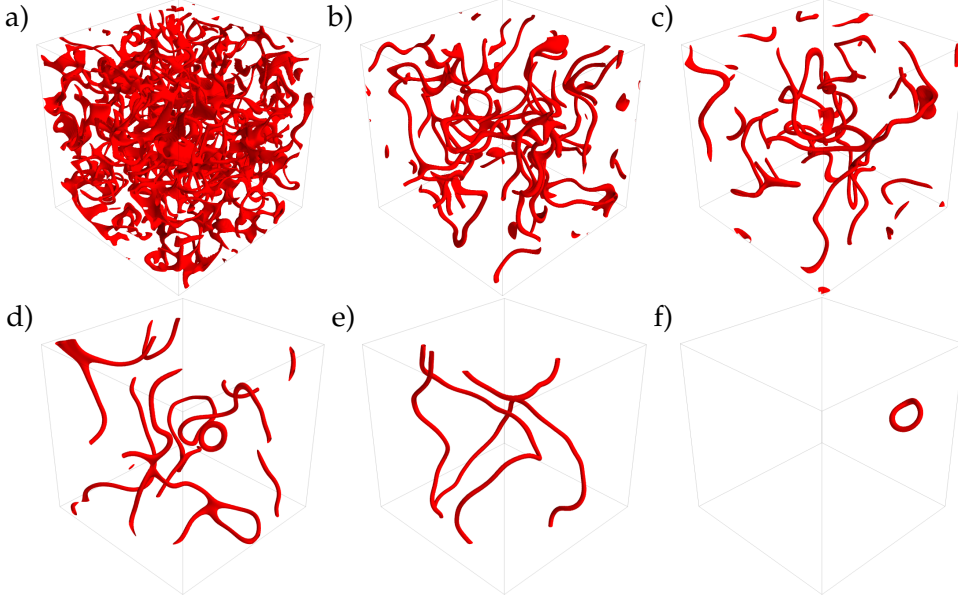


Figure 6.1: (Color online) Evolution of the quasi-condensate vortex tangle during the equilibration dynamics at times (a) $t/\tau = 0$, (b) 500, (c) 1000, (d) 2000, (e) 4000, and (f) 10 000. Shown are isosurfaces of the quasi-condensate density $|\hat{\psi}|^2 = 0.04 \langle |\hat{\psi}|^2 \rangle$. At later times all vortices disappear. Note that vortices cannot be visualized directly from the raw ψ due to the significant thermal fluctuations.

dynamics through iso-surface plots of the quasi-condensate density $|\hat{\psi}|^2$. The iso-surface density value ($0.04 \langle |\hat{\psi}|^2 \rangle$) is sufficiently low that only vortex cores are evident. The initially-formed dense vortex tangle relaxes over time. It remains random and isotropic throughout. Typically, the tangle relaxes to leave one or more vortex rings, which also relax, eventually leading to a vortex-free state. This is deemed the “equilibrated” state.

We can further analyse the vortex relaxation through the evolution of the vortex line-length density, L . It is convenient to evaluate the total vortex line length in terms of the total length of the isosurface tubes. We assume that each tube has uniform circular cross-sectional area A_t , measured by inspection of a given vortex line. Note that the assumption of uniform cross-section will be valid for the majority of vortex line length, but will deviate slightly where two vortices approach each other. The total tube length (viz. vortex line length) is then V_t/A_t , where V_t is the total tube volume.

The characteristic time of the evolution of the vortex tangle is $R^2 / \ln(R/a_0)$, depending on the typical inter-vortex spacing, R , and the core size a_0 [145]. As the tangle dissipates the inter-vortex spacing increases, and so although most vortices dissipate at early times, for relatively large boxes, it can take a very long time for every single vortex to dissipate and the condensate to reach the equilibrium state. A sample of evolutions of the vortex volume during equilibration is shown in Figure 6.2. The tangle decay rate lies in reasonable agreement with the decay of a vortex tangle in a ‘random’ Vinen state, with $L(t) \sim t^{-1}$.

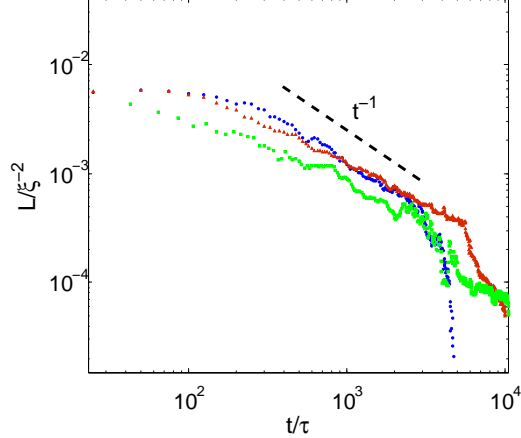


Figure 6.2: (Color online) Decay of the vortex line-length density during the equilibration dynamics, for various values of final condensate fraction: $\rho_0/\rho = 0.2$ (blue circles), $\rho_0/\rho = 0.5$ (brown triangles) and $\rho_0/\rho = 0.9$ (green squares)

6.4 Moving obstacle at finite-temperature

6.4.1 Critical velocity for vortex nucleation

Having obtained the equilibrated finite-temperature states of the Bose gas, we now move on to consider a laser-induced obstacle moving through the gas. The obstacle, uniform in z , is translated in the x -direction at speed v . Our simulations are conducted in the frame moving with the obstacle, modelled by the inclusion of a Galilean shift term $i\hbar v \partial_x \psi$ to the right-hand side of the GPE. In this frame the obstacle is imposed through the time-independent potential $V_{\text{obj}}(\mathbf{r}) = V_0 \exp [-(x^2 + y^2)/d^2]$, where d and V_0 parameterize the width and amplitude of the potential. The amplitude is linearly increased from $V_0 = 0$ at first introduction to its maximal value $V_0 = 5\mu$ over a period of 200τ . The frame speed is increased adiabatically to the required value according to the temporal profile $v \tanh(\hat{t}/200\tau)$, where \hat{t} denotes the time from introduction of the obstacle.

Simulations are repeated (from identical initial conditions) with increasing terminal speeds (in steps of $0.057c$) until vortices are detected. Vortex detection is by visual inspection of the filtered density, up to a maximum simulation time $\hat{t} = 500\tau$ (which is long enough to ensure that the obstacle is fully introduced and at terminal speed, but otherwise arbitrary). This procedure defines the critical velocity v_c . There is a systematic uncertainty in our measurement of v_c , arising from the discrete terminal speeds employed. Note that we have repeated this process for multiple randomized initial conditions, and find no change in our measurement of v_c ; that is, the systematic uncertainty due to using discretized speeds is larger than the statistical uncertainty arising from different random initial conditions.

Figure 6.3 shows the variation of v_c with both condensate fraction ρ_0/ρ (lower abscissa)

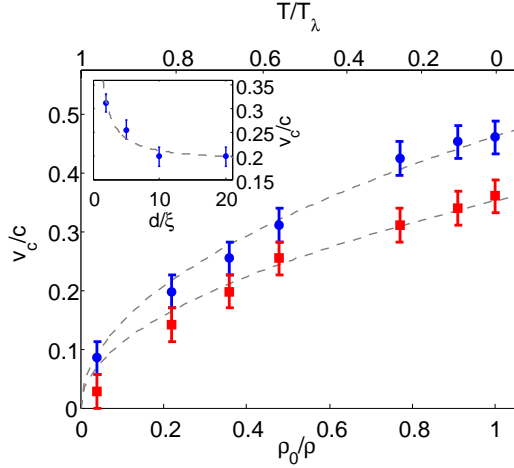


Figure 6.3: (Color online) Critical velocity v_c for the moving Gaussian-shaped obstacle (uniform in z) as a function of condensate fraction ρ_0/ρ and temperature T/T_λ , for obstacle widths $d = 2\xi$ (blue circles) and $d = 5\xi$ (red squares). The dotted lines show the analytic model $v_c = \beta\sqrt{\rho_0/\rho}$ with fitted coefficients $\beta = 0.46$ and 0.35 . (Inset) The critical velocity approaches an asymptotic value as the obstacle size is increased. Included is a fit of the form $v_c = \alpha/d + \gamma$ with $\alpha = 0.26 (\xi^2/\tau)$ and $\gamma = 0.18c$. Errors bars represent the systematic uncertainty in v_c due to the discretized values of v considered.

and temperature T/T_λ (upper abscissa), for two example obstacles widths. The critical velocity has a maximum value at zero temperature (unit condensate fraction), and decreases nonlinearly as temperature increases (condensate fraction decreases), reaching zero at the critical point for condensation.

At zero temperature, the critical velocity is of the order of the condensate speed of sound $c = \sqrt{\rho g/m}$, with a general form $v_c(T = 0) = \beta c$, where β is a parameter which depends solely on the shape of the obstacle (here d and V_0). The simulated v_c data in Figure 6.3 closely follow the simple functional form $v_c(T) = v_c(0)\sqrt{\rho_0/\rho}$, as shown by the dashed lines. An expression for the critical velocity valid at zero and non-zero temperatures is

$$v_c(T) = \beta\sqrt{\rho_0 g/m}. \quad (6.4)$$

In other words, for a given obstacle, the critical velocity is a fixed fraction of the speed of sound based on the *condensate* density rather than the total particle density [124].

The inset of Figure 6.3 shows the variation of v_c with the obstacle width d at finite temperature, for the example of $T/T_\lambda = 0.56$. The qualitative behaviour is consistent with that seen at zero temperature [69, 73, 107]: for small d the critical velocity is sensitive to d (due to the prominence of boundary layer effects) but as d increases v_c decreases towards a limiting values (the Eulerian limit). However, the critical velocities are systematically reduced compared to the zero temperature case due to the reduced condensate speed of sound at finite temperature.

6.4.2 Vortex nucleation pattern

Finally we examine the manner in which vortices are nucleated from the obstacle. At zero temperature, one expects the nucleation of straight anti-parallel vortex lines from the obstacle, either released in unison or staggered in time [63, 64, 107], which move downstream relative to the obstacle. At finite temperature, we observe three general regimes of vortex nucleation, with representative examples shown in Fig. 6.4:

Vortex lines A pair of “wiggly” vortex lines is produced [Fig. 6.4(a)]. The wiggles are driven by the thermal fluctuations, which cause the vortex elements to be nucleated at slightly different times along the obstacle; this is visible at intermediate times (snapshots (iii) and (iv)). These elements ultimately merge together along the axis of the obstacle to form a wiggly vortex/anti-vortex line. Similar vortex configurations in the form of lines which are partially attached to a thin wire were also observed in liquid helium [146].

Vortex rings Here vortices predominately form vortex rings [Figure 6.4(b)]. The vortex loops generated at the obstacle rapidly peel away from the obstacle, reconnecting with adjacent loops to form rings. Due to the way the vortex rings form initially along the obstacle, they are elliptical and polarised such that they are longer along the obstacle axis.

Vortex tangle Strong interaction between successively nucleated vortices leads to the formation of a complex tangle of vortex lines behind the obstacle [Figure 6.4(c)].

While the vortex line regime is analogous to the zero temperature case, no analog occurs for the ring and tangle regimes. We note that even a small amount of thermal fluctuations is enough to vastly change the form of vortex nucleation, such as the vortex rings produced in Fig. 6.4(c) for a condensate fraction of 0.91.

To systematically map the occurrence of these regimes, we measure the vortex line-length density L (length of vortex line per unit volume) and vortex polarity R (described below) at a fixed observation time of $\hat{t} = 500\tau$, throughout the parameter space of flow velocity and condensate fraction. Our method to evaluate the vortex line-length density is described in Appendix A. The results are presented in Fig. 6.5. Below the critical velocity (solid black line) no vortices are produced, and thus $L = 0$. Above the critical velocity, L increases strongly with the flow velocity. This is to be expected since the frequency of vortex nucleation increases with flow velocity [63]. L also increases with decreasing condensate fraction (increasing temperature), indicating the significant role of thermal fluctuations in enhancing vortex production.

Just above the critical velocity, where the vortex line-length density is relatively small, vortex nucleation occurs through vortex lines and rings. The low flow velocity ensures

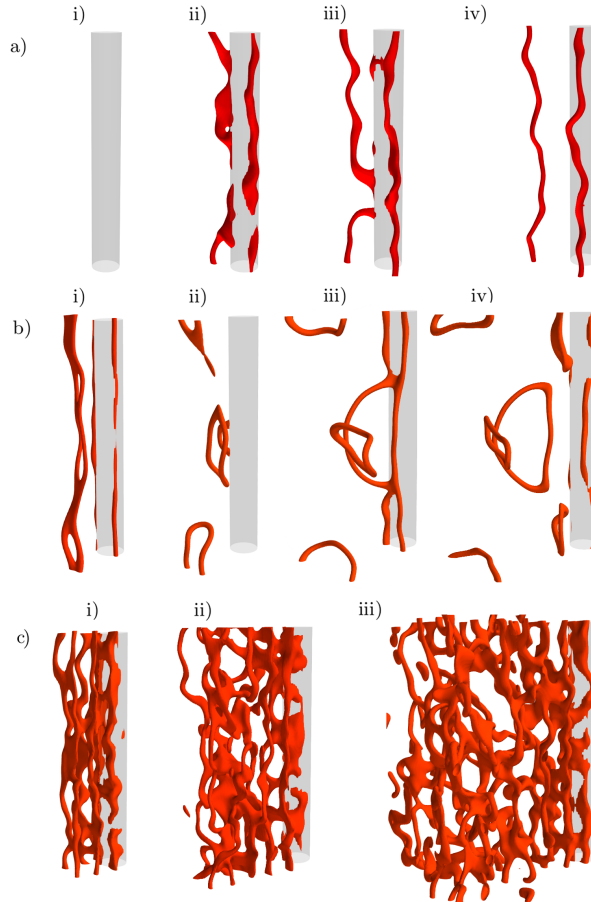


Figure 6.4: (Color online) Snapshots of the typical vortex nucleation from the moving Gaussian-shaped obstacle with $d = 5\xi$ (gray) in the finite temperature Bose gas. The three cases (a-c) are representative of the behaviour across the whole parameter space shown in Fig. 6.5. Shown are isosurfaces of the quasi-condensate density ($|\hat{\psi}|^2 = 0.04 \langle |\hat{\psi}|^2 \rangle$). (a) Vortices are shed as pairs of anti-parallel vortex lines. Here the system parameters are $\rho_0/\rho = 0.22$ and $v = 0.17c$, and the snapshots correspond to times (i) $\hat{t}/\tau = 210$, (ii) 460, (iii) 585 and (iv) 710. (b) Vortex rings are nucleated from the obstacle. The system parameters are $\rho_0/\rho = 0.91$ and $v = 0.42c$, and the times are (i) $\hat{t}/\tau = 500$, (ii) 700, (iii) 875 and (iv) 950. (c) A vortex tangle forms behind the obstacle. The system parameters are $\rho_0/\rho = 0.35$ and $v = 0.59c$, and the times are (i) $\hat{t}/\tau = 250$, (ii) 375 and (iii) 500.

that the vortex nucleation frequency is low, thereby suppressing strong interaction or reconnection between nucleated vortices. Here, whether lines or rings are produced is sensitive to the random initial conditions, and so it is not possible to further distinguish these nucleation regimes within this parameter space. In these cases a more consistent characterisation of the vortex form is given by R , described below. At higher flow velocities, where the vortex line-length density is relatively high, the nucleation frequency becomes sufficiently high that vortices immediately undergo strong interactions with each other, reconnecting and developing into a vortex tangle. The transition in the parameter space from vortex lines/rings to tangles is indicated approximately by the dashed line, although statistical effects blur the true boundary.

We further characterise the vortex distribution by its polarisation through the quantity $R = A_z/(A_y + A_z)$, where A_y and A_z are the total area of vortices when the vortex distribution is projected along the y and z directions, respectively. A value $R \approx 0$ corresponds to vortex lines aligned predominantly along the z axis, $R \approx 1$ corresponds to lines aligned predominantly along y , and $R \approx 0.5$ corresponds to an isotropic vortex distribution (in the yz plane). The parameter space of R has the same qualitative form as that for L , increasing with velocity and decreasing with condensate fraction. R typically lies in the range $0.1 \leq R \leq 0.4$ for the lines/rings regime, consistent with the presence of lines which are predominantly aligned along z and rings which are elongated along z . It is worth noting that while the occurrence of lines or rings, for a given flow velocity and condensate fraction, is sensitive to the initial conditions, the value of R is highly reproducible (to within a few percent). For the vortex tangle regime, $0.4 \leq R \leq 0.5$. It is worth noting that this shows that the produced tangle can be highly isotropic, despite two-dimensional nature of the obstacle that generates it.

6.5 Conclusions

Using classical field simulations, we have analysed the nucleation of vortices past a moving cylindrical obstacle in a finite temperature homogeneous Bose gas. We have evolved the classical field from highly non-equilibrium initial conditions to thermalized equilibrium states with ranging temperatures and condensate fractions. We have then inserted a cylindrical obstacle with Gaussian profile into the system, and imposed a flow relative to the gas. We have found that, above the critical velocity, vortices are nucleated forming wiggly anti-parallel pairs of vortex lines, vortex rings, or as a vortex tangle. The critical velocity decreases with increasing temperature, becoming zero at the critical temperature, and scales with the speed of sound of the condensate, i.e. as the square root of the condensate fraction. While our work is based on a homogeneous system, in reality Bose-Einstein condensates are experimentally confined in traps, rendering the gas inhomogeneous. Then one can

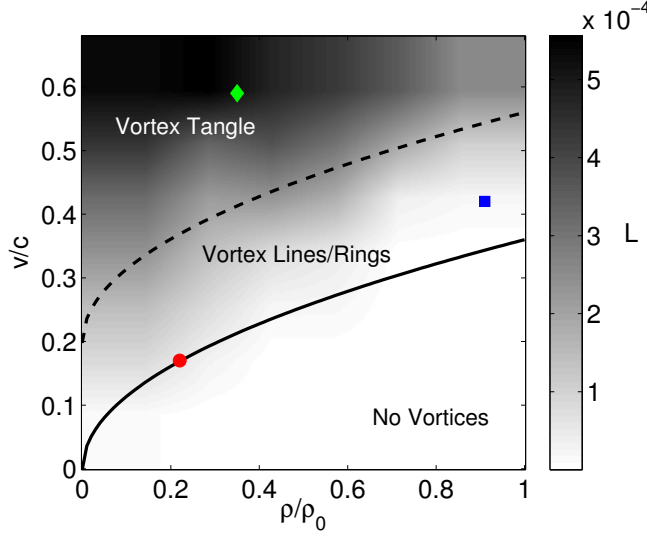


Figure 6.5: Vortex line density L (at an observation time $\hat{t} = 500\tau$) as a function of flow speed and condensate fraction, with the qualitative regimes of vortex nucleation indicated. The markers correspond to the three representative cases shown in Figure 6.4(a) [red circle], (b) [blue square] and (c) [green diamond]. This line length density data, obtained from 36 simulations, has been interpolated. The obstacle has size $d = 5\xi$.

expect corrections to the critical velocity due to density gradients, as well as modifications to the vortex nucleation pattern. These higher order effects could be studied in future work. However, we note that recent advances have led to the formation of quasi-homogeneous condensates in box-like traps [147, 148], where these corrections should have minimal effect.

Chapter 7

Simulating the surface of a “Floppy Wire”

7.1 Introduction

At sufficiently low temperatures, liquid helium has two striking properties. Firstly, it flows without viscosity. Secondly, its vorticity is constrained to thin mini-tornadoes, characterised by their fixed circulation h/m (the ratio of Planck's constant to the mass of the relevant boson - one atom in ^4He and one Cooper pair in $^3\text{He-B}$) and microscopic core radius ξ (0.1 nm in ^4He and 10 nm in $^3\text{He-B}$). In contrast, the eddies in everyday viscous fluids can have arbitrary shape, size and circulation.

Of ongoing experimental and theoretical study is the nature of turbulence in superfluids [? ? ? ?], a state dominated by an irregular tangle of quantised vortex lines. Despite the fundamental differences between superfluids and classical fluids, the observations of Kolmogorov energy spectra, famed from classical isotropic turbulence, in superfluid turbulence [?] are suggestive of a deep connection between them. Superfluid turbulence is nowadays most commonly formed by moving obstacles, including grids [25], wires [26? , 28, 29], forks [31, 32], propellers [? ?], spheres [33] and other objects [24]. Despite progress in visualizing the flow of superfluid helium in the bulk [? ?], including individual vortex reconnections [?], there is little direct experimental evidence about what happens at boundaries. Here, vortices are believed to be generated by two mechanisms. Firstly, they can nucleate at the boundary of the vessel or object. When the relative flow speed is sufficiently low, the flow is laminar (potential) and dissipationless. Near curved boundaries, however, vortex nucleation occurs if the local flow velocity exceeds a critical value. Secondly, the vortices can be procreated from so-called ‘remnant vortices’ which are present in the system since cooling the helium through the superfluid transition. Note that remnant vortices can be avoided using judicious, slow experimental protocols [?].

The nano-scale vortex core in superfluid helium is comparable in size to the typical roughness of the boundaries of the vessel or stirring object. Unfortunately the lack of direct experimental information about vortex nucleation at the boundaries and the subsequent vortex-boundary interactions, limit the interpretation of experiments. Theoretical progress is challenging and to date has focussed on smooth and idealised surfaces. In principle, the superfluid boundary conditions are straightforward: the superfluid velocity component which is perpendicular to the boundary must vanish at the boundary, whereas the tangential component (in the absence of viscous stresses) can slip. For the latter reason, we do not expect boundary layers, typical of viscous flows. Implementing these superfluid boundary conditions, Schwarz [?] and Tsubota *et al.* [?] found that one or more vortices sliding along a smooth surface can become deflected or trapped by a small hemispherical bump. Such bumps can also serve as nucleation sites for vortices; the local superfluid velocity is raised at the pole of the bump and more readily breaks the critical velocity for vortex nucleation [?]. Moreover, recent simulations [?] show that, if the bump is elliptically shaped and elongated perpendicular to the imposed flow, the superfluid velocity at the pole is enhanced, reducing the critical velocity for vortex nucleation and increasing the vortex nucleation rate (for a given super-critical imposed flow). We expect therefore that microscopically-small surface roughness may promote the nucleation of vortices at a surface. For pre-existing vortex lines in the vicinity of the surface, there is also indirect experimental evidence of a ‘vortex mill’ mechanism which continuously feeds vorticity into the flow by stretching the existing vortex lines. This mechanism only works if the spooling vortex, held by pinning sites at the surface, is aligned in the streamwise direction [?].

7.2 Method

To shed light on the microscopic behaviour of superflow near a rough boundary, we work with the three-dimensional profile of a real surface, shown in Fig. 7.1(a). This corresponds to a one square micron region of the surface of a thin NbTi wire used to generate quantum turbulence at Lancaster University, as profiled via atomic force microscopy (AFM) [23]. The surface is rough, with a height up to around 10 nm, and features sharp grooves and steep ridges, likely to have arisen during the etching phase of the wire preparation. We assume that such a ‘mountain’ landscape is typical of the wires and similar objects used across other superfluid turbulence experiments. We model the flow of superfluid helium over this surface through the time-dependent Gross-Pitaevskii equation [?] (GPE) for a weakly-interacting Bose superfluid. The superfluid is parameterised by a complex wavefunction $\Psi(\mathbf{r}, t) = \sqrt{n(\mathbf{r}, t)} \exp[iS(\mathbf{r}, t)]$, where n and S represent density and phase distributions,

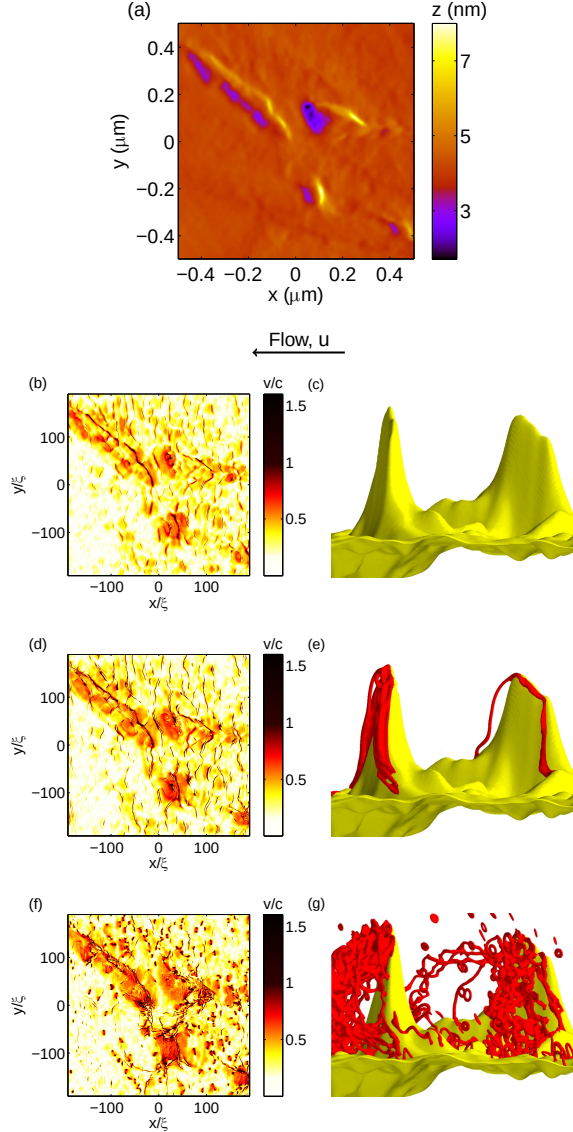


Figure 7.1: (a) AFM image of a section of the NbTi wire used to generate turbulence in superfluid helium at Lancaster University (data provided by R. P. Haley and C. Lawson). The image has been smoothed by Gaussian blur (standard deviation 6 nm). (b, d, f) Magnitude of the fluid speed, $v = |\mathbf{v}|$, shown in the xy -plane and computed just above the surface (where the density drops to $0.1n_0$), at three times. (c, e, g) Zoomed-up density isosurface plots showing the surface (yellow) and vortices (red) in the vicinity of the two tallest mountains (view taken along y over the x -range $15\xi \leq x \leq 125\xi$) at the same times. Just prior to vortex nucleation [plots (b, c), $t = 20\tau$], the largest fluid speed arises in the vicinity of the highest mountains. When the fluid speed becomes supercritical at the highest mountains [plots (d, e), $t = 30\tau$], vortex lines becomes nucleated. At later times [plots (f, g), $t = 100\tau$], vortices continue to be shed predominantly by the highest mountains, where the fluid speed continues to be highest. The nucleation vortex loops pass downstream (to the left of the mountains), filling a turbulent layer up to the height of the highest mountain. This causes a marked downstream spreading of high fluid speed.

and its dynamics obey

$$i\hbar \frac{\partial \Psi}{\partial t} = \left(-\frac{\hbar^2}{2m} \nabla^2 + V(\mathbf{r}, t) + g|\Psi|^2 \right) \Psi. \quad (7.1)$$

where m denotes the particle mass, the coefficient g accounts for local particle interactions, and $V(\mathbf{r}, t)$ describes a potential landscape acting on the fluid. The GPE is equivalent to a hydrodynamic model with fluid density $n(\mathbf{r}, t) = |\psi(\mathbf{r}, t)|^2$ and velocity $\mathbf{v}(\mathbf{r}, t) = (\hbar/m)\nabla S$, and embodies a classical continuity equation and a modified Euler equation (the modification being the presence of a quantum pressure term, arising from zero-point motion of the particles and responsible for vortex nucleation). While the GPE provides only a qualitative model of the strongly-interacting superfluid helium (for example, the excitation spectrum of the GPE lacks helium’s roton minimum), it nevertheless contains the key microscopic physical ingredients of our problem: finite-size vortex core, vortex interactions and vortex reconnections [?]. Furthermore, any boundary, however irregular, can be conveniently modelled through the potential $V(\mathbf{r}, t)$. Within the GPE model and assuming a homogeneous particle density n_0 , the vortex core size is characterised by the healing length $\xi = \hbar/\sqrt{mn_0g}$. The natural speed, energy and time scales are provided by the speed of sound $c = \sqrt{n_0g/m}$, the chemical potential $\mu = n_0g$ and the unit $\tau = \xi/c$, respectively.

The more traditional Vortex Filament Model [?], which has been used to model the motion of vortex lines in the presence of smooth spherical [149, 150], hemispherical [?] and cylindrical boundaries [151?], is less appropriate than the GPE for a number of reasons. Firstly, it assumes that the vortex core is infinitesimal compared to any other length scale (which is not the case if vortex core and wall roughness are comparable); secondly, it does not contain vortex nucleation and kinetic energy losses due to sound emission; thirdly it is difficult to generalise from smooth, geometrically simple (cylindrical or spherical) boundaries to the rough boundaries which interest us.

Our results are based on intensive simulations of the GPE over the entire AFM surface, resolved down to a sub-core scale of $\Delta = 0.4\xi$. In ${}^4\text{He}$ the vortex core size is $a_0 \approx 10^{-10} \text{ m}$ [152], such that the above AFM image has true core dimensions $(10^4 \times 10^4 \times 100)a_0^3$. It is not computationally feasible to model the corresponding range of scales directly within the GPE; as such we map the AFM image onto the largest practical healing length volume of $(400 \times 400 \times 100)\xi^3$. This is simulated in a box of size $(400 \times 400 \times 200)\xi^3$ (the numerical domain being twice as high as the highest mountain in the third dimension), on a $1000 \times 1000 \times 500$ spatial grid, which is periodic in x and y . Time evolution is performed with 4th order Runge-Kutta scheme with time step $\Delta t = 0.01\tau$, and performed across 256 (2.6 GHz) cores of a high-performance computer cluster. The rough surface is incorporated into the GPE by setting a potential barrier $V = 5\mu$ below the surface, heavily prohibiting density there; above the surface the density recovers to the bulk value n_0 (where $V = 0$)

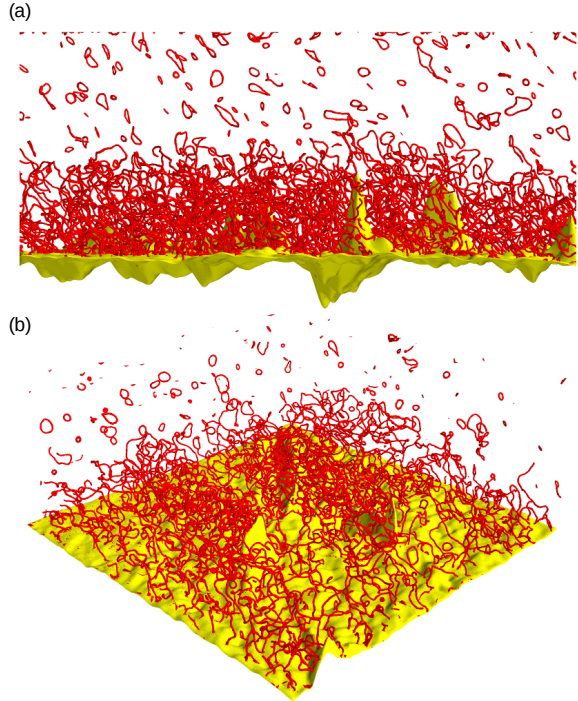


Figure 7.2: Instantaneous isosurfaces of density $n(\mathbf{r}, t)$ (plotted at 25% of the bulk density) for a super-critical flow ($u = 0.6c$) in the saturated turbulent regime reached at long times ($t = 1220\tau$). Notice the turbulent boundary layer up to approximately the height of the highest mountains and the region of small vortex rings above it.

over a lengthscale of the order of ξ .

We first obtain the stationary solution of the GPE in the presence of the rough boundary, with bulk density n_0 . The GPE is then transformed into a frame moving at speed u in the x -direction (corresponding to the imposed flow) by the addition of a Galilean boost term $i\hbar u \partial\Psi/\partial x$ to the right-hand side of the GPE. The flow speed is ramped up smoothly from zero to the final value of $u = 0.6c$; this final value is such that the critical velocity for nucleation is comfortably exceeded.

7.3 Three-dimensional results

In the vicinity of the surface the local fluid speed, $v = |\mathbf{v}|$, is enhanced considerably by the surface's roughness, with the maximum values occurring near the tallest mountain [Fig. 1 (b)]. Up to a critical imposed speed, the flow remains laminar and free of vortices. For increased imposed flow velocity, the critical velocity is first exceeded at the highest mountain, leading to nucleation of a vortex line [Fig. 1 (e)], and then by other high mountains on the surface. The critical velocity for vortex nucleation across this surface occurs for an imposed flow $u_c \approx 0.2c$; this is considerably smaller than, say a hemispherical bump for

which $u_c \approx 0.5c$ [?], indicating the significant role of the surface roughness in enhancing the breakdown of laminar flow.

Nucleated vortices either peel off the boundary, or, more frequently, slide down the slopes of the mountains (carried by the imposed flow) in the form of partially attached vortex loops. Such loops then interact with other vortices, becoming more distorted, and forming a tangle of vortices downstream of the mountains [Fig. 1(g)]. This tangle of vortices is continuously fed by further vortices nucleated from the mountains. The spreading of the velocity plots in Figs. 7.1 (b, c) reveals the formation of clusters of vortices on the leeward side of the mountains, which eventually saturate a turbulent layer. Vortex lines occasionally undergo vortex reconnections, or twist, detach and fly off as small vortex rings. At later times and higher imposed flow velocities, the critical velocity is exceeded across greater areas of the surface. However, even after considerable vortex nucleation, the highest mountains continue to dominate the vortex nucleation - here the fluid velocity is always the highest [Fig. 1(f)] and vortex shedding occurs at the fastest rate. This confirms that, with our choice of parameters, the vortex tangle which develops can be interpreted as generated either intrinsically or extrinsically: in both cases vortices nucleate at the highest mountains before filling the layer below. Indeed, Fig. 1(g) shows the formation of a long curved vortex which becomes twisted generating more vorticity by spooling smaller vortex loops, as in the vortex-mill mechanism envisaged by Schwarz [?].

As the number of vortices increases, a complex, turbulent region consisting of superfluid vortex loops and rings is formed [Fig. 2 (a,b)]. This is strongly localised to the vicinity of the surface, up to approximately the height of the highest mountain. Reconnections due to twisting of vortex lines or interaction of neighbouring lines form a continuous ejection of vortex rings which spread into the bulk, visible in the upper part of Fig. 2(a, b). The vortex length in the vicinity of the boundary, which has so far been increasing, approximately saturates in value. A supplementary movie [?] shows the full evolution of the turbulent layer. For slower, but still super-critical, imposed flows the turbulent layer still forms with the same height, albeit with reduced density of vortices.

The turbulent layer is not isotropic: on the average, vortex lines are flattened parallel to plane of the surface (the areas covered by vortex cores on the lines of sight along the x and y directions are only 62 and 60% respectively of the same area along the z direction).

7.4 Two-dimensional results

We find the critical velocity for vortex nucleation to be $v_c = (0.125 \pm 0.025)c$. We focus on an arbitrary super-critical flow speed of $v = 0.35c$, with Fig. 7.3 depicting the evolution of the system. For clarity we show both the condensate density (upper plots) and vortex locations/circulation (lower plots). At early times, a series of positive-circulation vortices

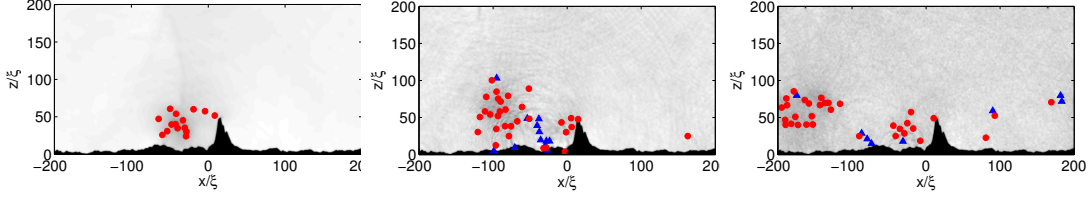


Figure 7.3: Evolution of 2D flow past the rough surface for a flow speed of $v = 0.35c$. Depicted are snapshots of density and vortex locations at times (from left to right) $t = 500, 1580$, and 2100τ . Red (blue) circles represent vortices of positive (negative) circulation.

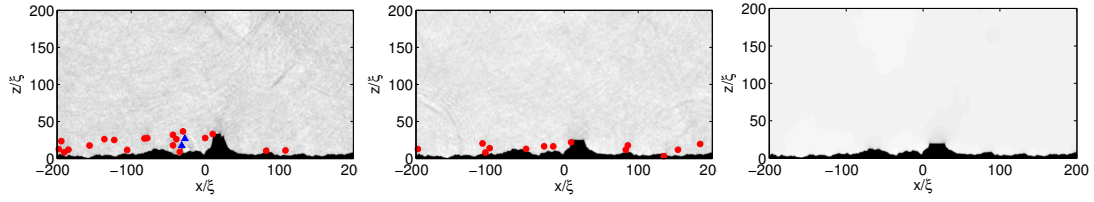


Figure 7.4: Same-time snapshots for various levels of surface truncation: (i) $\beta = 70\%$, (ii) $\beta = 50\%$ and (iii) $\beta = 40\%$, where β represents the truncation height relative to the highest point in the surface. Depicted are snapshots of density and vortex locations. For comparison, the untruncated surface ($\beta = 100\%$) is depicted in Fig. 7.3. The flow speed is $v = 0.35c$ and the time is $t = 2440\tau$.

(red) peel off from the peak of the large mountain. Vortices are nucleated here, and not elsewhere, due to the high curvature in the surface at this peak, which induces a relatively high local fluid velocity. As they are carried downstream the vortices stay in close proximity and co-rotate about one another; this leads to the vortices combining into a larger-scale cluster of positive circulation. This cluster travels downstream just above the surface. Close to the surface, the cluster introduces a large relative fluid flow in the positive- x direction. This interrupts the nucleation of vortices from the mountain top and also induces the secondary generation of vortices (blue) from smaller-scale surface prominences. These secondary vortices are of negative circulation and also form a vortex cluster. As this cluster grows, it leads to a cessation of secondary vortex production, and so again the primary vortices become nucleated from the mountain peak. This process repeats.

The total number of vortices N_v increases with time (Fig. 7.5(a), solid line); initially this increase is rapid but over time it slows down as the number of vortices within the finite-sized box begins to saturate. Initially this is almost entirely composed of positively-signed vortices (dashed line), apart from a small amount of spurious negative-sign vortices (dotted line). At $t \approx 700\tau$ the number of positive-sign vortices increases sharply; this represents the formation of secondary vortices.

It is important to note that the generation of secondary clusters requires the surface to be rough downstream of the mountain. If the surface is perfectly smooth downstream of the mountain, the positive-signed vortices persist.

Note also that it is possible for tertiary vortices/clusters of positive-sign; these arise

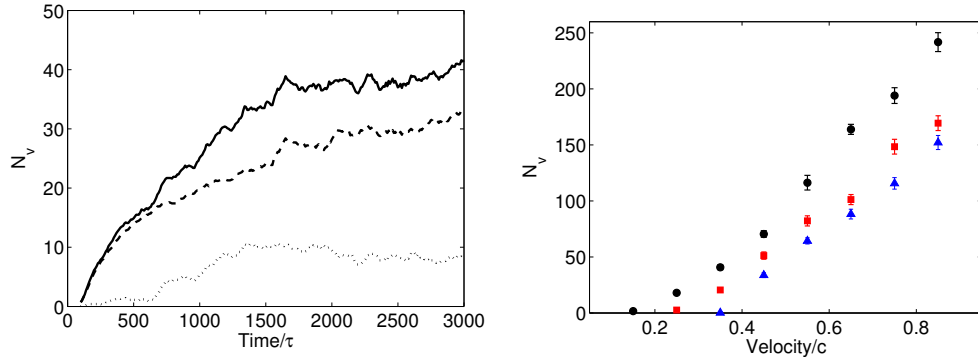


Figure 7.5: (a) Number of vortices produced during $v = 0.35c$ flow past the surface. Shown are the numbers of total vortices N_v (solid line), positive vortices (dashed line) and negative vortices (dotted line). (b) Final number of vortices N_v as a function of the flow velocity v for the 2d simulations. Each data point represents the average of 20 measurements of N_v in the vicinity of $t = 3000\tau$.

when the secondary cluster induces a sufficiently high flow speed in the negative- x direction to generate vortices from the local surface roughness.

7.4.1 Truncated surfaces

It is evident above that the vortex generation is dominated by the large single prominence in the surface, with the smaller prominences having only a secondary effect. To further analyse this we next study how the flow is affected by truncation of the surface height, $z = h(x, y)$, to a percentage β of the maximum height h_0 , i.e. $h(x, y) \rightarrow h(x, y)H(z/h_0 = \beta)$, where $H(z)$ is the Heaviside step function ($\beta = 100\%$ corresponds to no truncation, $\beta = 0$ corresponds to complete truncation).

Figure 7.4 shows a snapshot (at fixed time) for various levels of truncation β , with all cases having the same flow speed $v = 0.35c$. It is evident that the height of the mountain plays a critical role. Already, when the mountain is capped at 70%, the number of vortices produced by that time is vastly reduced. The vortices are generated at a sufficiently low frequency that only small clusters form; secondary vortices are still formed but in a much lower quantity. For $\beta = 50\%$ even fewer vortices are produced, and for this case no clustering takes place and in turn no secondary vortices are formed. For $\beta = 40\%$ no vortices are generated at all.

7.5 Conclusions

In conclusion, our results suggest that the walls of channels which confine the flow of superfluid liquid helium and the surfaces of moving objects (wires, grids, propellers, spheres) which are used to generate superfluid turbulence in current experiments may be covered by a thin ‘superfluid boundary layer’ consisting of vortex loops and rings. This is a surpris-

ing effect, because in fluid dynamics boundary layers usually arise from viscous forces, which in superfluid liquid helium near the temperature of absolute zero are completely absent. These findings further illustrate the deep analogies between classical and quantum fluids. The experimental implications of ‘superfluid boundary layers’ on macroscopic observables need to be investigated. Our results should particularly stimulate experiments in ${}^3\text{He-B}$, where, due to relative large healing length, it is possible to study flows with controlled surface height roughness.

Part III

Appendix

Appendix A

Detailed Derivations

A.1 Derivation of the Runge-Kutta scheme

Presented here is the derivation of the explicit second order Runge-Kutta scheme. The ideas and methods easily extend to the forth order scheme used in this thesis, but in the interests of brevity the entire proof will be given to second order, with the relevant forth order extensions clearly noted. Let an initial value problem be specified as

$$\psi'(t) = f(\psi(t), t), \quad \psi(t_0) = \psi_0,$$

where $t_n = nh$, h is a chosen step size, and $f(\psi(t), t)$ is known. The aim of the scheme is to estimate some $\psi(t_m)$ from the known $\psi(t_0)$ through the application of a single numerical step of size h , m times.

For a single application of the numerical step we attempt to find the unknown value of $\psi(t_{n+1})$, which can be written,

$$\begin{aligned} \psi(t_{n+1}) &= \psi(t_n) + [\psi(t_{n+1}) - \psi(t_n)] \\ &= \psi(t_n) + \int_{t_n}^{t_{n+1}} f(\psi(\tau), \tau) d\tau. \end{aligned}$$

We now decide to approximate the (difficult to calculate) integral $\int_{t_n}^{t_{n+1}} f(\psi(\tau), \tau) d\tau$ using quadrature, leading to the modified expression,

$$\psi(t_{n+1}) \approx \psi(t_n) + h \sum_{i=1}^N \omega_i f(t_n + h\nu_i, \psi(t_n + h\nu_i)),$$

where N is the order of the numerical scheme, ω_i are weights and ν_i are locations in time positioned between t_n and t_{n+1} inclusive. In this second-order derivation we take $N = 2$,

a forth order scheme would alternatively require $N = 4$.

We take the first temporal point to be $v_1 = 0$, so that the first term in the sum is

$$k_1 = hf(t_n, \psi(t_n)).$$

We can then easily calculate the value of k_1 . A single step in Euler's method tells us that $\psi(t_n + hv_2) \approx hv_2 f(t_n, \psi(t_n))$ and so we write k_2 in a form containing k_1 ,

$$k_2 = hf(t_n + hv_2, \psi(t_n + hv_2)) \approx hf(t_n + v_2 h, \psi(t) + v_2 k_1).$$

For a forth order scheme we would then introduce k_3 and k_4 , following the same methods of writing k_i in previous terms up to k_{i-1} . To second order, the quadrature formula becomes

$$\psi(t_{n+1}) \approx \psi(t_n) + \omega_1 k_1 + \omega_2 k_2. \quad (\text{A.1})$$

However, note that we still must derive values for the quantities $v_{i>1}$ and ω_i .

Consider the Taylor expansion,

$$\psi(t+h) = \psi(t) + h\psi'(t) + \frac{h^2}{2}\psi''(t) + \dots,$$

where for the full forth order derivation, further higher order terms are also considered. We substitute this expansion into the left hand side of Equation A.1, which leads to

$$\psi(t_n) + h\psi'(t_n) + \frac{h^2}{2!}\psi''(t_n) + O(h^3) \approx \psi(t_n) + \omega_1 k_1 + \omega_2 k_2. \quad (\text{A.2})$$

Note that

$$\begin{aligned} \psi'(t_n) &= f, \\ \psi''(t_n) &= \frac{\partial f}{\partial t} + f \frac{\partial f}{\partial \psi}, \end{aligned}$$

by the definition of $\psi'(t)$ and the total derivative, and where the arguments of $f(t_n, \psi(t_n))$ have been suppressed for notational ease. We then substitute the expressions for $\psi'(t_n)$, $\psi''(t_n)$, k_1 and k_2 into Equation A.1,

$$hf + \frac{h^2}{2} \left(\frac{\partial f}{\partial t} + f \frac{\partial f}{\partial \psi} \right) + O(h^3) = \omega_1 hf + \omega_2 hf(t_n + v_2 h, \psi(t) + v_2 k_1). \quad (\text{A.3})$$

Now consider the the Taylor expansion,

$$f(t+h, \psi+g) = f(t, \psi) + h \frac{\partial f(t, \psi)}{\partial t} + g \frac{\partial f(t, \psi)}{\partial \psi} + \dots,$$

where for the full forth order derivation, further higher order terms are also considered. We substitute this expansion into equation A.1, including terms up to the required order, and find

$$hf + \frac{h^2}{2!} \left(\frac{\partial f}{\partial t} + f \frac{\partial f}{\partial \psi} \right) + O(h^3) = \omega_1 hf + \omega_2 \left(hf + v_2 h^2 \frac{\partial f}{\partial t} + v_2 h^2 f \frac{\partial f}{\partial \psi} \right) + O(h^3). \quad (\text{A.4})$$

By equating terms on both the right hand side and left hand side of Equation A.1, we find that for the second order Runge-Kutta scheme the following equivalences are required for consistency,

$$\begin{aligned} \omega_1 + \omega_2 &= 1, \\ v_2 \omega_2 &= \frac{1}{2}. \end{aligned}$$

For the forth order scheme, more but similar equivalences are required for consistency. The canonical choice for the second order Runge-Kutta methods is $v_2 = 1$ and $\omega_1 = \omega_2 = 1/2$. The scheme can then be directly written down,

$$\psi(t_{n+1}) = \psi(t_n) + \frac{k_1}{2} + \frac{k_2}{2} + O(h^3), \quad (\text{A.5})$$

where $k_1 = hf(t_n, \psi(t_n))$ and $k_2 = hf(t_n + h, \psi(t_n) + k_1)$.

When this proof outline is followed with $N = 4$, the forth order Runge-Kutta scheme can be found,

$$\psi(t_{n+1}) = \psi(t_n) + \frac{k_1}{6} + \frac{k_2}{3} + \frac{k_3}{3} + \frac{k_4}{6} + O(h^5), \quad (\text{A.6})$$

where

$$\begin{aligned} k_1 &= hf(t_n, \psi(t_n)), \\ k_2 &= hf\left(t_n + \frac{h}{2}, \psi(t_n) + \frac{k_1}{2}\right), \\ k_3 &= hf\left(t_n + \frac{h}{2}, \psi(t_n) + \frac{k_2}{2}\right), \\ k_4 &= hf(t_n + h, \psi(t_n) + k_3). \end{aligned}$$

A.2 Derivation of the Gross-Pitaevskii Equation

This section derives the GPE following the methodology outlined in [153]. We begin by revisiting the quantum field theory formalism used to describe a many body quantum system [154]. Such a system is described by an N-body wavefunction, $\tilde{\Psi}(\mathbf{r}_1 \dots \mathbf{r}_N, t)$ which obeys the famous Schrödinger equation

$$i\hbar \frac{\partial}{\partial t} \tilde{\Psi}(\mathbf{r}_1 \dots \mathbf{r}_N, t) = \hat{H} \tilde{\Psi}(\mathbf{r}_1 \dots \mathbf{r}_N, t), \quad (\text{A.7})$$

where \mathbf{r}_i describes the coordinates of the i th body. Consider a closed system containing a dilute, weakly interacting Bose gas of N atoms. Such a system would be described by $\tilde{\Psi}(\mathbf{r}_1 \dots \mathbf{r}_N, t)$, with a Hamiltonian of the form

$$\hat{H} = \sum_{k=1}^N \hat{h}_0(\mathbf{r}_k, t) + \frac{1}{2} \sum_{k,l=1}^N \hat{V}(\mathbf{r}_k, \mathbf{r}_l). \quad (\text{A.8})$$

Here $\hat{h}_0(\mathbf{r}, t) = -\frac{\hbar^2}{2m} \nabla^2 + V_{\text{ext}}(\mathbf{r}, t)$ is a contribution arising from the effects of a single particle in an external potential. We assume in the dilute gas all interactions are binary; and so the second term arises from collisions between 2 atoms. The factor of $\frac{1}{2}$ ensures the effects are only counted once over the entire sum.

We now reformulate this system in a different representation, using the so called ‘occupation number’ orthonormal basis $|n_1 \dots n_\infty\rangle$. This basis arises from the observation that multiple particles sharing an energetically accessible state are indistinguishable. Instead we consider only the number of particles in each state i and denote this n_i . Such states often correspond to states with fixed energy ε_i . While the number of states are infinite, our system contains a fixed number of bosons, N , implying that there are at most N states occupied.

The wavefunction is mapped into the ‘occupation number’ basis via

$$\tilde{\Psi}(\mathbf{r}_1 \dots \mathbf{r}_N, t) \rightarrow |\tilde{\Psi}(t)\rangle = \sum_{n_1 \dots n_\infty} c(n_1 \dots n_\infty, t) |n_1 \dots n_\infty\rangle,$$

with appropriately chosen complex coefficients, $c(n_1 \dots n_\infty, t)$. The values c must follow the particle statistics rules (e.g. for Bosons much be symmetric under swapping of quantum numbers) and be normalised so that the probabilities correctly sum to one. We find that for our bosons,

$$\int |\tilde{\Psi}|^2 d\mathbf{r} = 1 \Rightarrow \sum_{n_1 \dots n_\infty} |c(n_1 \dots n_\infty, t)|^2 \frac{N!}{n_1! \dots n_\infty!} = 1.$$

In this formulation, note that the state vectors $|n_1 \dots n_\infty\rangle$ are time-independent, and the

evolution of the system is entirely encoded in the values of $c(n_1 \dots n_\infty, t)$. As part of the overall picture, we also must describe the movement of bosons between different states or energy levels. It is convenient to visualise this as the simultaneous destruction of a particle in state j and creation of a particle in state i , described mathematically using the single particle annihilation and creation operators[Shiff49].

$$\hat{a}_j |n_1 \dots n_i \dots n_j \dots n_\infty\rangle = \sqrt{n_j} |n_1 \dots n_i \dots n_j - 1 \dots n_\infty\rangle,$$

$$\hat{a}_i^\dagger |n_1 \dots n_i \dots n_j \dots n_\infty\rangle = \sqrt{n_i + 1} |n_1 \dots n_i + 1 \dots n_j \dots n_\infty\rangle,$$

which satisfy the bosonic commutation relations,

$$[\hat{a}_i, \hat{a}_j^\dagger] = \delta_{ij} \quad [\hat{a}_i, \hat{a}_j] = [\hat{a}_i^\dagger, \hat{a}_j^\dagger] = 0.$$

Any single particle changing states can now be described through these operators; a particle moving from state j to state i is described using a single annihilation operator and a single creation operator through the product $\hat{a}_i^\dagger \hat{a}_j$. Similarly, as we decided to simplify the system by considering a dilute gas where all interactions are binary collisions, all interactions can be described by two particles changing state, using the product $\hat{a}_i^\dagger \hat{a}_k^\dagger \hat{a}_j \hat{a}_l$. Using these tools and ideas, the original description in Equations A.7 and A.8 is now written

$$i\hbar \frac{\partial}{\partial t} |\tilde{\Psi}\rangle = \hat{H} |\tilde{\Psi}\rangle,$$

with the Hamiltonian

$$\hat{H} = \sum_{ij} \langle i | \hat{h}_0 | j \rangle \hat{a}_i^\dagger \hat{a}_j + \frac{1}{2} \sum_{ijkl} \langle ik | \hat{V} | jl \rangle \hat{a}_i^\dagger \hat{a}_k^\dagger \hat{a}_j \hat{a}_l, \quad (\text{A.9})$$

where

$$\langle i | \hat{h}_0 | j \rangle = \int \phi_i^*(\mathbf{r}) \hat{h}_0 \phi_j(\mathbf{r}) d\mathbf{r},$$

$$\langle ik | \hat{V} | jl \rangle = \frac{1}{2} [(ik | \hat{V} | jl) + (ik | \hat{V} | lj)],$$

$$(ik | \hat{V} | jl) = \iint \phi_i^*(\mathbf{r}) \phi_k^*(\mathbf{r}') \hat{V}(\mathbf{r} - \mathbf{r}') \phi_l(\mathbf{r}') \phi_j(\mathbf{r}) d\mathbf{r}' d\mathbf{r}.$$

For further convenience we introduce the so called Bose field operators

$$\hat{\Psi}(\mathbf{r}, t) = \sum_i \hat{a}_i(t) \phi_i(\mathbf{r}, t),$$

$$\hat{\Psi}^\dagger(\mathbf{r}, t) = \sum_i \hat{a}_i^\dagger(t) \phi_i(\mathbf{r}, t),$$

which can be thought of as operators that represent the addition or removal of a particle at time t and location \mathbf{r} . As with the annihilation and creation operators, the Bose field operators also satisfy the commutation relations,

$$[\hat{\Psi}(\mathbf{r}, t), \hat{\Psi}^\dagger(\mathbf{r}', t)] = \delta(\mathbf{r} - \mathbf{r}') \quad [\hat{\Psi}(\mathbf{r}, t), \hat{\Psi}(\mathbf{r}', t)] = [\hat{\Psi}^\dagger(\mathbf{r}, t), \hat{\Psi}^\dagger(\mathbf{r}', t)] = 0. \quad (\text{A.10})$$

Using these operators, the Hamiltonian in Equation A.9 can be again rewritten as

$$\begin{aligned} \hat{H} &= \int \hat{\Psi}^\dagger(\mathbf{r}, t) \hat{h}_0 \hat{\Psi}(\mathbf{r}, t) d\mathbf{r} \\ &\quad + \frac{1}{2} \iint \hat{\Psi}^\dagger(\mathbf{r}, t) \hat{\Psi}^\dagger(\mathbf{r}', t) V(\mathbf{r} - \mathbf{r}') \hat{\Psi}(\mathbf{r}', t) \hat{\Psi}(\mathbf{r}, t) d\mathbf{r}' d\mathbf{r}. \end{aligned} \quad (\text{A.11})$$

where, as before, $\hat{h}_0(\mathbf{r}_k, t) = -\frac{\hbar^2}{2m} \nabla^2 + V_{\text{ext}}(\mathbf{r}, t)$ and $V(\mathbf{r} - \mathbf{r}')$ is the two body interaction potential.

We now add to our approximations a frequent simplification of the interaction potential and consider all interactions as totally elastic contact collisions. The strength of this interaction is usually taken to be $g = 4\pi\hbar^2 a/m$, where a is the s-wave scattering length, measured for a particular atom in the lab. Our two body interaction potential then becomes,

$$V(\mathbf{r} - \mathbf{r}') = g\delta(\mathbf{r} - \mathbf{r}'),$$

which when inserted into Equation A.11 gives the Hamiltonian,

$$\hat{H} = \int \hat{\Psi}^\dagger(\mathbf{r}, t) \hat{h}_0 \hat{\Psi}(\mathbf{r}, t) d\mathbf{r} + \frac{g}{2} \int \hat{\Psi}^\dagger(\mathbf{r}, t) \hat{\Psi}^\dagger(\mathbf{r}', t) \hat{\Psi}(\mathbf{r}', t) \hat{\Psi}(\mathbf{r}, t) d\mathbf{r}.$$

The Bose field operator $\hat{\Psi}(\mathbf{r}, t)$ evolves over time according to the Heisenberg equation of motion

$$i\hbar \frac{\partial}{\partial t} \hat{\Psi}(\mathbf{r}, t) = [\hat{\Psi}(\mathbf{r}, t), \hat{H}].$$

By expanding out the commutator, using standard commutator identities along with the relations in Equation A.10 and integrating out resulting delta functions we find

$$\begin{aligned} i\hbar \frac{\partial}{\partial t} \hat{\Psi}(\mathbf{r}, t) &= \int [\hat{\Psi}, \hat{\Psi}^\dagger \hat{h}_0 \hat{\Psi}] d\mathbf{r} + \frac{g}{2} \int [\hat{\Psi}, \hat{\Psi}^\dagger \hat{\Psi}^\dagger \hat{\Psi} \hat{\Psi}] d\mathbf{r} \\ &= \int [\hat{\Psi}, \hat{\Psi}^\dagger] \hat{h}_0 \hat{\Psi} + \hat{\Psi}^\dagger [\hat{\Psi}, \hat{h}_0 \hat{\Psi}] d\mathbf{r} \\ &\quad + \frac{g}{2} \int [\hat{\Psi}, \hat{\Psi}^\dagger] \hat{\Psi}^\dagger \hat{\Psi} \hat{\Psi} + \hat{\Psi}^\dagger [\hat{\Psi}, \hat{\Psi}^\dagger] \hat{\Psi} \hat{\Psi} + \hat{\Psi}^\dagger \hat{\Psi}^\dagger [\hat{\Psi}, \hat{\Psi} \hat{\Psi}] d\mathbf{r} \\ &= \hat{h}_0 \hat{\Psi}(\mathbf{r}, t) + g \hat{\Psi}^\dagger(\mathbf{r}, t) \hat{\Psi}(\mathbf{r}, t) \hat{\Psi}(\mathbf{r}, t). \end{aligned} \quad (\text{A.12})$$

We can continue to simplify the equation of motion by considering a mean-field approach

for a single macroscopically occupied state. In the case of Bose-Einstein condensation the lowest energy level is macroscopically occupied and so we decompose the field operator via

$$\hat{\Psi}(\mathbf{r}, t) = \hat{\psi}(\mathbf{r}, t) + \hat{\delta}(\mathbf{r}, t),$$

where $\psi(\mathbf{r}, t)$ is a field operator for the condensate and $\hat{\delta}(\mathbf{r}, t)$ is a field operator for the non-condensed atoms, whether that be atoms in higher states, atoms residing in the thermal cloud, or atoms influenced by quantum mechanical fluctuations.

We now make the Bogoliubov approximation [155], a somewhat violent symmetry breaking approximation in which the condensate field operator is replaced by a classical field,

$$\hat{\psi}(\mathbf{r}, t) = \psi(\mathbf{r}, t) = \sqrt{N_0} \phi_0(\mathbf{r}, t),$$

where N_0 is the number of particles in the condensate. Written in this way, it is then possible to approximate the condensate density using $n(\mathbf{r}, t) = |\psi(\mathbf{r}, t)|^2$. Unfortunately a direct consequence of the action is that the physical state described by $\hat{\Psi}(\mathbf{r}, t)$ no longer satisfies the same symmetries as before. In particular, the total number of particles is not conserved. This approximation is justified by the understanding that as the condensate forms, it takes on a single phase, and all the particles in the condensate can be described by a single wavefunction. In addition, it is assumed that if there are many particles in the condensate, the exact value of N_0 does not affect the system state significantly, that is, $N_0 \approx N_0 + 1$. This approximation is essentially equivalent to the statement $\langle \hat{\Psi}(\mathbf{r}, t) \rangle = \psi(\mathbf{r}, t) \neq 0$, where $\langle \dots \rangle$ denotes the ensemble average. The non-condensed field operator $\hat{\delta}(\mathbf{r}, t)$ remains as an operator in the decomposition, and captures all the fluctuations around $\psi(\mathbf{r}, t)$. It is generally assumed that $\langle \hat{\delta}(\mathbf{r}, t) \rangle = 0$.

In principle, the classical field $\psi(\mathbf{r}, t)$ is interpreted as the condensed atoms, however it can also be interpreted as the condensate atoms along with excitations of the system, as long as the occupation at high energy states $n_i \gg 1$ and the size of quantum fluctuations are both negligible. The classical field, or c-field, approaches can be used to model finite temperature effects by modelling part of the thermal cloud with highly populated modes below a certain momentum cutoff, explored in Section 2.9.

In the limit of $T \rightarrow 0$, all of the particles become part of the condensate, so that $N = N_0$. The contribution from the non-condensate atoms can be neglected, $\hat{\delta}(\mathbf{r}, t) = 0$, and the field operator is written $\hat{\Psi}(\mathbf{r}, t) = \psi(\mathbf{r}, t)$. In this case, the Heisenberg equation of motion in Equation A.12 reduces to

$$\begin{aligned} i\hbar \frac{\partial}{\partial t} \psi(\mathbf{r}, t) &= \hat{h}_0 \psi(\mathbf{r}, t) + g \psi^*(\mathbf{r}, t) \psi(\mathbf{r}, t) \psi(\mathbf{r}, t) \\ &= \left(-\frac{\hbar^2}{2m} \nabla^2 + V_{\text{ext}}(\mathbf{r}, t) + g |\psi(\mathbf{r}, t)|^2 \right) \psi(\mathbf{r}, t), \end{aligned}$$

the so called Gross-Pitaevskii equation (GPE), also known as the non-linear Schrödinger equation.

Finally, note that as the particle number is no longer strictly conserved, calculations should be performed within the grand canonical ensemble [156]. This approach leads to the modified Hamiltonian $\hat{H} \rightarrow \hat{H} - \mu \hat{N}$, where μ is the chemical potential and \hat{N} is the total number operator. The above derivations can be easily repeated with the modified Hamiltonian to obtain a physically equivalent version of the GPE with a chemical potential term,

$$i\hbar \frac{\partial}{\partial t} \psi(\mathbf{r}, t) = \left(-\frac{\hbar^2}{2m} \nabla^2 + V_{\text{ext}}(\mathbf{r}, t) + g|\psi(\mathbf{r}, t)|^2 - \mu \right) \psi(\mathbf{r}, t). \quad (\text{A.13})$$

A.3 Derivation of the Hydrodynamic Equations via the Madelung Transformation

Inserting the Madelung transformation (Section 2.11) into the GPE and writing the result in tensor notation yields

$$i\hbar \left(\frac{\partial R}{\partial t} + i \frac{\partial \theta}{\partial t} R \right) e^{i\theta} = -\frac{\hbar^2}{2m} e^{i\theta} \left(\frac{\partial^2 R}{\partial x_j^2} + 2i \frac{\partial \theta}{\partial x_j} \frac{\partial R}{\partial x_j} + i \frac{\partial^2 \theta}{\partial x_j^2} R - \frac{\partial \theta}{\partial x_j} \frac{\partial \theta}{\partial x_j} R \right) + gR^3 e^{i\theta} + VR e^{i\theta}.$$

The real and imaginary parts of the GPE, once divided by $\exp(i\theta)$, then take the form

$$-\hbar R \frac{\partial \theta}{\partial t} = -\frac{\hbar^2}{2m} \left(\frac{\partial^2 R}{\partial x_j \partial x_j} - R \frac{\partial \theta}{\partial x_j} \frac{\partial \theta}{\partial x_j} \right) + gR^3 + VR, \quad (\text{A.14})$$

$$\hbar \frac{\partial R}{\partial t} = -\frac{\hbar^2}{2m} \left(2 \frac{\partial \theta}{\partial x_j} \frac{\partial R}{\partial x_j} + R \frac{\partial^2 \theta}{\partial x_j \partial x_j} \right). \quad (\text{A.15})$$

Consider Equation (A.15) and note that $\rho = mR^2 \Rightarrow \frac{\partial \rho}{\partial t} = 2mR \frac{\partial R}{\partial t}$, allowing us to rewrite the equation in terms of ρ ,

$$\begin{aligned} \frac{\partial \rho}{\partial t} &= -\hbar R \left(2 \frac{\partial \theta}{\partial x_j} \frac{\partial R}{\partial x_j} + R \frac{\partial^2 \theta}{\partial x_j \partial x_j} \right) \\ &= -2mR \frac{\partial R}{\partial x_j} \frac{\partial}{\partial x_j} \left(\frac{\hbar}{m} \theta \right) - mR^2 \frac{\partial^2}{\partial x_j \partial x_j} \left(\frac{\hbar}{m} \theta \right) \\ &= -\frac{\partial \rho}{\partial x_j} \frac{\partial}{\partial x_j} \left(\frac{\hbar}{m} \theta \right) - \rho \frac{\partial^2}{\partial x_j \partial x_j} \left(\frac{\hbar}{m} \theta \right). \end{aligned}$$

The terms containing the phase can then be directly replaced with the fluid velocity, $v_j = \frac{\partial}{\partial x_j} \left(\frac{\hbar}{m} \theta \right)$.

$$\begin{aligned}\frac{\partial \rho}{\partial t} &= -\frac{\partial \rho}{\partial x_j} v_j - \rho \frac{\partial}{\partial x_j} v_j \\ &= -\frac{\partial}{\partial x_j} (\rho v_j).\end{aligned}$$

Rewritten in vector form the result is a continuity equation,

$$\frac{\partial \rho}{\partial t} + \nabla(\rho \mathbf{v}) = 0. \quad (\text{A.16})$$

Now consider Equation (A.14), written in the form

$$\frac{\hbar}{m} \frac{\partial \theta}{\partial t} = \frac{\hbar^2}{2m^2} \left(\frac{1}{R} \frac{\partial^2 R}{\partial x_j \partial x_j} - \frac{\partial \theta}{\partial x_j} \frac{\partial \theta}{\partial x_j} \right) - \frac{gR^2}{m} - \frac{V}{m}.$$

Note that it can easily be shown $\frac{1}{R} \frac{\partial^2 R}{\partial x_j \partial x_j} = \frac{1}{\sqrt{\rho}} \nabla^2 \sqrt{\rho}$ and $\frac{\hbar^2}{2m^2} \frac{\partial \theta}{\partial x_j} \frac{\partial \theta}{\partial x_j} = \frac{v^2}{2}$. It follows that Equation (A.14) can be written,

$$\begin{aligned}\frac{\hbar}{m} \frac{\partial \theta}{\partial t} &= \frac{\hbar^2}{2m^2} \frac{1}{\sqrt{\rho}} \nabla^2 \sqrt{\rho} - \frac{v^2}{2} - \frac{gR^2}{m} - \frac{V}{m} \\ \Rightarrow \frac{\partial}{\partial t} \left(\frac{\hbar}{m} \frac{\partial \theta}{\partial x_k} \right) &= \frac{\partial}{\partial x_k} \left(\frac{\hbar^2}{2m^2} \frac{1}{\sqrt{\rho}} \nabla^2 \sqrt{\rho} \right) - \frac{\partial}{\partial x_k} \left(\frac{v^2}{2} \right) - \frac{2gR}{m} \frac{\partial R}{\partial x_k} - \frac{1}{m} \frac{\partial V}{\partial x_k} \\ \Rightarrow \rho \frac{\partial v_k}{\partial t} &= \rho \frac{\partial}{\partial x_k} \left(\frac{\hbar^2}{2m^2} \frac{1}{\sqrt{\rho}} \nabla^2 \sqrt{\rho} \right) - \rho \frac{\partial}{\partial x_k} \left(\frac{v^2}{2} \right) - 2gR^3 \frac{\partial R}{\partial x_k} - \rho \frac{1}{m} \frac{\partial V}{\partial x_k}.\end{aligned}$$

By noticing that $p = \frac{1}{2} g \left(\frac{\rho}{m} \right)^2 = \frac{gR^4}{2}$ we can write $\frac{\partial p}{\partial x_k} = 2gR^3 \frac{\partial R}{\partial x_k}$ and then,

$$\rho \frac{\partial v_k}{\partial t} + \rho \frac{\partial}{\partial x_k} \left(\frac{v^2}{2} \right) = \rho \frac{\partial}{\partial x_k} \left(\frac{\hbar^2}{2m^2} \frac{1}{\sqrt{\rho}} \nabla^2 \sqrt{\rho} \right) - \frac{\partial p}{\partial x_k} - mR^2 \frac{\partial}{\partial x_k} \left(\frac{V}{m} \right).$$

We now now use the following two results,

$$\begin{aligned}v_j \frac{\partial}{\partial x_j} v_k &= \frac{\partial}{\partial x_k} \left(\frac{v_j v_k}{2} \right) \\ 2 \frac{\partial}{\partial x_k} \left(\frac{1}{\sqrt{\rho}} \frac{\partial^2}{\partial x_j \partial x_j} \sqrt{\rho} \right) &= \frac{1}{\rho} \frac{\partial}{\partial x_j} \rho \frac{\partial}{\partial x_j} \frac{\partial}{\partial x_k} \ln \rho,\end{aligned}$$

and find,

$$\rho \left(\frac{\partial}{\partial t} v_k v_j \frac{\partial v_k}{\partial x_j} \right) = -\frac{\partial p}{\partial x_k} - \frac{\partial}{\partial x_j} P_{jk} - \rho \frac{\partial}{\partial x_k} \left(\frac{V}{m} \right),$$

where $P_{jk} = -\frac{\hbar^2}{4m^2}\rho \frac{\partial^2 \ln \rho}{\partial x_j \partial x_k}$. Writing this in vector notation, we obtain an equation similar to the Euler equation for an inviscid fluid,

$$\rho \left(\frac{\partial \mathbf{v}}{\partial t} + (\mathbf{v} \cdot \nabla) \mathbf{v} \right) = -\nabla p - \nabla \mathbf{P} - \rho \nabla \left(\frac{V}{m} \right). \quad (\text{A.17})$$

Appendix B

Important Quantities

B.1 Energy

The energy functional of the GPE is written

$$\varepsilon(\Psi) = \frac{\hbar}{2m} |\nabla\Psi|^2 + \frac{g}{2} |\Psi|^4 + V|\Psi|^2 - \mu|\Psi|^2, \quad (\text{B.1})$$

where the first term is the kinetic energy, the second term is the energy arising from atom-atom interactions, and the final two terms are the energy associated with the external and chemical potentials. This functional can be integrated over space to find a value for the condensate energy,

$$E = \int \varepsilon(\Psi) \, d\mathbf{r} \quad (\text{B.2})$$

Alternatively, the energy of the system can be defined as a sum of the contributions from various types of energy in the system,

$$E = E_{\text{kin}} + E_{\text{int}} + E_{\text{pot}}, \quad (\text{B.3})$$

so that,

$$E_{\text{kin}} = \int \frac{\hbar}{2m} |\nabla\Psi|^2 \, d\mathbf{r}, \quad E_{\text{int}} = \int \frac{g}{2} |\Psi|^4 \, d\mathbf{r}, \quad E_{\text{pot}} = \int (V - \mu) |\Psi|^2 \, d\mathbf{r}, \quad (\text{B.4})$$

the kinetic, interaction and potential energies respectively. The kinetic energy can be further decomposed into compressible and incompressible parts by considering the kinetic energy spectrum \hat{E}_{kin} [52],

$$\hat{E}_{\text{kin}}(k) = \hat{E}_{\text{kin}}^i(k) + \hat{E}_{\text{kin}}^c(k), \quad (\text{B.5})$$

where \hat{E}_{kin}^i is the incompressible kinetic energy spectrum and \hat{E}_{kin}^c is the compressible kinetic energy spectrum.

B.2 Force

A useful quantity to know for the study of superflow around a gaussian obstacle is the force exerted by the fluid on the obstacle, also known as the drag force. Let

$$\begin{aligned} J_k &= \rho v_k, \\ p &= \frac{g}{2} \left(\frac{\rho}{m} \right)^2, \\ P_{jk} &= -\frac{\hbar^2}{4m^2} \rho \frac{\partial}{\partial x_j} \frac{\partial}{\partial x_k} \ln(\rho), \\ T_{jk} &= \rho v_j v_k + p \delta_{jk} + P_{jk}. \end{aligned}$$

Then it can be shown that the two equations,

$$\frac{\partial}{\partial t} \rho + \frac{\partial}{\partial x_k} J_k = 0 \quad (\text{B.6})$$

$$\frac{\partial}{\partial t} J_k + \frac{\partial}{\partial x_j} T_{jk} + \rho \frac{\partial}{\partial x_k} \left(\frac{V}{m} \right) = 0, \quad (\text{B.7})$$

are equivalent to the continuity equation and modified Euler equation derived from the GPE in Section A.3. Now, using Equation B.7, the k th component of the force can be written,

$$F_k = \frac{\partial}{\partial t} \int_V \rho v_k dV = - \int_V \frac{\partial}{\partial x_j} T_{jk} dV - \int_V \rho \frac{\partial}{\partial x_k} \left(\frac{V}{m} \right) dV. \quad (\text{B.8})$$

B.3 Healing Length

The characteristic length scale of a GPE based system is the healing length, ξ . We can directly find a expression for ξ by considering the minimum length needed for a large perturbation to return to the equilibrium value. Consider only the kinetic and interaction terms in Equation 7.1,

$$\frac{\hbar^2}{2m} \nabla^2 \Psi = g |\Psi(\mathbf{r}, t)|^2 \Psi. \quad (\text{B.9})$$

Dimensionally we can balance these terms by replacing $\nabla^2 \Psi$ with $2\Psi/\xi^2$, leading to

$$\frac{\hbar^2}{m\xi^2} = g\rho, \quad (\text{B.10})$$

where $\rho = |\Psi(\mathbf{r}, t)|^2$. Rearranging for ξ ,

$$\xi = \frac{\hbar}{\sqrt{mg\rho}}. \quad (\text{B.11})$$

Appendix C

Algorithms

C.1 Density/Phase Visualisation Technique

A technique to visualise both the wavefunction phase and density is used throughout this thesis. The advantage of the method is that it allows for an easy way to visualise the state of the phase of the system, while also retaining information about what areas of phase are unimportant due to the non-existence of fluid density in that region. Common problems with phase visualisation include the prevalence of ghost vortices[10] when considering a trapped condensate; with this method the discontinuities introduced by ghost vortices are entirely unseen. Previously, this has been attained through the use of masks to hide the unimportant phase regions in trapped systems. These masks are quite arbitrary in nature and an overzealous mask may hide details. Additionally, any condensate with a breathing mode or centre of mass oscillation will periodically extend beyond a hard coded mask. The method outlined in this section instead smoothly hides the unwanted areas of phase by using the density information in the system, disregarding the need for masks completely.

C.1.1 Plotting Algorithm

Initially, the phase plotting is performed as normal, a process involving a conversion of a set of values in the region $[-\pi, \pi]$ to an image (defined as a 2D grid of pixels of size $n \times m$). Examples include MATLAB's `image`/`pcolor` commands or `gnuplot`'s `splot` command. It is recommended, but not required, that a periodic colourmap (such as MATLAB's '`hsv`') of equal lightness is used. The $n \times m$ pixels obtained from this procedure will most commonly be stored in the `rgb` format, a triad of values (r, g, b) corresponding to the values of the red, green and blue intensities of the pixel respectively. For a maximum intensity of 255 (a common format for `rgb` pixels), a pixel with value $(0, 0, 0)$ is black, and a pixel of $(255, 255, 255)$ is white.

Each pixel must be instead represented in the **hs1** format, a triad of values (h, s, l) corresponding to the values of the hue, saturation and lightness of the pixel respectively. **hs1** is most commonly represented such that $h \in [0, 360)$ and $s, l \in [0, 1]$. Any pixel of the form $(h, s, 0)$ is black, and any pixel of the form $(h, s, 1)$ is white.

For each pixel, the lightness is then modified so that for a pixel at location (x, y) , $l = |\Psi(x, y)|^2 / \max(|\Psi|^2)$. Once complete, conversion back to (r, g, b) must presumably be performed, before finally re-plotting in one's software of choice. Areas of low density will appear in black, which areas of high density will show hues corresponding to the fluid phase at that location.

C.1.2 Colour space conversion - rgb to hs1

Given an **rgb** format pixel (r, g, b) , rescale so that $r, g, b \in [0, 1]$. Compute $m = \max(r, g, b)$, $n = \min(r, g, b)$ and set $l = (m + n)/2$. If $m = n$ then the pixel is achromatic and $h = s = 0$, otherwise compute

$$s = \begin{cases} \frac{m-n}{2-m-n} & \text{if } l \leq 0.5 \\ \frac{m-n}{m+n} & \text{if } l > 0.5. \end{cases} \quad (\text{C.1})$$

Finally, find

$$h = \begin{cases} 60(\frac{g-b}{m-n}) & \text{if } m = r \\ 60(\frac{b-r}{m-n} + 2) & \text{if } m = g \\ 60(\frac{r-g}{m-n} + 4) & \text{if } m = b. \end{cases} \quad (\text{C.2})$$

C.1.3 Colour space conversion - hs1 to rgb

Given a **hs1** format pixel (h, s, l) , compute $c = (1 - |2l - 1|) \times s$ and $h' = h/60$. With this, one can find $x = c(1 - |h' \bmod 2 - 1|)$. Find

$$(r', g', b') = \begin{cases} (c, x, 0) & \text{if } 0 \leq h' < 1 \\ (x, c, 0) & \text{if } 1 \leq h' < 2 \\ (0, c, x) & \text{if } 2 \leq h' < 3 \\ (0, x, c) & \text{if } 3 \leq h' < 4 \\ (x, 0, c) & \text{if } 4 \leq h' < 5 \\ (c, 0, x) & \text{if } 5 \leq h' < 6, \end{cases} \quad (\text{C.3})$$

and compute $m = l - c/2$ to finally find $(r, g, b) = (r' + m, g' + m, b' + m)$.

C.2 Other Numerical Algorithms

Algorithm 1: RK4 algorithm for advancing a ODE/PDE in time with optional re-normalisation.

```

input : An initial field  $\Psi$ , a step size  $h$ , optional phase profile  $\Theta$ 
 $t \leftarrow 0, dt \leftarrow -ih;$ 
repeat
    Perform a single step of the RK4 Scheme;
     $t = t + dt;$ 
     $n \leftarrow \text{norm}(\Psi);$ 
    for all points  $i$  in  $\Psi$  do
         $|\Psi[i] \leftarrow \Psi[i]/\sqrt{n};$ 
    end
    if we want a phase profile imprinted into the ground state then
        for all points  $i$  in  $\Psi$  do
             $|\Psi[i] \leftarrow \Theta[i].|\Psi[i]|;$ 
        end
    end
until a suitable ground state is found;
 $dt = h;$ 
repeat
    Perform a single step of the RK4 Scheme;
     $t = t + dt;$ 
    if real time normalisation is enabled then
         $n \leftarrow \text{norm}(\Psi);$ 
        for all points  $i$  in  $\Psi$  do
             $|\Psi[i] \leftarrow \Psi[i]/\sqrt{n};$ 
        end
    end
until satisfied;

```

Algorithm 2: Vortex detection. Outputs a field with positive values near a vortex with circulation 1, negative values near a vortex with circulation -1 and zero valued otherwise. This algorithm will detect ghost vortices.

```

input :A  $n_x \times n_y$  phase profile  $\theta$ . A line integral width  $l$ .
output:A ‘vortex field’  $Q$ .

for  $i \leftarrow 1 + l/2$  to  $n_x - l/2$  do
    for  $i \leftarrow 1 + l/2$  to  $n_y - l/2$  do
         $| Q[i, j] \leftarrow \oint_{C_{[i,j]}} \nabla \theta \cdot ds$ , where  $C_{[i,j]}$  is a square loop of width  $l$  centred on
         $|$  point  $[i, j]$ ;
    end
end
```

Algorithm 3: Improved vortex detection. Outputs a field with positive values near a vortex with circulation 1, negative values near a vortex with circulation -1 and zero valued otherwise. This method ignores ghost vortices.

```

input :A  $n_x \times n_y$  density profile  $R$ , A  $n_x \times n_y$  phase profile  $\theta$ . A line integral width
 $l$ .
output:A ‘vortex field’  $Q$ .

for  $i \leftarrow 1 + l/2$  to  $n_x - l/2$  do
    for  $i \leftarrow 1 + l/2$  to  $n_y - l/2$  do
         $| S \leftarrow R(i, j)/\max(R)$ ;
         $| Q[i, j] \leftarrow S \times \oint_{C_{[i,j]}} \nabla \theta \cdot ds$ , where  $C_{[i,j]}$  is a square loop of width  $l$  centred on
         $|$  point  $[i, j]$ ;
    end
end
```

Algorithm 4: Gaussian convolution. Filters out features with structures of size less than the input filter width. The output is analogous to a ‘blurring’ of the input field. This allows high frequency noise to be removed.

```

input : A  $n_x \times n_y$  field  $Q$ , a Gaussian filter width  $g$ .
output: A  $n_x \times n_y$  field  $G$ .
 $G[i] \leftarrow 0;$ 
for  $k \leftarrow 1$  to  $n_x$  do
    for  $l \leftarrow 1$  to  $n_y$  do
        for  $i \leftarrow 1$  to  $n_x$  do
            for  $j \leftarrow 1$  to  $n_y$  do
                 $| G[k, l] \leftarrow G[k, l] + Q[i, j] \times \exp(-[(k - i)^2 + (l - j)^2]/g^2);$ 
            end
        end
         $| G[k, l] \leftarrow G[k, l]/(n_x \cdot n_y);$ 
    end
end

```

Algorithm 5: The B/W Label algorithm. Outputs a field with the same non-zero regions of the input binary field, but with each connected region labeled with a unique value.

```

input :A  $n_x \times n_y$  binary field  $P$ .
output:A  $n_x \times n_y$  field  $Q$ .
Let  $L$  be a  $4 \times (n_x.n_y)$  field;
Let  $A$  be a vector length 4;
for all points  $i$  in  $L$  do  $L[i] \leftarrow -1$  ;
for all points  $i$  in  $Q$  do  $Q[i] \leftarrow -1$  ;
 $l_c \leftarrow 1, r_c \leftarrow 0$ ;
for  $i \leftarrow 2$  to  $n_x - 1$  do
    for  $j \leftarrow 2$  to  $n_y - 1$  do
        if  $P[i, j] = 0$  then continue;
         $A \leftarrow (Q[i + 1, j - 1], Q[i, j - 1], Q[i - 1, j - 1], Q[i - 1, j])$ ;
        for  $c \leftarrow 1$  to 4 do
            if  $A[c] \geq 0$  then
                 $Q[i, j] \leftarrow A[c]$ ;
                 $L[c, l_c] \leftarrow A[c]$ ;
            end
        end
        if  $Q[i, j] \geq 0$  then  $l_c \leftarrow l_c + 1$ ;
        else
             $Q[i, j] \leftarrow r_c$ ;
             $r_c \leftarrow r_c + 1$ ;
        end
    end
end
for  $r \leftarrow 1$  to  $(n_x.n_y)$  do
    if  $\max(\text{elements of } L \text{ in row } r) = -1$  then continue;
     $m \leftarrow \min(\text{elements of } L \text{ in row } r \text{ with value } \geq 0)$ ;
    for  $c \leftarrow 1$  to 4 do
        if  $L[c, r] \neq m$  and  $L[c, r] \geq 0$  then
            for all points  $i$  in  $Q$  do
                if  $Q[i] = L[c, r]$  then  $Q[i] \leftarrow m$ ;
            end
        end
    end
end

```

Algorithm 6: Calculate vortex locations and polarity.

```

input : A  $n_x \times n_y$  field  $\theta$ . A  $n_x \times n_y$  field  $P$ . A threshold value  $t$ .
output: Number of vortices found,  $n_v$ . Vortex location, a  $2 \times n_v$  field  $V_l$ . Vortex
polarity, a vector  $V_p$  of length  $n_v$ .

 $Q \leftarrow$  Algorithm 4  $\leftarrow$  Algorithm 2  $\leftarrow (\theta, P)$ ;
 $R \leftarrow 0$  at every point,  $S \leftarrow 0$  at every point;
 $n_v \leftarrow 0$ ;
for  $i \leftarrow 1$  to  $n_x$  do
    for  $j \leftarrow 1$  to  $n_y$  do
        if  $Q[i, j] > t$  then  $R[i, j] = 1$ ;
        if  $Q[i, j] < t$  then  $S[i, j] = 1$ ;
    end
end
foreach  $C \in (R, S)$  do
     $D \leftarrow$  Algorithm 5  $\leftarrow C$ ;
    for  $i \leftarrow 1$  to  $\max(D)$  do
         $V[1, n_v] \leftarrow$  mean row of the points where  $D = i$ ;
         $V[2, n_v] \leftarrow$  mean column of the points where  $D = i$ ;
        if  $C = R$  then  $V[3, n_v] \leftarrow 1$ ;
        if  $C = S$  then  $V[3, n_v] \leftarrow -1$ ;
         $n_v \leftarrow n_v + 1$ ;
    end
end

```

Algorithm 7: The Recursive Cluster Algorithm. Decomposes a list of vortices into vortex dipoles or clusters. Vortices are labelled with a cluster number, with vortex dipoles labelled with -1.

```

input : Vortex locations and polarity. Number of vortices,  $n_v$ .
output: A group number for each vortex

 $n_{rca} \leftarrow 0$ ;
while dipoles continue to be identified do
    for  $i \leftarrow 1$  to  $n_v$  do
        if vortex i is mutual nearest neighbours with some other vortex j then
            if vortex i is of opposite polarity to j then
                | Set both vortices as group -1;
            end
        end
    end
end
while the vortex group configuration continues to change do
    for  $(i, j)$  in 1 to  $n_v$  do
        if either vortex i or j is in group -1 then continue;
        if vortex i and j are closer than either is to a vortex of opposite polarity then
            if one of the two vortices i and j is in a group n then
                | Set both vortices as group n;
            else if both vortices i and j are in groups n and m then
                | Set all vortices in groups n and m as group  $\min(n, m)$ ;
            else
                |  $n_{rca} \leftarrow n_{rca} + 1$ ;
                | Set both vortices as group  $n_{rca}$ ;
            end
        end
    end
end

```

Algorithm 8: The vortex unwinding algorithm. By accurately imprinting a vortex, this algorithm removes vortices from the input wavefunction non-destructively.

```

input : A  $n_x \times n_y$  complex field  $\psi$ . A ‘safe’ distance  $d$ . Vortex core radius  $c$ .
output: A  $n_x \times n_y$  complex field  $\phi$ .

 $\phi \leftarrow \psi;$ 
 $(n_v, V_l, V_p) \leftarrow \text{Algorithm 6} \leftarrow \psi;$ 
for  $i \leftarrow 1$  to  $n_v$  do
    if  $|V_l[i]| > d$  then
        Imprint a vortex of polarity  $V_p[i]$  at location  $V_l[i]$  in  $\phi$ ;
        for  $j \leftarrow -c$  to  $c$  do
            for  $k \leftarrow -c$  to  $c$  do
                 $x \leftarrow V_l[1, i] + j;$ 
                 $y \leftarrow V_l[2, i] + k;$ 
                 $\phi(x, y) \leftarrow \psi_{\text{inf}} \times \text{phase}(\psi(x, y));$ 
            end
        end
    end
end

```

Bibliography

- [1] A. Görlitz, J. M. Vogels, A. E. Leanhardt, C. Raman, T. L. Gustavson, J. R. Abo-Shaeer, A. P. Chikkatur, S. Gupta, S. Inouye, T. Rosenband, et al., Phys. Rev. Lett. **87**, 130402 (2001).
- [2] N. G. Parker, Ph.D. thesis, The University of Durham (2004).
- [3] J. Thijssen, *Computational Physics* (Cambridge University Press, 1999), ISBN 9780521575881.
- [4] W. Bao and W. Tang, Journal of Computational Physics **187**, 230 (2003), ISSN 0021-9991.
- [5] M. Edwards and K. Burnett, Phys. Rev. A **51**, 1382 (1995).
- [6] W. H. Press, S. A. Teukolsky, W. T. Vetterling, and B. P. Flannery, *Numerical Recipes in FORTRAN; The Art of Scientific Computing* (Cambridge University Press, New York, NY, USA, 1993), 2nd ed., ISBN 0521437164.
- [7] M. L. Chiofalo, S. Succi, and M. P. Tosi, Phys. Rev. E **62**, 7438 (2000).
- [8] C. F. Barenghi, R. Donnelly, W. Vinen, and eds., *Physical Kinetics, Landau and Lifshitz Course of Theoretical Physics Vol. 10* (Pergamon Press, Oxford, 1981).
- [9] S. Choi, S. A. Morgan, and K. Burnett, Phys. Rev. A **57**, 4057 (1998).
- [10] M. Tsubota, K. Kasamatsu, and M. Ueda, Phys. Rev. A **65**, 023603 (2002).
- [11] E. Madarassy and C. F. Barenghi, Journal of Low Temperature Physics **152**, 122 (2008).
- [12] A. A. Penckwitt, R. J. Ballagh, and C. W. Gardiner, Phys. Rev. Lett. **89**, 260402 (2002).
- [13] C. W. Gardiner, P. Zoller, R. J. Ballagh, and M. J. Davis, Phys. Rev. Lett. **79**, 1793 (1997).

Bibliography

- [14] N. G. Berloff and B. V. Svistunov, Phys. Rev. A **66**, 013603 (2002).
- [15] P. Carruthers and K. S. Dy, Phys. Rev. **147**, 214 (1966).
- [16] V. E. Zakharov and A. B. Shabat, Sov. Phys. JETP **34**, 62 (1972).
- [17] V. E. Zakharov and A. B. Shabat, Sov. Phys. JETP **37**, 823 (1973).
- [18] B. P. Anderson, P. C. Haljan, C. A. Regal, D. L. Feder, L. A. Collins, C. W. Clark, and E. A. Cornell, Phys. Rev. Lett. **86**, 2926 (2001).
- [19] Z. Dutton, M. Budde, C. Slowe, and L. V. Hau, Science **293**, 663 (2001).
- [20] D. L. Feder, M. S. Pindzola, L. A. Collins, B. I. Schneider, and C. W. Clark, Phys. Rev. A **62**, 053606 (2000).
- [21] N. G. Berloff, Journal of Physics A: Mathematical and General **37**, 1617 (2004).
- [22] M. J. Davis, S. A. Morgan, and K. Burnett, Phys. Rev. Lett. **87**, 160402 (2001).
- [23] C. Lawson, Ph.D. thesis, Lancaster University (2013).
- [24] L. Skrbek and W. Vinen, in *Quantum Turbulence*, edited by M. Tsubota and W. Halperin (Elsevier, 2009), vol. 16 of *Progress in Low Temperature Physics*, pp. 195 – 246.
- [25] S. Davis, P. Hendry, and P. McClintonck, Physica B: Condensed Matter **280**, 43 (2000).
- [26] A. Guénault, V. Keith, C. Kennedy, S. Mussett, and G. Pickett, Journal of Low Temperature Physics **62**, 511 (1986), ISSN 0022-2291.
- [27] D. I. Bradley, D. O. Clubb, S. N. Fisher, A. M. Guénault, R. P. Haley, C. J. Matthews, G. R. Pickett, V. Tsepelin, and K. Zaki, Phys. Rev. Lett. **95**, 035302 (2005).
- [28] D. Bradley, M. Človečko, M. Fear, S. Fisher, A. Guénault, R. Haley, C. Lawson, G. Pickett, R. Schanen, V. Tsepelin, et al., Journal of Low Temperature Physics **165**, 114 (2011).
- [29] S. N. Fisher, A. J. Hale, A. M. Guénault, and G. R. Pickett, Phys. Rev. Lett. **86**, 244 (2001).
- [30] R. Goto, S. Fujiyama, H. Yano, Y. Nago, N. Hashimoto, K. Obara, O. Ishikawa, M. Tsubota, and T. Hata, Phys. Rev. Lett. **100**, 045301 (2008).
- [31] R. Blaauwgeers, M. Blazkova, M. Človečko, V. Eltsov, R. de Graaf, J. Hosio, M. Krusius, D. Schmoranz, W. Schoepe, L. Skrbek, et al., Journal of Low Temperature Physics **146**, 537 (2007).

- [32] D. I. Bradley, M. Človečko, S. N. Fisher, D. Garg, E. Guise, R. P. Haley, O. Kolosov, G. R. Pickett, V. Tsepelin, D. Schmoranzer, et al., Phys. Rev. B **85**, 014501 (2012).
- [33] J. Jäger, B. Schuderer, and W. Schoepe, Phys. Rev. Lett. **74**, 566 (1995).
- [34] R. P. Duncan, Journal of Ecology **81**, 403 (1993).
- [35] C. J. Peterson and E. R. Squiers, Journal of Ecology **83**, 847 (1995).
- [36] D. Stoyan and A. Penttinen, Statistical Science **15**, 61 (2000).
- [37] N. E. Stamp and J. R. Lucas, Journal of Ecology **78**, 589 (1990).
- [38] K. F. Gaines, A. L. Bryan, and P. M. Dixon, Waterbirds **23**, 64 (2000).
- [39] P. J. Diggle and A. G. Chetwynd, Biometrics **47**, 1155 (1991).
- [40] P. M. Dixon, Encyclopaedia of Environments **3**, 1796 (2002).
- [41] B. D. Ripley, Journal of Applied Probability **13**, 255 (1976).
- [42] B. D. Ripley, Journal of the Royal Statistical Society **41**, 368 (1979).
- [43] M. T. Reeves, T. P. Billam, B. P. Anderson, and A. S. Bradley, Phys. Rev. Lett. **110**, 104501 (2013).
- [44] M. T. Reeves, T. P. Billam, B. P. Anderson, and A. S. Bradley, Phys. Rev. A **89**, 053631 (2014).
- [45] H. W. Kuhn, Naval Research Logistics Quarterly **2**, 83–97 (1955).
- [46] M. T. Reeves, T. P. Billam, B. P. Anderson, and A. S. Bradley, Phys. Rev. Lett. **114**, 155302 (2015).
- [47] S. Taneda, J. Phys. Soc. Jpn. **11**, 302 (1956).
- [48] S. Taneda, J. Phys. Soc. Jpn. **50**, 1398 (1981).
- [49] M. Van Dyke, *An Album of Fluid Motion* (Parabolic Press, Stanford, CA, 1982).
- [50] J. Maurer and P. Tabeling, EPL (Europhysics Letters) **43**, 29 (1998).
- [51] J. Salort, C. Baudet, B. Castaing, B. Chabaud, F. Daviaud, T. Didelot, P. Diribarne, B. Dubrulle, Y. Gagne, F. Gauthier, et al., Physics of Fluids **22**, 125102 (2010).
- [52] C. Nore, M. Abid, and M. E. Brachet, Phys. Rev. Lett. **78**, 3896 (1997).
- [53] M. Kobayashi and M. Tsubota, Phys. Rev. Lett. **94**, 065302 (2005).

Bibliography

- [54] A. W. Baggaley, J. Laurie, and C. F. Barenghi, Phys. Rev. Lett. **109**, 205304 (2012).
- [55] JETP Letters **80**, 479 (2004).
- [56] U. Frisch, *Turbulence. The legacy of A.N. Kolmogorov* (Cambridge University Press, Cambridge, 1995).
- [57] C. F. Barenghi, V. L'vov, and P.-E. Roche, *Velocity spectra of quantum turbulence: experiments, numerics and models* (2013), arXiv:1306.6248.
- [58] M. R. Smith, D. K. Hilton, and S. Van Sciver, Phys. Fluids **11**, 1 (1999).
- [59] T. Zhang and S. Van Sciver, Nature Physics **1**, 36 (2005).
- [60] Y. Sergeev and C. Barenghi, J. Low Temp. Phys. **157**, 429 (2009).
- [61] R. Hänninen, M. Tsubota, and W. F. Vinen, Phys. Rev. B **75**, 064502 (2007).
- [62] S. Fujiyama and M. Tsubota, Phys. Rev. B **79**, 094513 (2009).
- [63] T. Frisch, Y. Pomeau, and S. Rica, Phys. Rev. Lett. **69**, 1644 (1992).
- [64] K. Sasaki, N. Suzuki, and H. Saito, Phys. Rev. Lett. **104**, 150404 (2010).
- [65] B. Jackson, J. F. McCann, and C. S. Adams, Phys. Rev. A **61**, 051603 (2000).
- [66] C. Nore, M. E. Brachet, and S. Fauve, Physica D **65**, 154 (1993).
- [67] T. Winiecki, J. F. McCann, and C. S. Adams, Phys. Rev. Lett. **82**, 5186 (1999).
- [68] T. Winiecki, B. Jackson, J. F. McCann, and C. S. Adams, Journal of Physics B: Atomic, Molecular and Optical Physics **33**, 4069 (2000).
- [69] C. Huepe and M. E. Brachet, Physica D (Amsterdam) **140**, 126 (2000).
- [70] J. S. Stießberger and W. Zwerger, Phys. Rev. A **62**, 061601 (2000).
- [71] M. Crescimanno, C. G. Koay, R. Peterson, and R. Walsworth, Phys. Rev. A **62**, 063612 (2000).
- [72] N. G. Berloff and P. H. Roberts, J. Phys. A **33**, 4025 (2000).
- [73] S. Rica, Physica D **148**, 221 (2001).
- [74] C. T. Pham, C. Nore, and M. E. Brachet, Comptes Rendus Physique **5**, 3 (2004).
- [75] B. Jackson, J. F. McCann, and C. S. Adams, Phys. Rev. Lett. **80**, 3903 (1998).
- [76] K. Fujimoto and M. Tsubota, Phys. Rev. A **83**, 053609 (2011).

- [77] T. Aioi, T. Kadokura, T. Kishimoto, and H. Saito, Phys. Rev. X **1**, 021003 (2011).
- [78] G. A. El, A. Gammal, and A. M. Kamchatnov, Phys. Rev. Lett. **97**, 180405 (2006).
- [79] I. Carusotto, S. X. Hu, L. A. Collins, and A. Smerzi, Phys. Rev. Lett. **97**, 260403 (2006).
- [80] C. Raman, M. Köhl, R. Onofrio, D. S. Durfee, C. E. Kuklewicz, Z. Hadzibabic, and W. Ketterle, Phys. Rev. Lett. **83**, 2502 (1999).
- [81] R. Onofrio, C. Raman, J. M. Vogels, J. R. Abo-Shaeer, A. P. Chikkatur, and W. Ketterle, Phys. Rev. Lett. **85**, 2228 (2000).
- [82] S. Inouye, S. Gupta, T. Rosenband, A. P. Chikkatur, A. Görlitz, T. L. Gustavson, A. E. Leanhardt, D. E. Pritchard, and W. Ketterle, Phys. Rev. Lett. **87**, 080402 (2001).
- [83] T. W. Neely, E. C. Samson, A. S. Bradley, M. J. Davis, and B. P. Anderson, Phys. Rev. Lett. **104**, 160401 (2010).
- [84] R. J. Donnelly, *Quantized Vortices in Helium II* (Cambridge University Press, Cambridge, 1991).
- [85] P. Nozières and D. Pines, *The Theory of Quantum Liquids II* (Addison-Wesley, Redwood City, 1990).
- [86] T. Winiecki, Ph.D. thesis, The University of Durham (2001).
- [87] A. C. White, C. F. Barenghi, and N. P. Proukakis, Phys. Rev. A **86**, 013635 (2012).
- [88] A. W. Baggaley, C. F. Barenghi, A. Shukurov, and Y. A. Sergeev, EPL (Europhysics Letters) **98**, 26002 (2012).
- [89] T. Winiecki, J. F. McCann, and C. S. Adams, EPL (Europhysics Letters) **48**, 475 (1999).
- [90] D. H. Wacks, A. W. Baggaley, and C. F. Barenghi, Physics of Fluids **26**, 027102 (2014).
- [91] M. Blažková, D. Schmoranzer, L. Skrbek, and W. F. Vinen, Phys. Rev. B **79**, 054522 (2009).
- [92] C. J. Foster, P. B. Blakie, and M. J. Davis, Phys. Rev. A **81**, 023623 (2010).
- [93] A. C. White, B. P. Anderson, and V. S. Bagnato, Proceedings of the National Academy of Sciences **111**, 4719 (2014).
- [94] C. F. Barenghi, L. Skrbek, and K. R. Sreenivasan, Proceedings of the National Academy of Sciences **111**, 4647 (2014).

Bibliography

- [95] C. F. Barenghi, R. Donnelly, W. Vinen, and eds., *Quantized Vortex Dynamics and Superfluid Turbulence* (Springer, Berlin, 2001).
- [96] E. A. L. Henn, J. A. Seman, G. Roati, K. M. F. Magalhães, and V. S. Bagnato, Phys. Rev. Lett. **103**, 045301 (2009).
- [97] N. G. Parker and C. S. Adams, Phys. Rev. Lett. **95**, 145301 (2005).
- [98] S. Middelkamp, P. J. Torres, P. G. Kevrekidis, D. J. Frantzeskakis, R. Carretero-González, P. Schmelcher, D. V. Freilich, and D. S. Hall, Phys. Rev. A **84**, 011605 (2011).
- [99] T. W. Neely, A. S. Bradley, E. C. Samson, S. J. Rooney, E. M. Wright, K. J. H. Law, R. Carretero-González, P. G. Kevrekidis, M. J. Davis, and B. P. Anderson, Phys. Rev. Lett. **111**, 235301 (2013).
- [100] W. J. Kwon, G. Moon, J.-y. Choi, S. W. Seo, and Y.-i. Shin, Phys. Rev. A **90**, 063627 (2014).
- [101] A. M. Mateo and V. Delgado, Phys. Rev. A **74**, 065602 (2006).
- [102] N. G. Parker and D. H. J. O'Dell, Phys. Rev. A **78**, 041601 (2008).
- [103] B. Jackson, N. P. Proukakis, C. F. Barenghi, and E. Zaremba, Phys. Rev. A **79**, 053615 (2009).
- [104] Y. Shin, private communication.
- [105] A. J. Allen, E. Zaremba, C. F. Barenghi, and N. P. Proukakis, Phys. Rev. A **87**, 013630 (2013).
- [106] D. Yan, R. Carretero-González, D. J. Frantzeskakis, P. G. Kevrekidis, N. P. Proukakis, and D. Spirn, Phys. Rev. A **89**, 043613 (2014).
- [107] G. W. Stagg, N. G. Parker, and C. F. Barenghi, Journal of Physics B: Atomic, Molecular and Optical Physics **47**, 095304 (2014).
- [108] S. Nazarenko and M. Onorato, Journal of Low Temperature Physics **146**, 31 (2007).
- [109] C. Rorai, K. R. Sreenivasan, and M. E. Fisher, Phys. Rev. B **88**, 134522 (2013).
- [110] S. Prabhakar, R. P. Singh, S. Gautam, and D. Angom, Journal of Physics B: Atomic, Molecular and Optical Physics **46**, 125302 (2013).
- [111] M. Leadbeater, T. Winiecki, D. C. Samuels, C. F. Barenghi, and C. S. Adams, Phys. Rev. Lett. **86**, 1410 (2001).

- [112] S. Zuccher, M. Caliari, A. Baggaley, and C. Barenghi, Physics of Fluids **24**, 125108 (2012).
- [113] A. T. Powis, S. J. Sammut, and T. P. Simula, Phys. Rev. Lett. **113**, 165303 (2014).
- [114] W. J. Kwon, G. Moon, S. W. Seo, and Y. Shin, Phys. Rev. A **91**, 053615 (2015).
- [115] W. J. Kwon, S. W. Seo, and Y. il Shin, *Periodic shedding of vortex dipoles from a moving penetrable obstacle in a bose-einstein condensate* (2015), arXiv:1508.00958.
- [116] R. Desbuquois, L. Chomaz, T. Yefsah, J. Léonard, J. Beugnon, C. Weitenberg, and J. Dalibard, Nature Physics **8**, 645 (2012).
- [117] G. W. Stagg, A. J. Allen, C. F. Barenghi, and N. G. Parker, Journal of Physics: Conference Series **594**, 012044 (2015).
- [118] T. Winiecki and C. S. Adams, EPL (Europhysics Letters) **52**, 257 (2000).
- [119] E. Hodby, G. Hechenblaikner, S. A. Hopkins, O. M. Maragò, and C. J. Foot, Phys. Rev. Lett. **88**, 010405 (2001).
- [120] J. R. Abo-Shaeer, C. Raman, and W. Ketterle, Phys. Rev. Lett. **88**, 070409 (2002).
- [121] J. E. Williams, E. Zaremba, B. Jackson, T. Nikuni, and A. Griffin, Phys. Rev. Lett. **88**, 070401 (2002).
- [122] K. Kasamatsu, M. Tsubota, and M. Ueda, Phys. Rev. A **67**, 033610 (2003).
- [123] C. Lobo, A. Sinatra, and Y. Castin, Phys. Rev. Lett. **92**, 020403 (2004).
- [124] M. Leadbeater, T. Winiecki, and C. S. Adams, Journal of Physics B: Atomic, Molecular and Optical Physics **36**, L143 (2003).
- [125] C. J. Pethick and H. Smith, *Bose-Einstein Condensation in Dilute Gases* (Cambridge University Press, Cambridge, 2002).
- [126] M. Brewczyk, M. Gajda, and K. RzaÅijewski, Journal of Physics B: Atomic, Molecular and Optical Physics **40**, R1 (2007).
- [127] N. P. Proukakis and B. Jackson, Journal of Physics B: Atomic, Molecular and Optical Physics **41**, 203002 (2008).
- [128] A. Griffin, T. Nikuni, and E. Zaremba, *Bose-Condensed Gases at Finite Temperatures* (Cambridge University Press, 2009), ISBN 9780521837026.

Bibliography

- [129] N. Proukakis, S. Gardiner, M. Davis, and M. Szymanska, *Quantum Gases: Finite Temperatures and Non-equilibrium Dynamics*, Cold atoms (Imperial College Press, 2013), ISBN 9781848168107.
- [130] P. Blakie, A. Bradley, M. Davis, R. Ballagh, and C. Gardiner, Advances in Physics **57**, 363 (2008).
- [131] N. G. Berloff, M. Brachet, and N. P. Proukakis, Proceedings of the National Academy of Sciences **111**, 4675 (2014).
- [132] Y. Kagan and B. V. Svistunov, Phys. Rev. Lett. **79**, 3331 (1997).
- [133] M. J. Davis, S. A. Morgan, and K. Burnett, Phys. Rev. Lett. **87**, 160402 (2001).
- [134] A. Sinatra, C. Lobo, and Y. Castin, Phys. Rev. Lett. **87**, 210404 (2001).
- [135] M. J. Davis, S. A. Morgan, and K. Burnett, Phys. Rev. A **66**, 053618 (2002).
- [136] C. Connaughton, C. Josserand, A. Picozzi, Y. Pomeau, and S. Rica, Phys. Rev. Lett. **95**, 263901 (2005).
- [137] R. W. Pattinson, N. P. Proukakis, and N. G. Parker, Phys. Rev. A **90**, 033625 (2014).
- [138] S. Nazarenko, M. Onorato, and D. Proment, Phys. Rev. A **90**, 013624 (2014).
- [139] M. J. Davis and P. B. Blakie, Phys. Rev. Lett. **96**, 060404 (2006).
- [140] T. M. Wright, N. P. Proukakis, and M. J. Davis, Phys. Rev. A **84**, 023608 (2011).
- [141] T. P. Simula and P. B. Blakie, Phys. Rev. Lett. **96**, 020404 (2006).
- [142] N. G. Berloff and A. J. Youd, Phys. Rev. Lett. **99**, 145301 (2007).
- [143] N. Berloff and C. Yin, Journal of Low Temperature Physics **145**, 187 (2006), ISSN 0022-2291.
- [144] H. Salman and N. G. Berloff, Physica D: Nonlinear Phenomena **238**, 1482 (2009), nonlinear Phenomena in Degenerate Quantum Gases.
- [145] N. G. Berloff and B. V. Svistunov, Phys. Rev. A **66**, 013603 (2002).
- [146] L. Hough, L. A. K. Donev, and R. J. Zieve, Phys. Rev. B **65**, 024511 (2001).
- [147] A. L. Gaunt, T. F. Schmidutz, I. Gotlibovych, R. P. Smith, and Z. Hadzibabic, Phys. Rev. Lett. **110**, 200406 (2013).
- [148] L. C. *et al.*, Nat. Comm. **6**, 6162 (2015).

- [149] R. Hänninen, M. Tsubota, and W. F. Vinen, Phys. Rev. B **75**, 064502 (2007).
- [150] D. Kivotides, C. F. Barenghi, and Y. A. Sergeev, Phys. Rev. B **77**, 014527 (2008).
- [151] R. Hänninen and A. W. Baggaley, Proceedings of the National Academy of Sciences **111**, 4667 (2014).
- [152] G. W. Rayfield and F. Reif, Phys. Rev. **136**, A1194 (1964).
- [153] N. P. Proukakis and B. Jackson, Journal of Physics B: Atomic, Molecular and Optical Physics **41**, 203002 (2008).
- [154] A. Fetter and J. Walecka, *Quantum theory of many-particle systems*, International series in pure and applied physics (McGraw-Hill, 1971).
- [155] N. N. Bogoliubov, J. Phys. USSR **11**, 23 (1947).
- [156] K. Huang, *Statistical mechanics* (Wiley, 1987), ISBN 9780471815181.